

Dark Matter Plasma Instabilities

von

Patrick Schillings

Masterarbeit in Physik

vorgelegt der

**Fakultät für Mathematik, Informatik und Naturwissenschaften
der RWTH Aachen**

im Oktober, 2022

angefertigt im

Institut für theoretische Teilchenphysik und Kosmologie

bei

Philipp Mertsch

Zweitprüfer:

Julien Lesgourges

I assure that I wrote this thesis all by myself and used no other sources and means than those I have cited properly.

Contents

1	Introduction	5
1.1	Dark Matter	5
1.2	Galaxy Cluster and the Bullet Cluster	7
1.3	Plasma Physics	8
1.4	Waves and Instabilities	10
2	Dark Matter Plasma	15
2.1	Is this a great idea? - Putting the dark matter on the plasma proof	15
2.2	Relevant Types of Instabilities	18
3	The Linear Two-Stream Instability	25
3.1	The Cold Case	25
3.2	The Warm Case	26
3.2.1	Calculating the Dispersion Relation in the Vlasov Approach	26
3.2.2	Transformations of Coordinate Systems	30
3.2.3	Numerical Evaluation of the Warm Dispersion Relation	32
3.3	Mediator Mass	40
3.4	Time Evolution	42
4	PIC-Simulations	49
4.1	Introduction to PIC-simulations	49
4.2	Electron Plasma Waves	51
4.3	The Full Two-Stream Instability	58
4.4	Noise	68
4.4.1	Random Noise	70
4.4.2	Noise of the Galaxy Substructure	71
4.4.3	Translation into PIC-simulations	74

4.5	Final Boundaries	76
5	Conclusions and Outlook	78
A	The plasma dispersion function	81
B	More fun Setups	81
B.1	Reset	82
B.2	Two Blops	82
B.3	Sliced Cluster	82
C	TRISTAN-MP	83
C.1	Tips for the Setup	83

1 Introduction

In this thesis, I will research the long-ranged interactions of possible dark matter models.

1.1 Dark Matter

In 1933, Fritz Zwicky evaluated the velocity dispersion of the Coma-Cluster via the virial theorem and discovered that the required mass for this velocity dispersion would be considerably higher than the observed luminous mass [1]. He assumed the reason to be some yet undiscovered matter, the same that Jan Hendrik Oort needed to explain the velocity of stars in the solar neighbourhood perpendicular to the disk [2]. Vera Rubin's measurement of the rotation velocity of stars in the Andromeda Galaxy supported that idea because, for a flat disk of mass, the rotation velocity should decrease with the distance to the center [3]. A halo of dark matter was suspected around every galaxy and galaxy cluster and was later visualized by gravitational lensing of the Bullet Cluster [4] (see Figure 1).

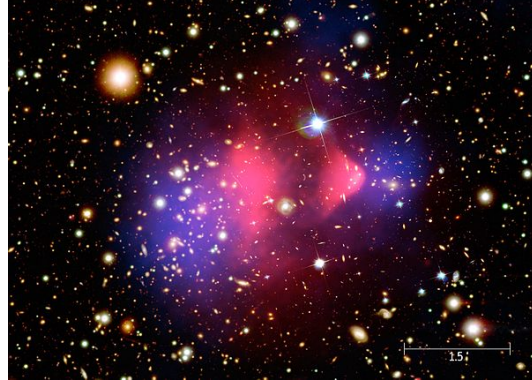


Figure 1: The Bullet Cluster [4]: The stars were observed in the visible spectrum, while the gas clouds measured by Chandra with their Roentgen-spectrum are shown in pink. The blue area is the mass distribution of the galaxies found by gravitational lensing with Hubble. Because it is not slowed down by friction, dark matter must have low self-interaction. Picture from [5].

Sky surveys supported this idea [6] and the measurement of the Cosmic Microwave Background, where the Λ CDM-model demands a non-baryonic

massive component for perturbations to grow fast enough, even yielded the most accurate measurement of the dark matter density in the universe today: $\Omega_{\text{DM}} h^2 \equiv \frac{\rho_{\text{DM}}}{\rho_{\text{crit},0}/h^2} = 0.120$ [7], where Ω_{DM} is the density parameter of dark matter, ρ_{DM} the dark matter density, h is the Hubble constant normalized to 100 km/s/Mpc and $\rho_{\text{crit},0}$ is the critical density for a flat universe today.

While dark matter is mostly known for its gravitational effects, physicists ask the question of what other properties we can infer. What is the mass of dark matter and what quantum numbers does it carry? Does it consist of unknown particles that could be an extension of the standard model and if so, how many of them are there? Answering these questions requires a lot of model-building, making predictions and falsifying them through measurements. Until now, we only know some cosmological properties of dark matter:

First of all, dark matter is measured to be adiabatic by several sky surveys, meaning it is denser where ordinary matter and photons are denser [6]. It also follows that it has to be cold, which means it is moving non-relativistically at the time of structure formation. Otherwise, streams of hot dark matter would have dissolved all visible clumps of structure. Moreover, it should be non-baryonic (from the cosmic microwave background [8, 7]) and its coupling to the standard-model particles and to itself must be very small (otherwise it would not be dark or the bullet cluster would look different). The self-interaction will be addressed more closely in this thesis. Furthermore, the expected quantity is about five times the amount of ordinary matter [7]. We know this from the mass differences between expected and measured values in gravitational lensing and the rotation curves, as well as a more exact value from the needed perturbation growth for the acoustic cosmic microwave background peaks. From that, it directly follows that dark matter should be stable, meaning its life-time must be larger than the age of the universe because the amount stayed the same from recombination to today.

A dark matter candidate χ is characterized by its mass m_χ and at least one coupling g , the nature of which is most interesting to modern researchers. For a long time, it was suspected that dark matter could interact via the weak force, which is already known and investigated. This Weakly Interacting Massive Particle (WIMP) was the astronomers' favourite candidate, but is mainly ruled out by now [9]. As one, thus, needs a completely new force to mediate between the dark matter particles, one tends to stick to the simplest ones, and in this thesis, I will mainly focus on U(1)-group dark matter models

with some dark charge and a single mediator particle, a dark photon, which may be massive with mass m_A . Similarly, a very small electric charge could still be considered, which would enable the dark matter to interact weakly with the standard model baryons, or some mixing between the dark and the real photon could be included. All of them should follow the same set of base equations: the (dark) Maxwell equations (or in the case of a massive mediator, the Proca-equation).

1.2 Galaxy Cluster and the Bullet Cluster

Matter in our universe shows structure at different length scales: In dense clouds, it tends to form stars, stars are clustered in galaxies, and galaxies themselves are again clustered - quite obviously named - in galaxy clusters. While a single galaxy has an expansion of about 10 kpc, a galaxy cluster extends up to 5 Mpc and contains up to 1000 galaxies. Their weight may be $10^{15} M_\odot$. An example is the Virgo Cluster [10].

Galaxy clusters do not only consist of the bunched galaxies, but additionally of intra-cluster gas and a halo of dark matter. Because of the continuous dark matter density profiles, it is not always unambiguous where the cluster boundaries are. The same is true for galactic halos. A common method, therefore, is to define the border at the radius where the averaged mass density profile is equal to Δ times the critical density $\frac{\rho_c}{h^2} = \frac{3H_0^2/h^2}{8\pi G} = \frac{1.88 \cdot 10^{-26}}{h^2} \text{ kg/m}^3$ where H_0 is the Hubble parameter today, h the normalized Hubble parameter and G the gravitational constant. The critical density is the density the universe should have if its space-time is flat and, coincidentally, this is the case [7]. The mass and radius of a galaxy (cluster) can, thus, be defined via

$$\frac{M(R_\Delta)}{\frac{4}{3}\pi R_\Delta^3} = \Delta\rho_c. \quad (1)$$

Commonly, $\Delta = 200$ is chosen to define the galaxy (cluster) size R_{200} and the mass $M_{200} = M(R_{200})$ [11].

In N-Body simulations, a large number of massive (quasi)particles will be simulated with regard to their gravitational interactions. They show that the particles typically arrange themselves corresponding to the NFW-profile [12, 13]

$$\rho_{\text{NFW}}(r) = \frac{\rho_0}{\frac{r}{r_s} \left(1 + \frac{r}{r_s}\right)^2}, \quad (2)$$

where r_s denotes some scale radius and ρ_0 the density at r_s . This is true for the galaxies inside a cluster, as well as for the dark matter inside the galaxies and the galaxy cluster. Of course, when integrating this over the volume to determine the mass, the integral will diverge. To resolve this, one cuts off this profile at $R_{200} = cr_s$ where c is called a concentration parameter. For galaxies, typical values are $M_{200} = 10^{12} M_\odot$, $R_{200} = 200$ kpc and $c = 10$ [14]. Particularly interesting is the previously mentioned bullet cluster. The two clusters collided 100 Myrs ago [4] and are drifting apart with a speed of $2v_0 = 2600$ km/s since then [15]. Fits of weak lensing data to the NFW-profile give for the heavier cluster $M_{200} = 1.5 \cdot 10^{15} M_\odot$, $R_{200} = 2136$ kpc and $c = 1.94$ and for the ‘bullet’ $M_{200} = 1.5 \cdot 10^{14} M_\odot$, $R_{200} = 995$ kpc and $c = 7.12$ [15].

For our purpose, though, it can be useful to approximate the dark matter profile of the Bullet Cluster by a cored profile with the values $R = 250$ kpc, $M = 2 \cdot 10^{14} M_\odot$ and a velocity dispersion of $V = 100$ km/s [16]. The model will have a constant density of

$$\rho_\chi = \frac{M}{\frac{4}{3}\pi R^3} = 1.78 \text{kg/m}^3 = 0.1 \text{GeV/cm}^3. \quad (3)$$

The time the two clusters needed to cross each other will be called

$$t_{\text{cross}} = \frac{R}{2v_0} = 9.4 \cdot 10^7 \text{yr}. \quad (4)$$

One can find more information on the structures of the universe in [17]. Colliding clusters and the Bullet Cluster in particular will be an interesting laboratory for my research.

1.3 Plasma Physics

A plasma, simply speaking, is a bunch of particles with collective behaviour induced by some long-range interaction. First studies date back to 1928, where Irving Langmuir was the first to use the name ‘plasma’ to describe an ionized gas [18]. Although the setup is quite simple, innumerable phenomena can be observed in a plasma and dozens of different waves and instabilities can occur [19, 20, 21, 22, 23].

Plasma is found almost everywhere in the universe and in many applications on our planet: lighting, our atmosphere, gas-discharge lamps, lasers, stars, the interstellar medium and hopefully for clean future energy production. Fundamentally, all of them are supported by the electromagnetic force as a

long-range interaction. Everywhere, where the temperature is high enough to allow for some atoms to be ionized or in every setup where there is at least a portion of the particles in a free, charged state, plasma-like behaviour occurs. One can categorize plasma into a number of different classes depending on the fraction of ionization, the frequency of collisions, the strength of the coupling, the total charge and the magnetization of the medium. In the description of each of these classes, one has to rely on important length and time scales. If, from the equilibrium, the charge density is displaced by a small amount, the system will oscillate with the plasma frequency [24]

$$\omega_p^2 = \frac{nq^2}{m} \quad (5)$$

in natural units ($c = \hbar = \epsilon_0 = k_B = 1$, as will be adopted for the whole thesis), where n is the number density of the plasma particles, q is their charge, and m is their mass. If there are different species in the plasma, their contributions to the plasma frequency need to be summed up. In the most abundant case of a plasma consisting of electrons and protons, the contribution of the protons is negligible, and the term ‘electron plasma frequency’ is used synonymously with just the ‘plasma frequency’, which is a marker of typical time scales within the collective motion of the plasma particles. As such, all external influences need to happen on time scales much longer than the inverse plasma frequency in order to not dominate the plasma-like behaviour.

Another important definition is the thermal speed of each species inside the plasma:

$$V = \sqrt{\frac{T}{m}}, \quad (6)$$

where the temperature T is defined independent of thermal equilibrium from the mean square velocity. It describes the kinetic energy that is stored in the system.

If, in a plasma, there is an equal amount of positive and negative charges that redistribute once there is a disturbance from equilibrium to shield the electrostatic potential, the plasma is called quasi-neutral. The distance over which the potential is shielded and which will be the effective range of interaction is called the Debye-length [25]

$$\lambda_D = \sqrt{\frac{T}{nq^2}} = \frac{V}{\omega_p}. \quad (7)$$

The extension of a system should always be larger than this length to ensure that the interaction is complete and it can be properly described as a plasma.

Equally important is the so-called plasma parameter

$$\Lambda = \frac{4}{3}\pi n \lambda_D^3, \quad (8)$$

which is the number of particles contained inside a Debye-sphere. This number should be much larger than one, so that the plasma is only weakly coupled and there are no bound systems inside the plasma. Strongly coupled plasmas are hard to describe mathematically and will not be considered here. For further reading, please refer to the textbooks [19, 20, 21, 22, 23]

1.4 Waves and Instabilités

Various complex phenomena can arise in plasmas. The collective behaviour of the particles can lead to different waves and instabilities. They are classified depending on the setup and the frequencies and wavelengths that are considered. In linear theory, one can find the dispersion relation $\omega(\vec{k})$ of those setups and find the waves and instabilities as the solution $\omega = \omega_r + i\omega_i$. Because the waves evolve as $e^{-i(\omega t - \vec{x} \cdot \vec{k})}$, the real part of ω leads to oscillation, while a negative imaginary part leads to exponential damping of the waves. A positive imaginary part $\omega_i > 0$, however, leads to an exponential growth over time and is called ‘instability’. This does not mean that there will be a growth in energy, but instead some particular wave mode will consume the energy of other wave modes or kinetic energy until the instability saturates, which happens due to higher order turbulent terms.

To calculate the dispersion relation, one can reduce the problem to the calculation of the response tensor K , which is the dielectric tensor in natural units [19, 21]. To achieve this goal, one starts with the very basic equations that describe the problem: On the one hand, we have the Maxwell equations, which describe the forces between charged particles. In natural units, they read

$$\begin{aligned} \vec{\nabla} \cdot \vec{D} &= \rho \\ \vec{\nabla} \times \vec{E} &= -\frac{\partial \vec{B}}{\partial t} \\ \vec{\nabla} \cdot \vec{B} &= 0 \\ \vec{\nabla} \times \vec{H} &= \frac{\partial \vec{D}}{\partial t} + \vec{j}, \end{aligned} \quad (9)$$

where ρ is the density of free charges, \vec{j} is the density of free currents, \vec{E} is the electric field, \vec{B} the magnetic field, \vec{D} the displacement field and \vec{H} the

magnetizing field. All fields are functions of time t and position \vec{x} . On the other hand, we have the fluid equations, which describe the particle motion. They consist of the continuity equation

$$\frac{\partial n}{\partial t} + \vec{\nabla} \cdot (\vec{v}n) = 0 \quad (10)$$

and the momentum equation

$$mn \left(\frac{\partial \vec{v}}{\partial t} + \vec{v} \cdot \vec{\nabla} \vec{v} \right) = \vec{f}, \quad (11)$$

where m is the particle mass, n the number density, \vec{v} the flow velocity and \vec{f} some force density, here most importantly the Coulomb force

$$\vec{f} = \rho \left(\vec{E} + \vec{v} \times \vec{B} \right), \quad (12)$$

where $\rho = qn$. The problem is easily solvable in Fourier space because $\frac{\partial}{\partial t} \rightarrow -i\omega t$ and $\vec{\nabla} \rightarrow i\vec{k}$. We will also linearize the problem by assuming that all quantities are very close to equilibrium and there are only small, first-order corrections. In vacuum, $\vec{E} = \vec{D}$ and $\vec{H} = \vec{B}$, so that the Maxwell equations yield

$$\begin{aligned} \vec{k} \cdot \vec{E} &= -i\rho \\ \vec{k} \times \vec{E} &= \omega \vec{B} \\ \vec{k} \cdot \vec{B} &= 0 \\ \vec{k} \times \vec{B} &= -\omega \vec{E} - i\vec{j} \end{aligned} \quad (13)$$

All fields are functions of the frequency ω and the wave vector \vec{k} . While the third equation is redundant when computing the scalar product of the second equation with \vec{k} , one can replace the first one by the continuity equation that tells us, how ρ and \vec{j} are connected. We can, thus, treat \vec{j} as containing all the information we need, and insert equation two into equation four to get:

$$\frac{1}{\omega} \vec{k} \times (\vec{k} \times \vec{E}) + \omega \vec{E} = -i\vec{j}. \quad (14)$$

In linear theory, the current is given by $\vec{j} = \sigma \vec{E}$, where σ is the conductivity tensor. Furthermore, $\vec{a} \times (\vec{b} \times \vec{c}) = \vec{b}(\vec{a} \cdot \vec{c}) - \vec{c}(\vec{a} \cdot \vec{b})$, so that in index notation:

$$\left(\frac{1}{\omega} k_j k_i - \frac{1}{\omega} (k^2 - \omega^2) \delta_{ij} + i\sigma_{ij} \right) E_j = 0, \quad (15)$$

where δ_{ij} is the Kronecker- δ . Here we can define the response tensor as

$$K_{ij} = \delta_{ij} + \frac{i}{\omega} \sigma_{ij}, \quad (16)$$

so that

$$\left(\frac{k_i k_j - k^2 \delta_{ij}}{\omega^2} + K_{ij} \right) E_j \equiv \Lambda_{ij} E_j = 0. \quad (17)$$

Any solution needs to fulfil the condition $\det(\Lambda(\omega, \vec{k})) = 0$, which connects ω and \vec{k} . This is the dispersion relation. In this equation, the only dependence on the specific problem is hidden in K .

In unmagnetized plasmas, the only remarkable direction is the direction of wave propagation \vec{k} . Therefore, one can decompose the response tensor into a longitudinal part $K_L = \frac{1}{k^2} k_i K_{ij} k_j$ and a transverse part $K_T = \frac{1}{2}(K_{ij}\delta_{ij} - K_L)$, so that

$$k^2 K_{ij} = K_L k_i k_j + K_T(k^2 \delta_{ij} - k_i k_j). \quad (18)$$

Because the determinant is invariant under rotations, one can quickly see that if we rotate $\vec{k} = \vec{e}_z'$, the unity vector in z -direction, then $\Lambda = \text{diag}(K_T - N^2, K_T - N^2, K_L)$ and

$$\det \Lambda = K_L (K_T - N^2)^2 \stackrel{!}{=} 0 \quad (19)$$

with the refractive index $N = \frac{k}{\omega}$ and the two sub-equations

$$K_L = 0 \quad \text{and} \quad K_T = N^2. \quad (20)$$

These will be different branches of the dispersion relation, and each of these equations may still supply more than one branch.

So far, we still need to provide a way to calculate the response tensor. We will take a look at the Vlasov approach. In a general plasma, there will be a velocity distribution as well as a distribution in space, both of which will vary over time. This can be described by a distribution function $f(\vec{v}, \vec{x}, t)$ which follows - when collisions are negligible - the collisionless Boltzmann equation

$$\frac{df}{dt}(\vec{v}, \vec{x}, t) = \left(\frac{\partial}{\partial t} + \frac{d\vec{x}}{dt} \cdot \vec{\nabla} + \frac{d\vec{v}}{dt} \cdot \vec{\nabla}_v \right) f(\vec{v}, \vec{x}, t) = 0. \quad (21)$$

For our problem, we can insert $\frac{d\vec{x}}{dt} = \vec{v}$ and $\frac{d\vec{v}}{dt} = \frac{\vec{F}}{m} = \frac{q}{m}(\vec{E} + \vec{v} \times \vec{B})$, the Coulomb force, where \vec{E} and \vec{B} are given by Maxwell's equations. \vec{j} and ρ

can in turn be expressed by $f(\vec{v}, \vec{x}, t)$ as

$$\vec{j}(\vec{x}, t) = \sum_s q_s \int d\vec{v} \vec{v} f_s(\vec{v}, \vec{x}, t) \quad \rho(\vec{x}, t) = \sum_s q_s \int d\vec{v} f_s(\vec{v}, \vec{x}, t), \quad (22)$$

with a sum over the different species s . This leads to a complicated, nonlinear, integrodifferential equation for a coupled set of f_s , which is called the ‘Vlasov equation’. Again, we simplify by transforming into Fourier space:

$$0 = -i\omega f(\vec{v}, \vec{k}, \omega) + i(\vec{v} \cdot \vec{k}) f(\vec{v}, \vec{k}, \omega) + \frac{1}{(2\pi)^4} \int d\lambda \frac{q}{m} (\vec{E}(\omega_1, \vec{k}_1) + \vec{v} \times \vec{B}(\omega_1, \vec{k}_1)) \cdot \frac{\partial f}{\partial \vec{v}}(\vec{v}, \vec{k}_2, \omega_2), \quad (23)$$

where we used in the last term that the Fourier transform of a product is a convolution in Fourier space with $d\lambda = d\omega_1 d\vec{k}_1 d\omega_2 d\vec{k}_2 \delta(\omega - \omega_1 - \omega_2) \delta(\vec{k} - \vec{k}_1 - \vec{k}_2)$ with the delta function δ . We again use the second Maxwell equation and the bac-cab rule on the last term to gain

$$\frac{1}{(4\pi)^4} \int d\lambda \frac{q}{m\omega_1} (\omega_1 \vec{E} + \vec{k}_1 (\vec{v} \cdot \vec{E}) - (\vec{v} \cdot \vec{k}_1) \vec{E}) \cdot \frac{\partial f}{\partial \vec{v}}. \quad (24)$$

Let us now expand f in orders of \vec{E} . From the equation in proper space (Eq. (21)) we can simply see that the lowest order is only dependent on \vec{v} , because making a separable ansatz $f_0(\vec{v}, \vec{x}, t) = f_{0,v}(\vec{v}) f_{0,x}(\vec{x}) f_{0,t}(t)$:

$$\frac{1}{f_{0,t}(t)} \frac{\partial f_{0,t}(t)}{\partial t} + \frac{1}{f_{0,x}(\vec{x})} \vec{v} \frac{\partial f_{0,x}(\vec{x})}{\partial \vec{x}} = 0 \implies \frac{\partial f_{0,t}(t)}{\partial t} = \frac{\partial f_{0,x}(\vec{x})}{\partial \vec{x}} = 0, \quad (25)$$

meaning that $f_0(\vec{v}, \vec{x}, t)$ is not dependant on \vec{x} and t and, thus, in Fourier space $f_0(\vec{v}, \vec{k}, \omega) = f_{0,v}(\vec{v})(2\pi)^4 \delta(\vec{k}) \delta(\omega)$. The first order Vlasov equation in Fourier space then looks like

$$f_1(\vec{v}, \vec{k}, \omega) = \frac{-i}{\omega - \vec{k} \cdot \vec{v}} \frac{q}{m\omega} ((\omega - \vec{k} \cdot \vec{v}) \vec{E} + (\vec{v} \cdot \vec{E}) \vec{k}) \cdot \frac{\partial f_{0,v}(\vec{v})}{\partial \vec{v}}. \quad (26)$$

The first order current is

$$\vec{j} = \sum_s q_s \int d\vec{v} \vec{v} f_{1,s}(\vec{v}, \vec{k}, \omega) = \sigma \vec{E}, \quad (27)$$

and, thus, K can be identified from Eq. (16) as

$$K_{ij} = \delta_{ij} + \sum_s \frac{q_s^2}{m_s \omega^2} \int d\vec{v} v_i \left(\frac{\partial f_s(\vec{v})}{\partial v_j} + \frac{\vec{k} \cdot \frac{\partial f_s(\vec{v})}{\partial \vec{v}} v_j}{\omega - \vec{k} \cdot \vec{v}} \right). \quad (28)$$

So if one introduces a velocity distribution, one can calculate the dispersion relation of the problem via this formula and Eq. (19).

Some instabilities that often occur in plasmas will be introduced in Section 2.2.

2 Dark Matter Plasma

Let us now combine the two ideas established in the introduction: There are a lot of models to describe dark matter, and some of them work analogously to the standard model, especially U(1) models that imitate the electromagnetic force. The only differences that there may be in the description of dark matter compared to electromagnetic matter are the masses m_χ and the coupling g that is different from the electric base charge e and because it is not necessarily the photon that mediates the force between the charged particles. The new mediator may also be massive and there is an additional parameter m_A involved. Because it follows the same equations, dark matter should, in these models, also develop the same phenomena as baryons. One of these is the plasma state.

In this thesis, I will be mostly interested in the consequences of the dark matter plasma inside two colliding galaxy clusters - most famously the bullet cluster. Two streams of plasma crossing each other is a very interesting setup and leads to multiple possibly observable consequences. The most important ones will be discussed and compared to observations in this thesis. Parts of my thesis are following the argumentation of Lasenby, who considered this possibility first [26], but later on, I will improve his results in terms of motivation and precision.

Let us start with the important question of whether the idea of dark matter plasma is reasonable at all.

2.1 Is this a great idea? - Putting the dark matter on the plasma proof

I hereby claim that dark matter in the halo of a galaxy cluster can be described as a fully ionized, quasi-neutral, weakly coupled, unmagnetized and collisionless plasma. To prove that, one could take a first look if we would expect bound states, because as mentioned, plasma always needs to be at least partially dissociated. For a fully ionized plasma, we need the temperature to be much higher than the binding energy of dark matter. As we do not know much about the different dark contributors, which may be similarly complicated as our existing standard model, I will confine this calculation to two dark candidates, analogous to electrons and protons. These will be bound when the thermal energy of the environment is smaller than the energy of the bond. The binding energy of the (more general) hydrogen atom can be

calculated via

$$|E_n| = \frac{e^4 \mu}{32\pi^2} \frac{Z^2}{n^2}, \quad (29)$$

where e is the charge of the electron and proton, Z is the number of protons in the core and $\mu = \frac{Zm_e m_p}{m_e + Zm_p}$ is the effective mass of the system with m_e the mass of the electron and m_p the mass of the proton. Furthermore, $n \geq 1$ denotes the energy quantum number. The strongest bond is given for $n = 1$ and we can identify g with e and m_χ with m_e . The bond is more favourable if the dark proton is significantly heavier than the dark electron χ which is something I will assume in most of my thesis, so $\mu \approx m_\chi$. Z in this case describes the possibility that the dark protons do not need to have exactly the same charge as the dark electron (or several of them are bound together by some additional dark force similar to the strong force in standard model atoms). With Z arbitrarily high, the force can get arbitrarily strong. But for the purpose of this thesis we will assume that dark protons have the same charge as the dark electrons and that the hydrogen atom is the most common one in the universe, so $Z = 1$. This is motivated by the similarity to the standard model. We can set the gained binding energy equal to the temperature and solve for g to get

$$g \lesssim \left(32\pi^2 \frac{T}{m_\chi} \right)^{1/4}. \quad (30)$$

$V = \sqrt{\frac{T}{m_\chi}}$ is the thermal velocity of the dark matter halo and can be set equal to the velocity dispersion from Section 1.2. The result is $g \lesssim 42$. For a force that is responsible for the very low self-interaction of dark matter, one would at least expect it to be < 1 , so our dark matter will always be fully dissipated.

To ensure quasi-neutrality, the length scale of the plasma L , which is the size of a galaxy cluster in our case, must be much larger than the plasma Debye length

$$\lambda_D = \sqrt{\frac{T}{g^2 n}} = 75 \text{ m} \sqrt{\frac{0.1 \text{ GeV/cm}^3}{\rho_\chi}} \frac{V}{100 \text{ km/s}} \frac{m_\chi/g}{1 \text{ GeV}} \quad (31)$$

of the plasma with values from the core model of Section 1.2. The clusters are approximated by their cores and will have a constant density. This is compared to $R = 250$ kpc in Figure 2. Every coupling above the marked blue line leads to a quasi-neutral plasma.

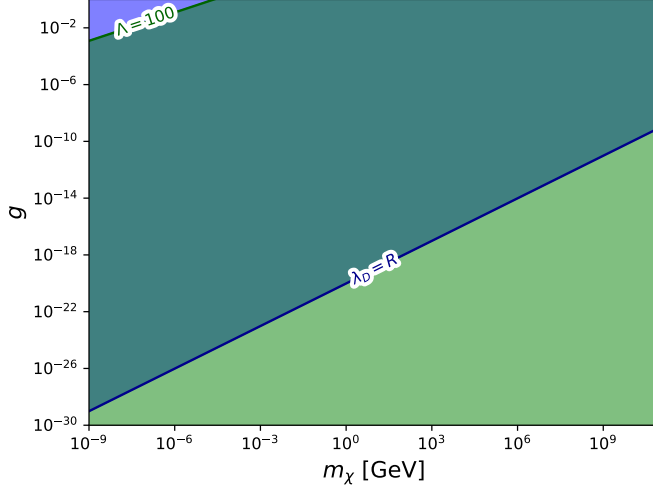


Figure 2: The mass-charge space of the dark matter plasma. The region where it is weakly coupled is coloured green; the region where it is quasi-neutral is blue. The dark green region, therefore, is the region with the desired plasma behaviour.

Additionally, the plasma will be weakly coupled as long as

$$\Lambda = \frac{4}{3} \pi n \lambda_D^3 = 1.77 \cdot 10^{11} \sqrt{\frac{0.1 \text{ GeV/cm}^3}{\rho_\chi}} \left(\frac{V}{100 \text{ km/s}} \right)^3 \frac{m_\chi^2/g^3}{1 \text{ GeV}^2} \gg 1. \quad (32)$$

This is true for everything below the green line in Figure 2. So the dark green region in the figure is where the plasma has the properties I claimed it to have in the beginning. This is a huge portion of the parameter space typically considered for dark matter. This means that basically all U(1)-dark-matter models have to be described as plasma in galaxy clusters. Because we do not know anything about the dark magnetic fields, I will demand them to vanish while the low collisionality is trivially fulfilled by the seldom self-interacting dark matter. It is certainly true that

$$\nu_c \ll \omega, \quad (33)$$

where ν_c is the rate of collisions between dark matter particles, and ω is the lowest important frequency for plasma processes.

Finally, something that does not need to be considered when calculating

standard-model plasmas is the finite mediator mass that limits the range of the interaction. In order to maintain collective behaviour, the range of the interaction must be a lot larger than the typical distance between particles. For our galaxy cluster setup, this reads:

$$\begin{aligned} \frac{1}{m_A} &\gg \left(\frac{m_\chi}{\rho_\chi}\right)^{1/3} \\ \implies m_A &\ll 9.15 \cdot 10^{-6} \text{ eV} \left(\frac{\rho_\chi}{0.1 \text{ GeV/cm}^3}\right)^{1/3} \left(\frac{m_\chi}{\text{GeV}}\right)^{-1/3}. \end{aligned} \quad (34)$$

Weakly depending on the dark matter mass χ , the mediator mass may not be arbitrarily high, but we will see later on that in the important cases these bounds are not worrisome. When every single one of these conditions is fulfilled, the dark matter halo can be considered as a dark matter plasma. For completeness, we can write down the plasma frequency that we will need later on:

$$\omega_p = \sqrt{\frac{g^2 n}{m_\chi}} = 4 \cdot 10^{-6} \text{ yr}^{-1} \sqrt{\frac{\rho_\chi}{0.1 \text{ GeV cm}^{-3}}} \frac{\text{GeV}}{m_\chi} \frac{g}{10^{-16}}. \quad (35)$$

2.2 Relevant Types of Instabilities

As I said, observations like the Bullet Cluster are my main point of interest. If dark matter is a plasma, then by the collision and passing through each other of the two dark matter halos, various instabilities could be induced. Let us simplify the setup in order to identify the most important one (for comparison, see [27]). Consider two infinite streams of (dark) plasma electrons that pass through each other. One of them will be called the ‘beam’ and the other one the ‘plasma’. This is because we will calculate in the reference frame where the two currents are equal:

$$n_b v_b = n_p v_p, \quad (36)$$

where n is the number density, v is the streaming velocity and b stands for ‘beam’, while p stands for ‘beam’. The one with the lower density will move faster and is, thus, the ‘beam’. There will be an amount of background ions that are considered motionless and will be sufficient to balance the charge so that our system is quasineutral. We can define some dimensionless quantities

to characterize the system:

$$\alpha \equiv \frac{n_b}{n_p}, \quad \gamma_b \equiv \frac{1}{\sqrt{1 - v_b^2}}, \quad \Omega_B \equiv \frac{\omega_c}{\omega_p}, \quad R \equiv \frac{m_e}{m_i} \quad x \equiv \frac{\omega}{\omega_p}, \quad \vec{Z} \equiv \frac{\vec{k}v_b}{\omega_p}, \quad (37)$$

$\alpha \leq 1$ being the density contrast, γ_b the relativistic γ -factor of the beam, $\omega_c = \frac{qB}{m_e}$ the cyclotron frequency of the plasma and Ω_B therefore a dimensionless measurement of the plasma magnetization given by the absolute value of the magnetic field B . R is the mass ratio that is supposed to be much smaller than 1, so that the ions stay immovable. q is the dark electron charge, m_e its mass and m_i the ion mass. The electron plasma frequency ω_p is given by $\omega_p^2 = \frac{q^2 n_p}{m_e}$.

For simplicity, we will take a look at the cold case first, thus, there will be no spread in velocity and calculations will be simple. For all purposes, the wavevector \vec{k} (and, thus, \vec{Z}) can be divided into the direction along the beam velocity, which we will call the z -direction, and the direction perpendicular, which will be the x -direction. So $k_y = 0$ without loss of generality. We can pretend to have three species in our setup: The beam electrons with velocity v_b , mass m_e and charge $-q$, the plasma electrons with $-v_p$, m_e and $-q$ and the ions with velocity 0, mass m_i and charge q . Their velocity distribution equals to

$$f_s(\vec{v}) = n_s \delta(\vec{v} - v_s \vec{e}_z), \quad (38)$$

where v_s is the species velocity and \vec{e}_z the unit vector in z -direction. The number density n_s is here because $\int d\vec{v} f(\vec{v}, \vec{x}, t) = n(\vec{x}, t)$. This equation can be inserted into Equation (19) with the relativistic replacement $p = \gamma mv$. We will take a look at the $k_x = 0$ case first. The longitudinal part of the dielectric tensor reads, when using partial integration to shift the derivative:

$$K_L = K_{zz} = 1 - \frac{q^2 n_b}{m_e \omega^2 \gamma_b^3} \left(1 + \frac{2k_z v_b}{\omega - k_z v_b} - \frac{k_z^2 v_b^2}{(\omega - k_z v_b)^2} \right) - \frac{q^2 n_p}{m_e \omega^2 \gamma_p^3} \left(1 - \frac{2k_z v_p}{\omega + k_z v_p} - \frac{k_z^2 v_p^2}{(\omega + k_z v_p)^2} \right) - \frac{q^2 (n_b + n_p)}{m_i \omega^2}. \quad (39)$$

Replacing with the dimensionless values defined above, we get:

$$K_L = 1 - \frac{\alpha \omega_p^2}{\omega^2 \gamma_b^3} \frac{\omega^2}{(\omega - k_z v_b)^2} - \frac{\omega_p^2}{\omega^2 \gamma_p^3} \frac{\omega^2}{(\omega + k_z v_p)^2} - R \frac{\omega_p^2}{\omega^2} (\alpha + 1) = 1 - \frac{\alpha}{(x - Z_z)^2 \gamma_b^3} - \frac{1}{(x + \alpha Z_z)^2 \gamma_p^3} - \frac{R(1 + \alpha)}{x^2} \stackrel{!}{=} 0, \quad (40)$$

where we used $\alpha = \frac{v_p}{v_b}$ from Eq. (36) for the plasma term. γ_p can be replaced with the same equation by $\gamma_p = 1/\sqrt{1 - \alpha^2(1 - \frac{1}{\gamma_b^2})}$. This dispersion relation is independent of Ω_B and therefore the magnetic field because wave perturbances are, in this case, only generated along the magnetic field direction. All of the magnetic field parallel to the beam direction is 0. Therefore, the branches of the instabilities that can be calculated from this equation are called the electrostatic modes. There are two of them at different wavelengths that are maximally growing: the Two-Stream instability and the Buneman instability.

The Two-Stream instability arises from the interaction of the two crossing streams of particles. For a diluted beam with $\alpha \ll 1$, the maximum growth rate can be found at a normalized wavenumber of $Z_z = 1$ and it grows with

$$\delta \equiv \frac{\omega_i}{\omega_p} = \text{Im}[x] = \frac{\sqrt{3}}{2^{4/3}} \frac{\alpha^{1/3}}{\gamma_b}. \quad (41)$$

I will return to this formula in Section 3.1 to explain the full solution of the dispersion relation and provide an overview of different approximations. The Buneman instability arises from the interaction of the beam with the background ions and can be found at smaller wavelengths $Z_z = \frac{1}{\alpha}$. It grows with [28]

$$\delta = \frac{\sqrt{3}}{2^{4/3}} R^{1/3}. \quad (42)$$

There will be different regions in the parameter space where the Buneman instability is dominating over the two-stream instability and vice versa. In this case, the two-stream instability is dominating for

$$\frac{\alpha}{\gamma_b} > R. \quad (43)$$

For example, when looking at beams with infinitely massive ions, the two-stream instability will always grow fastest. But when considering non-relativistic beams of standard model electrons and background protons with $R = \frac{1}{1836}$, the Buneman instability dominates whenever $\alpha \lesssim 10^{-3}$. When α gets closer to 1, the plasma and the beam are symmetric and the physical interpretation of the system is not as easy, because both instabilities arise at equal wavelengths and merge. The calculations are still valid, but depending on the value of $\gamma_b^3 R$, the dominating behaviour might be different.

The full dispersion relation from the full response tensor can be calculated via Mathematica, which Bret did in 2007 [29], and the result is given in the appendix of [27]. One can numerically step through the parameter space

$(\alpha, \gamma_b, \Omega_B, R)$ and identify the fastest growing instability for the full 2d- k -space. Take a look at Figure 3.

The two figures on the left show different mass ratios R . Take a look at the upper left plot which corresponds to the actual electron-proton mass-ratio. The waves that are along the direction of the beam are to be found at the bottom of the plot where $Z_x = 0$. Here, we can identify the two-stream instability at about $Z_z = 1$ and the Buneman instability at $Z_z = \frac{1}{\alpha} = 10$. One can see that they both expand continuously into the space where $k_x \neq 0$. This area is generally called the ‘oblique’ modes, because the waves move oblique to the stream. The case where waves travel orthogonally to the beam direction, meaning $Z_z = 0$ is called the ‘filamentation’ mode. This is due to its appearance in 3d-PIC simulations. The filamentation mode can be seen in the upper right plot. If there is no magnetic field, there is only the two-stream instability, the filamentation instability and one oblique branch connecting those two (see also [30]). Therefore, this branch is called the ‘Oblique $_{B_0}$ ’-branch. Also, the Buneman instability is visible, which is different from the lower left plot where $R = 0$. This is also obvious from the dispersion relation 40 and the interpretation of the Buneman instability. When the magnetic field is bigger than 0, two different oblique modes are visible. Take a look at the left of the lower right plot. Here, there are still remnants of the oblique mode that was once connected to the filamentation instability. But there, also, is a new branch that increases with Z_x and is maximal at $Z_x = \infty$. These new modes are called ‘upper-hybrid-like’ while the remnants that decrease with γ_b are just called ‘Oblique’. In the left plot, the upper-hybrid-like mode can be identified, as well as the rightmost branch. For very high values of the magnetic field, there could be ‘Bell’ instabilities from the transverse part of the response tensor at low Z_z , but they are not visible in the plots and usually stay low in growth rate.

Now one can look for the region of the plot where there is the highest growth rate and identify the instability that is responsible by its wavelength and direction. This is equivalent to just comparing all the different maximum growth rates and determining the biggest one for certain regions of the parameter space as explained in the simple case of two-stream and Buneman above. This was done in [27], and the result is shown in Figure 4.

First of all, let us try to find the plots from Figure 3 in this figure. In the upper left plot, there we had $\Omega_B = 3$ and $R = 1/1836$, so we need to look into the middle plot of the first row of Figure 4. At the point $\alpha = 0.1$ and $\gamma_b = 2$, we can indeed see, that it is the two-stream instability that dominates. This one had the highest growth rate in Figure 3’s upper left plot

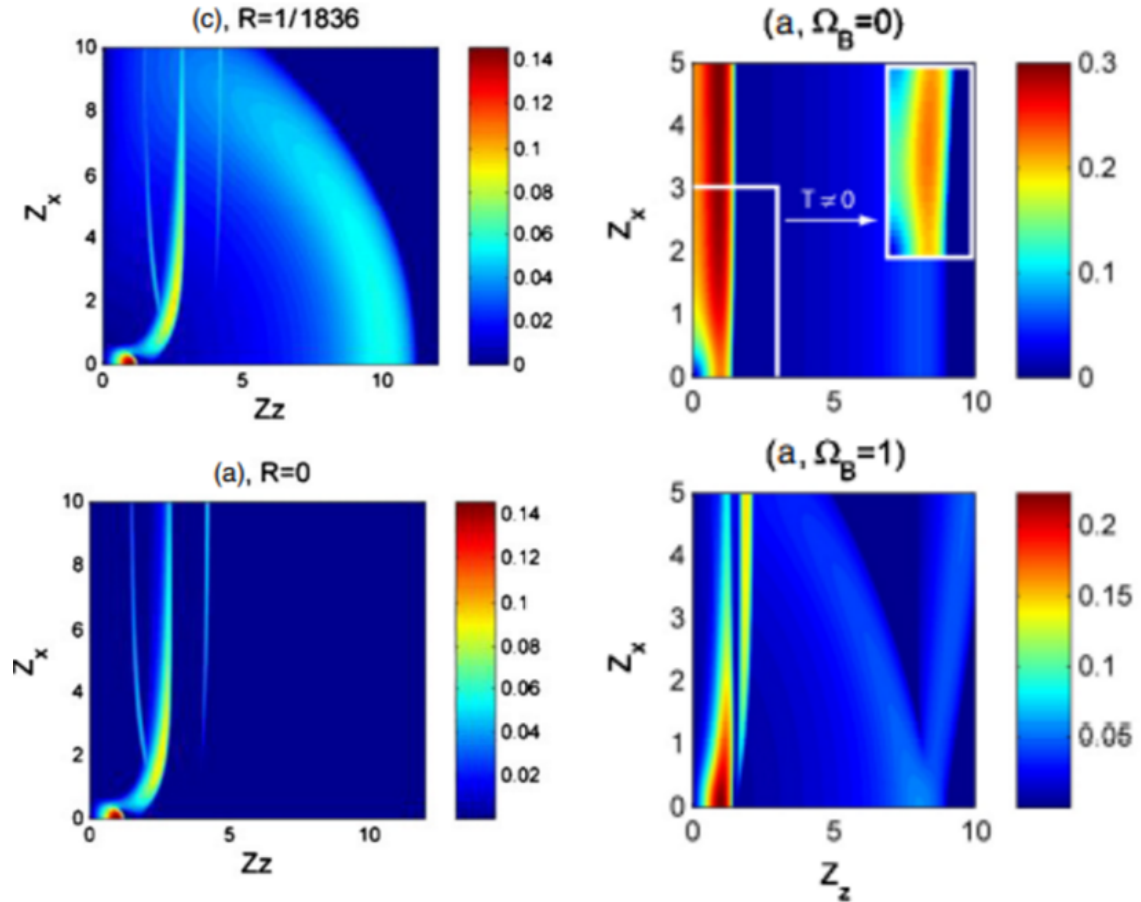


Figure 3: The maximum growth rate $\delta = \text{Im}[x]$ as a function of the normalized wavenumber Z . One can get this plot as the solution of Eq. (40) with the biggest imaginary part. For the two plots on the left, the parameters $\alpha = 0.1$, $\gamma_b = 2$ and $\Omega_B = 3$ are used. The upper one shows the standard model case with $R = 1/1836$, while the lower one shows the case for immovable ions ($R = 0$). On the right, both figures show the parameters $\alpha = 1/8$, $\gamma_b = 1.34$ and $R = 1/1836$. The upper one is without magnetic field and the lower one shows $\Omega_B = 1$. The figures are taken from [27].

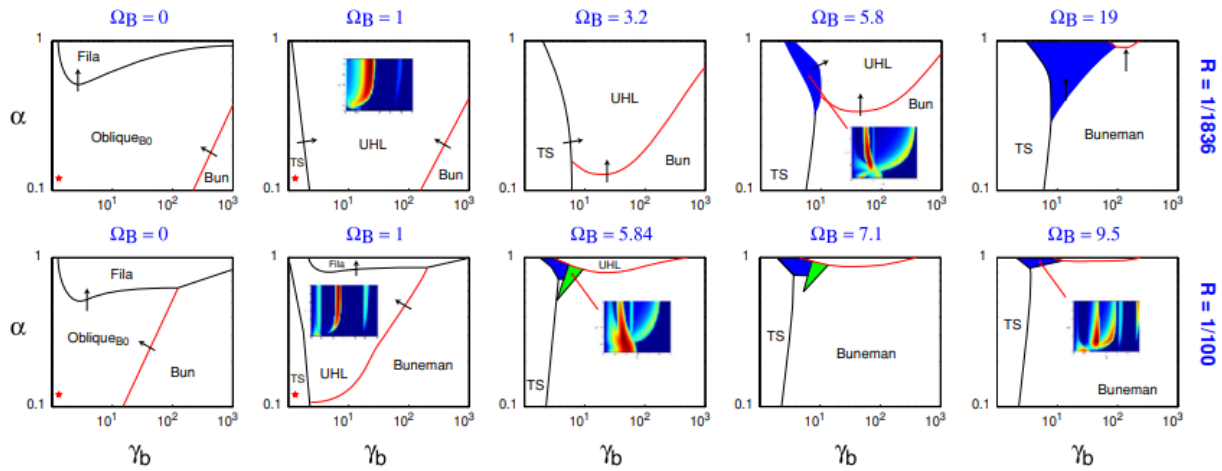


Figure 4: The instability that grows fastest at different points of the $(\alpha, \gamma_b, \Omega_B, R)$ -parameter space. Each of this plots shows γ_b on the x -axis and α on the y -axis, while the magnetic field increases from left to right. The upper line shows a higher mass difference than the lower one. The arrows indicate how the borders between instability dominations move with increasing Ω_B . The inset plots show the same as Figure 3 for the corresponding values of the parameters to emphasize where the important instability lies. ‘TS’ is short for two-stream, ‘UHL’ stands for upper-hybrid-like, ‘Bun’ means Buneman and ‘Fila’ the filamentation instability. Figure from [27].

(visible in dark red). In the upper right plot, it should be the Oblique _{B_0} -mode that is dominating. We find this in the upper plot of the first column in Figure 4 for $\alpha = 0.125$ and $\gamma = 1.34$. It is important to notice at this point that for $\gamma_b = 1$, the Oblique _{B_0} -mode is exactly equal to the two-stream instability, even in the case without B -field.

After understanding how the method works, one can make some general observations: The non-relativistic region is always dominated by the two-stream instability. For a symmetric setup, the filamentation instability dominates for low magnetic fields, but for high magnetic fields, the upper-hybrid-like modes grow fastest. As long as $R > 0$, the Buneman instability dominates for relativistic, diluted beams.

For my project, the most important regime will be the non-relativistic one, as the velocity of the Bullet Cluster is clearly lower than c . The densities of the two clusters will also be similar, because they have a similar mass.¹ When considering dwarf galaxies passing through bigger clusters, there may be a lower density contrast. But we are not concerned by the value of α , because for a non-relativistic beam with $\gamma_b = 1$, it is always the two-stream instability that is the fastest growing one and therefore the dominating source of visual change. Even when we neglect magnetic fields for simplicity, we can choose between the Oblique _{B_0} -mode and the two-stream instability. But because the two-stream instability has easy physical interpretations and can be easily calculated, this is the one that I will closely examine in the following.

An extension of this growth rate comparison for streams with a non-zero temperature can be found in [31]. The domination of the two-stream instability for non-relativistic velocities will sustain for the warm case.

¹This is, of course, not always true, because both clusters have a dark matter density profile. When different regions of the clusters have crossed each other, there may be locally different values of α .

3 The Linear Two-Stream Instability

The two-stream instability occurs when there are two plasmas with a relative velocity that are colliding [32]. It dissipates directed beam energy into thermal energy after the exponential growth of certain wave modes.

3.1 The Cold Case

When we want to examine the two-stream instability, we can consider the case of infinitely massive ions and take a look at the K_{zz} part of the dielectric tensor as we did above. The dispersion equation yields

$$0 = 1 - \frac{\alpha}{(x - Z_z)^2 \gamma_b^3} - \frac{1}{(x + \alpha Z_z)^2 \gamma_p^3} \quad (44)$$

with $\gamma_p = 1/\sqrt{1 - \alpha^2(1 - \frac{1}{\gamma_b^2})}$. For simplification we will only take a look at the non-relativistic two-stream instability, so $\gamma_b = \gamma_p = 1$. There are several approximate solutions to this problem - all of them consider the case of a very diluted beam, meaning $\alpha \ll 1$, so that the dispersion equation only reads

$$1 = \frac{1}{x^2} + \frac{\alpha}{(x - Z_z)^2}, \quad (45)$$

which is still complicated enough - too complicated to write down all the steps that lead to the approximations written down. They can be looked up in the corresponding pieces of writing. Melrose takes a closer look at $Z_z \approx 1$ [21]:

$$\delta \equiv \text{Im}[x] = \frac{\sqrt{3}}{2^{4/3}} \alpha^{1/3} \left((\Delta_+(Z_z - 1))^{2/3} - (\Delta_-(Z_z - 1))^{2/3} \right) \quad (46)$$

with

$$\Delta_{\pm}(y) = 2\sqrt{\frac{1}{16} - \frac{y^3}{54\alpha}} \pm \frac{1}{2}. \quad (47)$$

This solution has been brought to a form where it is easily comparable with the one by Schlickeiser. It reaches a maximum at $Z_z = 1$ with a value of $\delta = \frac{\sqrt{3}}{2^{4/3}} \alpha^{1/3}$, which corresponds to the Equation (41). For high values of Z_z , it quickly decreases until it is not real anymore (which δ should be by definition), while it is constant for low values of Z_z . Schlickeiser uses the approximation $|x| \gg \sqrt{\alpha}$, ending up with [22]

$$\delta = \frac{\sqrt{3}}{2^{4/3}} \alpha^{1/3} \left((\Delta_+(|1 - Z_z|))^{2/3} - (\Delta_-(|1 - Z_z|))^{2/3} \right), \quad (48)$$

which is very similar, except that it is also decreasing for low Z_z . Schlickeiser also provides a calculation for the real part of the frequency, which reads

$$\text{Re}[x] = \frac{|1 - Z_z|}{3} - \frac{1}{2^{4/3}} \alpha^{1/3} \left((\Delta_+ (|1 - Z_z|))^{2/3} + (\Delta_- (|1 - Z_z|))^{2/3} \right). \quad (49)$$

At $Z_z = 1$, this is about $\frac{\alpha^{1/3}}{2^{4/3}}$, so close to $Z_z = 1$, $|x| = \left(\frac{\alpha}{2}\right)^{1/3}$. Anderson, Fedele and Lisak (AFL) presented a solution for $\text{Re}[x] \approx \frac{2Z_z}{1+\alpha^{2/3}}$ and found [33]

$$\delta = \frac{4Z_z^2 \alpha^{1/3}}{\sqrt{3}(1 + \alpha^{2/3})^{5/2}} \sqrt{\frac{(1 + \alpha^{2/3})^3}{4Z_z^2} - 1}. \quad (50)$$

This is slightly different and yields another maximum value, but instead the slope of the real and imaginary part are linear for small Z_z . For $Z_z > 1$, this decreases until it is not useful anymore. I have solved the dispersion relation exactly with Mathematica (but it is too lengthy to write it down) and plotted the solution for δ and $\text{Re}[x]$ together with the different approximations for different values of α . They are shown in Figure 5.

Because all of the approximation started from the diluted dispersion relation, they of course fail to reproduce the pink true solution for $\alpha = 1$ even for the region in which they are supposed to work (which is $Z_z \approx 1$ for Schlickeiser and Melrose). With the exception of $\alpha = 1$, where the real part of the frequency is always 0, the AFL solution primarily reproduces the slope of both the frequency and the growth rate. While the green curve of Schlickeiser is very similar to Melrose (which is clear from the form of equations (46) and (48)) and describes the region around $Z_z = 1$ very well, its real part is quite a bad approximation and I do not know why this is the case.

The most important conclusion from this is the understanding of Equation (41) from the two first approximations that smoothly snuggle to the pink curve in the right plot of Figure 5. The cold two-stream instability is also a limiting case for the following considerations.

3.2 The Warm Case

3.2.1 Calculating the Dispersion Relation in the Vlasov Approach

When we introduce a temperature in each of the streams, we need to recalculate the dispersion relation from Equation (28), which I write down again

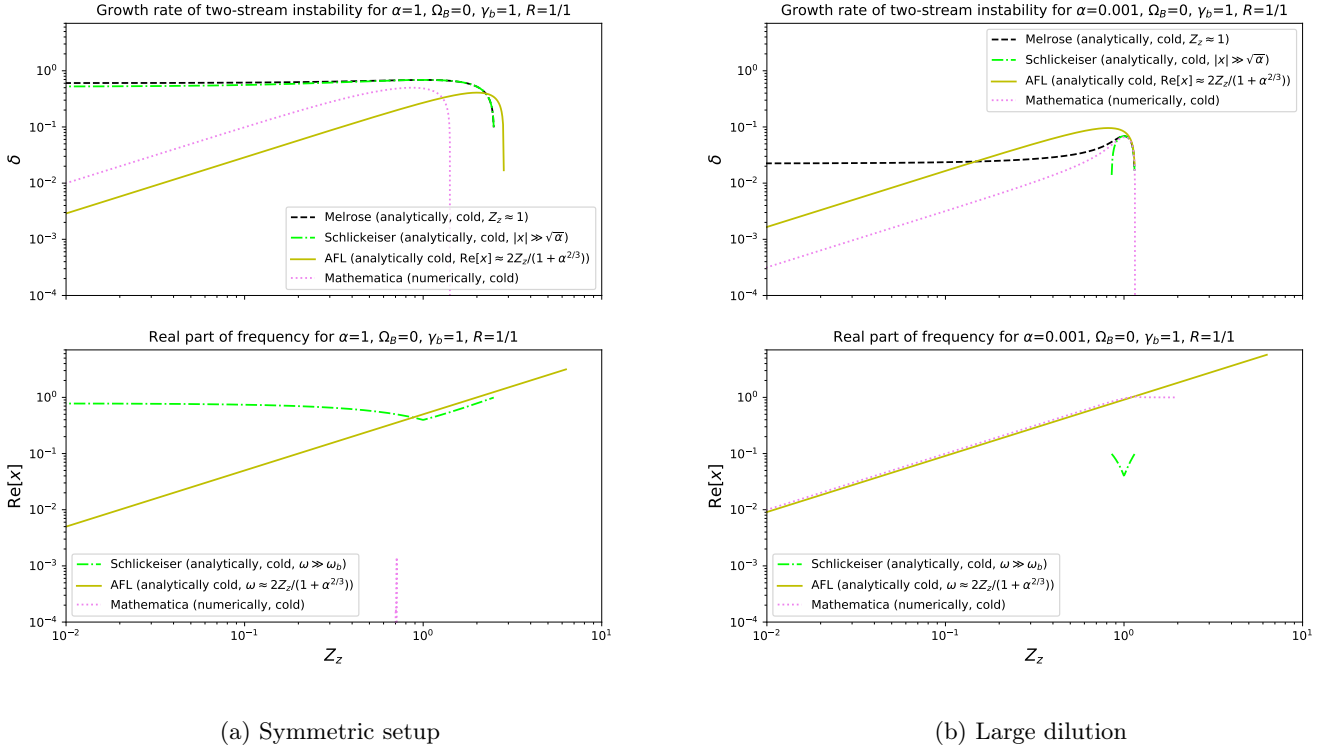


Figure 5: Comparison of the different approximations to the dispersion relation of the cold two-stream instability and the full numerical solution. The upper plots show the imaginary part and the lower plots show the real part of the frequency as a function of normalized wave number. The left plots have $\alpha = 0$, while the plots on the right depict $\alpha = 0.001$. Eq. (46) is represented by the black dashed line, the green dash-dotted line belongs to Eq. (48), and the ochre line belongs to Eq. (50). The dotted pink line is the numerical solution.

for convenience (Compare also [21]):

$$K_{ij} = \delta_{ij} + \sum_s \frac{q^2 m^2}{\omega^2} \int d^3 v \frac{v_i}{\omega - \vec{k} \cdot \vec{v}} \left((\omega - \vec{k} \cdot \vec{v}) \delta_{jm} + k_m v_j \right) \partial_{v_m} f(\vec{v}). \quad (51)$$

For two streams of the same particles, we use the velocity distribution

$$f(\vec{v}) = \frac{1}{2} \frac{n}{(2\pi)^{3/2} m^3 V^3} e^{-\frac{(\vec{v} + \vec{v}_0)^2}{2V^2}} + \frac{1}{2} \frac{n}{(2\pi)^{3/2} m^3 V^3} e^{-\frac{(\vec{v} - \vec{v}_0)^2}{2V^2}} \equiv f_+ + f_-, \quad (52)$$

where $V = \sqrt{\frac{T}{m}}$, the thermal velocity, is the variance of the Boltzmann distribution, and \vec{v}_0 is the streaming velocity along the z -axis.

One could also consider different temperatures V_\pm , streaming velocities $v_{0,\pm}$ or densities n_\pm with $n_+ + n_- = n$, but we don't need this right now. Because the structure is the same, we can calculate both terms at once and add them up at the end.

$$\begin{aligned} K_{ij}^\pm &= \sum_s \frac{q^2 m^2}{\omega^2} \int d^3 v \frac{v_i}{\omega - \vec{k} \cdot \vec{v}} \left((\omega - \vec{k} \cdot \vec{v}) \delta_{jm} + k_m v_j \right) \partial_{v_m} f_\pm \\ &= - \sum_s \frac{q^2 n}{m \omega^2} \frac{1}{2(2\pi)^{3/2} V^5} \\ &\quad \times \int d^3 v \frac{v_i}{\omega - \vec{k} \cdot \vec{v}} \left((\omega - \vec{k} \cdot \vec{v}) \delta_{jm} + k_m v_j \right) \cdot (v_m \pm v_{0m}) e^{-\frac{(\vec{v} \pm \vec{v}_0)^2}{2V^2}}. \end{aligned} \quad (53)$$

We can work out the integral as

$$\begin{aligned} &\int d^3 v \frac{v_i}{\omega - \vec{k} \cdot \vec{v}} \left((\omega - \vec{k} \cdot \vec{v}) \delta_{jm} + k_m v_j \right) \cdot (v_m \pm v_{0m}) e^{-\frac{(\vec{v} \pm \vec{v}_0)^2}{2V^2}} \\ &= \int d^3 v \frac{v_i}{\omega - \vec{k} \cdot \vec{v}} \left((\omega - \vec{k} \cdot \vec{v}) v_j + (\vec{k} \cdot \vec{v}) v_j \pm (\omega - \vec{k} \cdot \vec{v}) v_{0j} \pm (\vec{k} \cdot \vec{v}_0) v_j \right) e^{-\frac{(\vec{v} \pm \vec{v}_0)^2}{2V^2}} \\ &= \int d^3 v \left(\frac{\omega v_i v_j}{\omega - \vec{k} \cdot \vec{v}} \pm v_i v_{0j} \pm \frac{(\vec{k} \cdot \vec{v}_0) v_i v_j}{\omega - \vec{k} \cdot \vec{v}} \right) e^{-\frac{(\vec{v} \pm \vec{v}_0)^2}{2V^2}} \\ &= \int d^3 v \left(\left(1 \pm \frac{\vec{k} \cdot \vec{v}_0}{\omega} \right) \frac{\omega v_i v_j}{\omega - \vec{k} \cdot \vec{v}} \pm v_i v_{0j} \right) e^{-\frac{(\vec{v} \pm \vec{v}_0)^2}{2V^2}}. \end{aligned} \quad (54)$$

The second term can be solved as

$$\begin{aligned} & \pm v_{0j} \frac{1}{(2\pi)^{3/2} V^3} \int d^3v v_i e^{-\frac{(\vec{v} \pm \vec{v}_0)^2}{2V^2}} \\ &= \pm v_{0j} \cdot (\mp v_{0i}) \\ &= -v_{0i} v_{0j}. \end{aligned} \quad (55)$$

The first part can be solved after choosing $\vec{k} = k\vec{e}_z$ and taking the longitudinal direction (remember that the two-stream instability is mainly found as an electrostatic mode):

$$\begin{aligned} & \frac{\omega}{(2\pi)^{3/2} V^3} \int d^3v \frac{1}{\omega - \vec{k} \cdot \vec{v}} \left(\frac{\vec{k} \cdot \vec{v}}{k} \right)^2 e^{-\frac{(\vec{v} \pm \vec{v}_0)^2}{2V^2}} \\ &= -\frac{\omega}{k^2} \frac{1}{(2\pi)^{3/2} V^3} \int d^3v \left(\frac{\omega^2 - (\vec{k} \cdot \vec{v})^2}{\omega - \vec{k} \cdot \vec{v}} - \frac{\omega^2}{\omega - \vec{k} \cdot \vec{v}} \right) e^{-\frac{(\vec{v} \pm \vec{v}_0)^2}{2V^2}} \\ &= -\frac{\omega}{k^2} \frac{1}{(2\pi)^{3/2} V^3} \int d^3v \left(\omega + \vec{k} \cdot \vec{v} - \frac{\omega^2}{\omega - \vec{k} \cdot \vec{v}} \right) e^{-\frac{(\vec{v} \pm \vec{v}_0)^2}{2V^2}} \\ &= -\frac{\omega}{k^2} \left(\omega \mp \vec{k} \cdot \vec{v}_0 - \frac{\omega^2}{(2\pi)^{3/2} V^3} \int d^3v \frac{1}{\omega - \vec{k} \cdot \vec{v}} e^{-\frac{(\vec{v} \pm \vec{v}_0)^2}{2V^2}} \right) \\ &= -\frac{\omega}{k^2} \left(\omega \mp \vec{k} \cdot \vec{v}_0 - \frac{\omega^2}{\sqrt{2\pi} V} \int dv_z \frac{1}{\omega - k(v_z \mp v_{0z})} e^{-\frac{v_z^2}{2V^2}} \right) \\ &= -\frac{\omega}{k^2} \left(\omega \mp \vec{k} \cdot \vec{v}_0 + \omega^2 \frac{1}{\sqrt{\pi}} \frac{1}{\sqrt{2} V k} \int dt \frac{1}{t - \left(\frac{\omega}{\sqrt{2} V k} \pm \frac{v_{0z}}{\sqrt{2} V} \right)} e^{-t^2} \right) \\ &\equiv \tilde{K}_L^\pm. \end{aligned} \quad (56)$$

We introduce $z_\pm = \frac{\omega \mp \vec{k} \cdot \vec{v}_0}{\sqrt{2} V k}$ and the plasma dispersion function

$$\Phi(z) = -\frac{z}{\sqrt{\pi}} \int dt \frac{1}{t - z} e^{-t^2} \quad (57)$$

to obtain

$$\tilde{K}_L^\pm = -\frac{\omega^2}{k^2} \left(1 \mp \frac{\vec{k} \cdot \vec{v}_0}{\omega} - \frac{\omega}{\sqrt{2} V k} \frac{\Phi(z_\pm)}{z_\pm} \right). \quad (58)$$

The plasma dispersion function is an important complex function in plasma physics that always appears when there are Maxwell distributions involved.

Properties of $\Phi(z)$ are listed in Section A of the appendix.
Putting things back together yields:

$$\begin{aligned}
K_L^\pm &= - \sum_s \frac{\omega_p^2}{\omega^2} \frac{1}{2V^2} \left(\left(1 \pm \frac{\vec{k} \cdot \vec{v}_0}{\omega} \right) \tilde{K}_L^\pm - \left(\frac{\vec{k} \cdot \vec{v}_0}{k} \right)^2 \right) \\
&= \sum_s \frac{\omega_p^2}{2V^2 k^2} \left(1 - \left(\frac{\vec{k} \cdot \vec{v}_0}{\omega} \right)^2 - \left(1 \pm \frac{\vec{k} \cdot \vec{v}_0}{\omega} \right) \frac{\omega}{\sqrt{2}Vk} \frac{\Phi(z_\pm)}{\frac{\omega \pm \vec{k} \cdot \vec{v}_0}{\sqrt{2}Vk}} + \left(\frac{\vec{k} \cdot \vec{v}_0}{\omega} \right)^2 \right) \\
&= \sum_s \frac{\omega_p^2}{2V^2 k^2} (1 - \Phi(z_\pm)),
\end{aligned} \tag{59}$$

with $\omega_p^2 = \frac{q^2 n}{m}$ and

$$\begin{aligned}
K_L &= 1 + K_L^+ + K_L^- \\
&= 1 + \sum_s \frac{\omega_p^2}{V^2 k^2} \left(1 - \frac{1}{2} (\Phi(z_+) + \Phi(z_-)) \right).
\end{aligned} \tag{60}$$

Note that the normalization plasma frequency differs from the cases before, because the density of a beam is $n/2$. Of course, if we are only considering one type of streaming dark matter particle, we can omit the sum over species s . We realize that for each stream there is a plasma dispersion function weighted with the part of the total number density that it consists of. Its argument is always the phase speed - the Doppler-shifted frequency over the wave number - divided by the thermal velocity (and $\sqrt{2}^2$).

3.2.2 Transformations of Coordinate Systems

The same result can be obtained when using the formula for Galilean shifts from the unprimed to the primed system moving with \vec{v}_0 [34]:

$$\begin{aligned}
\alpha'_{ij}(\omega', \vec{k}') &= \alpha_{ij}(\omega' - \vec{k}' \cdot \vec{v}_0, \vec{k}') + \frac{v_{0i} k'_r \alpha_{rj}(\omega' - \vec{k}' \cdot \vec{v}_0, \vec{k}')}{\omega' - \vec{k}' \cdot \vec{v}_0} \\
&\quad + \frac{v_{0j} k'_s \alpha_{is}(\omega' - \vec{k}' \cdot \vec{v}_0, \vec{k}')}{\omega' - \vec{k}' \cdot \vec{v}_0} + \frac{v_{0i} v_{0j} k'_r k'_s \alpha_{rs}(\omega' - \vec{k}' \cdot \vec{v}_0, \vec{k}')}{(\omega' - \vec{k}' \cdot \vec{v}_0)^2},
\end{aligned} \tag{61}$$

²Some people, therefore define $V^2 = 2 \frac{T}{m}$

where $\vec{k}' = \vec{k}$, $\omega' = \omega + \vec{k} \cdot \vec{v}_0$ and $j_i = \alpha_{ij} A_j$ the spacial part of the relation between current density \vec{j} and potential \vec{A} . This relates to the response tensor like

$$K = \mathbb{1} + \frac{i}{\omega} \sigma \quad \sigma = \frac{i}{\omega} \alpha, \quad (62)$$

where in the system with the Maxwell distribution without velocity shift there is [21]

$$K_L = 1 + \sum_s \frac{\omega_p^2}{V^2 k^2} \left(1 - \Phi(z(\omega, \vec{k})) \right), \quad (63)$$

with $z(\omega, \vec{k}) = \frac{\omega}{\sqrt{2V}k}$. The calculation for this is way simpler than the one above and can also be seen from Equation (60) (or any other step beforehand) by setting v_0 to 0. Transforming the longitudinal part of the response tensor will result in

$$\begin{aligned} K'_L &= 1 - \frac{1}{\omega'^2} \alpha'_L(\omega', \vec{k}') \\ &= 1 - \frac{1}{\omega'^2} \alpha_L(\omega' - \vec{k}' \cdot \vec{v}_0, \vec{k}') \left(1 + \frac{2\vec{k} \cdot \vec{v}_0}{\omega' - \vec{k}' \cdot \vec{v}_0} + \frac{(\vec{k} \cdot \vec{v}_0)^2}{(\omega' - \vec{k}' \cdot \vec{v}_0)^2} \right) \\ &= 1 + \frac{(\omega' - \vec{k}' \cdot \vec{v}_0)^2}{\omega'^2} \sum_s \frac{\omega_p^2}{V^2 k'^2} \left(1 - \Phi(z(\omega' - \vec{k}' \cdot \vec{v}_0, \vec{k}')) \right) \left(\frac{\omega'^2}{(\omega' - \vec{k}' \cdot \vec{v}_0)^2} \right) \\ &= 1 + \sum_s \frac{\omega_p^2}{V^2 k'^2} (1 - \Phi(z_-)), \end{aligned} \quad (64)$$

where $\alpha_L(\omega, \vec{k}) = \frac{k_i k_j}{k^2} \alpha_{ij}(\omega, \vec{k}) = -\omega^2 \sum_s \frac{\omega_p^2}{V^2 k^2} \left(1 - \Phi(z(\omega, \vec{k})) \right)$. The result for two streams in opposing directions that are sharing the number density n equally can easily be deduced and compared with Eq. (60).

Analogously, one finds for the transverse part:

$$K_T = 1 - \sum_s \frac{\omega_p^2}{\omega^2} \Phi(z(\omega, \vec{k})) = 1 - \frac{1}{\omega^2} \alpha_T, \quad (65)$$

with $\alpha_T(\omega, \vec{k}) = \frac{1}{2}(\delta_{ij} - \frac{k_i k_j}{k^2})\alpha_{ij}(\omega, \vec{k}) = \sum_s \omega_p^2 \Phi(z(\omega, \vec{k}))$ and $\alpha_{ij} = \alpha_L \frac{k_i k_j}{k^2} + \alpha_T \left(\delta_{ij} - \frac{k_i k_j}{k^2} \right)$. Writing $\alpha_X = \alpha_X(\omega' - \vec{k}' \cdot \vec{v}_0, \vec{k}')$, one gets

$$\begin{aligned}
2\alpha'_T(\omega', \vec{k}') &= \alpha'_{ii}(\omega', \vec{k}') - \alpha'_L(\omega', \vec{k}') \\
&= \alpha_L + 2\alpha_T + 2 \frac{v_{0i} k'_r \left(\alpha_L \frac{k_r k_i}{k'^2} + \alpha_T \left(\delta_{ir} - \frac{k_r k_i}{k'^2} \right) \right)}{\omega' - \vec{k}' \cdot \vec{v}_0} + \frac{v_0^2 k'_r (\alpha_L k'_r + \alpha_T (\delta_{rs} k'_s - k'_r))}{(\omega' - \vec{k}' \cdot \vec{v}_0)^2} \\
&\quad - \alpha_L \frac{\omega'^2}{(\omega' - \vec{k}' \cdot \vec{v}_0)^2} \\
&= 2\alpha_T + \frac{\omega'^2 - 2\omega' (\vec{k}' \cdot \vec{v}_0) + (\vec{k}' \cdot \vec{v}_0)^2 + 2\omega' (\vec{k}' \cdot \vec{v}_0) - 2(\vec{k}' \cdot \vec{v}_0)^2 + k'^2 v_0^2 - \omega'^2}{(\omega' - \vec{k}' \cdot \vec{v}_0)^2} \alpha_L \\
&= 2\alpha_T + \frac{k'^2 v_0^2 - (\vec{k}' \cdot \vec{v}_0)^2}{(\omega' - \vec{k}' \cdot \vec{v}_0)^2} \alpha_L.
\end{aligned} \tag{66}$$

It follows:

$$\begin{aligned}
K'_T &= 1 - \frac{1}{2\omega'^2} \left(2\alpha_T(\omega' - \vec{k}' \cdot \vec{v}_0, \vec{k}') + \frac{|\vec{k}' \times \vec{v}_0|^2}{(\omega' - \vec{k}' \cdot \vec{v}_0)^2} \alpha_L(\omega' - \vec{k}' \cdot \vec{v}_0, \vec{k}') \right) \\
&= 1 - \sum_s \frac{\omega_p^2}{\omega'^2} \left(\Phi(z_-) - \frac{|\vec{k}' \times \vec{v}_0|^2}{2V^2 k'^2} (1 - \Phi(z_-)) \right).
\end{aligned} \tag{67}$$

3.2.3 Numerical Evaluation of the Warm Dispersion Relation

The dispersion relation can be found from Equation (19). This can be evaluated numerically. The plasma dispersion function can be divided into a real and an imaginary part like [21]

$$\Phi(z) = \phi(z) - i\sqrt{\pi}ze^{-z^2}, \tag{68}$$

with

$$\phi(z) = 2ze^{-z^2} \int_0^z dt e^{t^2}, \tag{69}$$

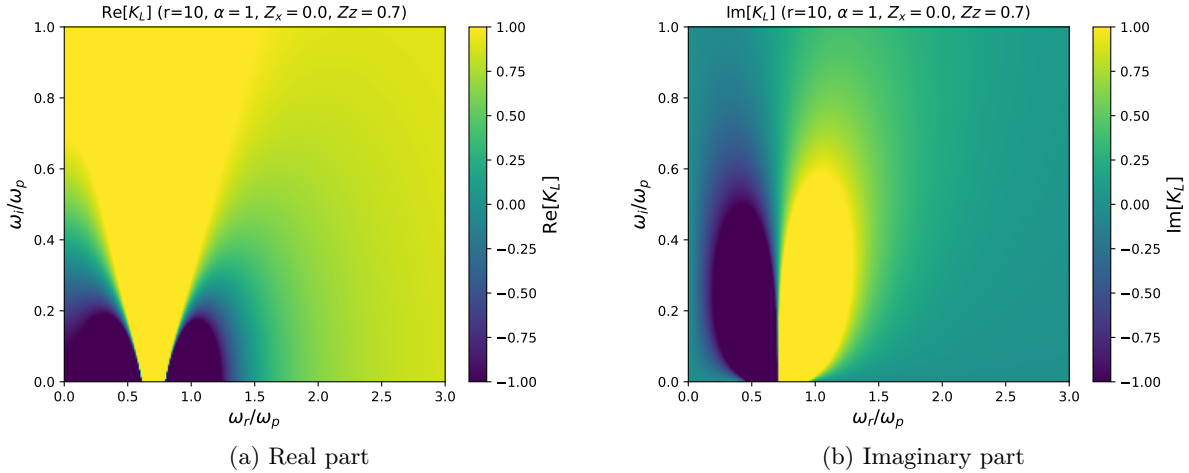


Figure 6: The longitudinal response tensor K_L for $Z = (0, 0, 0.7)$ as a function of complex ω . On the left, we have the real part, and on the right, we have the imaginary part. All values > 1 are displayed as 1, the same for -1 so the zeros are more visible.

so, for the longitudinal part, one ends up with the two equations $\text{Re}[K_L] = 0$ and $\text{Im}[K_L] = 0$. Numerically, this is done with the plasmapy package for a general $\omega = \omega_r + i\omega_i$ and different values of the wavevector $\vec{k} = (k_x, 0, k_z)$ without loss of generality. The dispersion relation is, therefore, written in dimensionless form under the assumption of just one species:

$$0 = 1 + \frac{r^2}{Z^2} \left(1 - \frac{1}{2} \left[\Phi\left(r \frac{x + Z_z}{\sqrt{2}Z}\right) + \Phi\left(r \frac{x - Z_z}{\sqrt{2}Z}\right) \right] \right), \quad (70)$$

where $r = \frac{v_0}{V}$ is the velocity ratio. In practice, a point in the complex x -plane is marked if the value of both parts of K_L is below a threshold, and I checked by eye, that there is always a change of sign involved if a point is marked for both parts, so that there are no false discoveries. Take a look at Figure 6.

Here, the the real part of the longitudinal response tensor is plotted on the left and the imaginary on the right for some value of \vec{Z} as a function of ω_r and ω_i in units of ω_p . The real part only gets 0 for two parabola-shaped lines, where one of them crosses the y -axis at some level ω_i . The imaginary part is zero exactly along the maximum in the middle of those two parabolas, so there is no intersection where both of them are 0. But it additionally

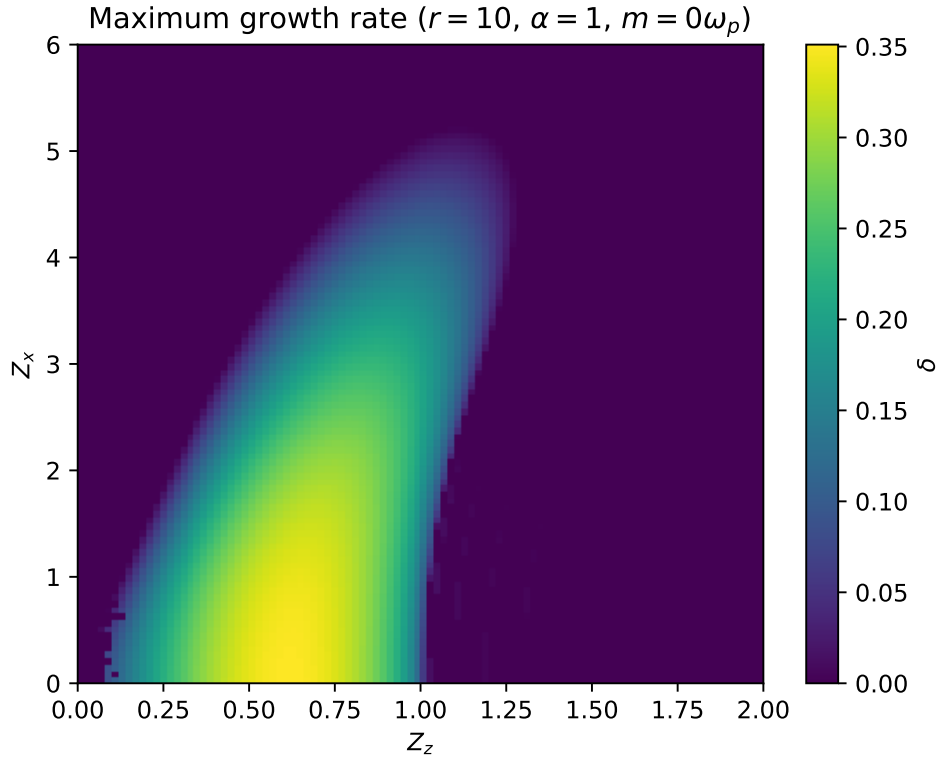


Figure 7: The maximum growth rate of a two stream scenario as a function of \vec{Z} with $\alpha = 1$ and $r = 10$. Compare this to Figure 1 of [26].

vanishes everywhere, where $\omega_r = 0$, so the point that always fulfils both $\text{Re}[K_L] = 0$ and $\text{Im}[K_L]$ and has $\omega_i \neq 0$ is the intersection of the parabola with the y -axis. This is the maximum growth rate.

In the automated process, all points that may arise where $K_L = 0$ are collected and the maximum ω_i of all those points is plotted in the (Z_x, Z_z) -plane in Figure 7. Some gaps occur where the spacing of the imaginary frequency grid was too low because the real part of K_L is rapidly growing with ω_i at $\omega_r = 0$ for some values of the wave vector. The largest growth rate is found at $\vec{Z} \approx (0.0, 0.61)$ and has a value of $\omega_i = 0.35\omega_p$. The reason why it is not at $Z_z \approx 1$ is to be found in the normalization of the frequency. The plasma frequency for the whole system was used instead of the plasma frequency of a single beam, which leads to an additional factor of $1/\sqrt{2}$.

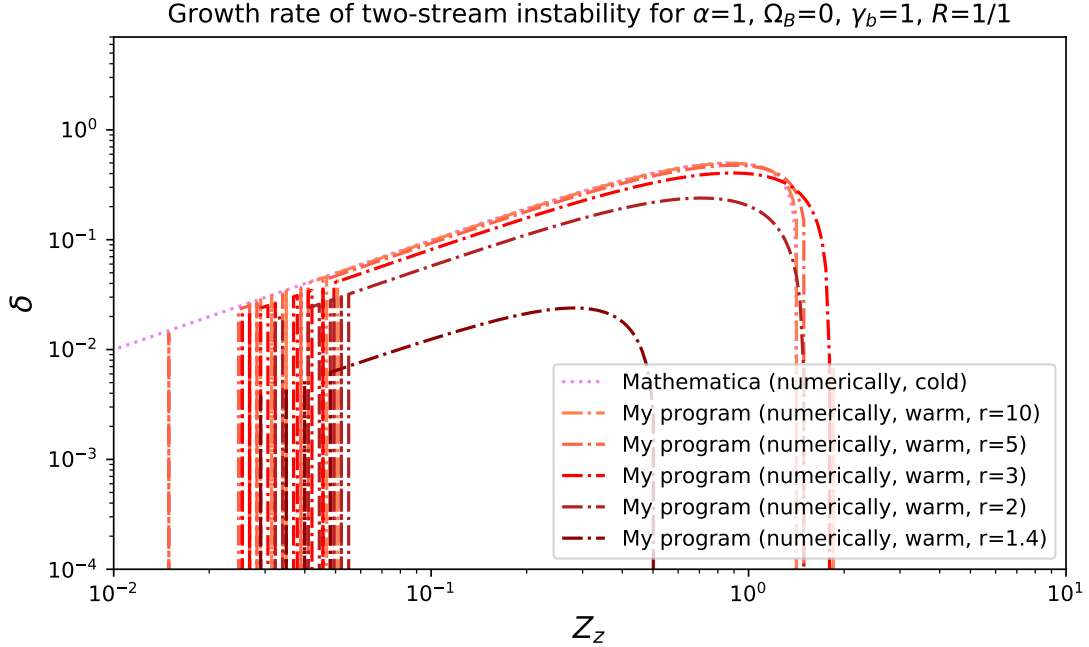


Figure 8: The maximum growth rate as a function of the normalized wave vector in Z -direction with $Z_x = 0$. The numerical solution of the cold two-stream dispersion relation is compared with several solutions of the warm two-stream dispersion relation for different values of r .

The whole procedure can be repeated for different values of the velocity ratio r . Small values of r are called the ‘warm’ case, while very high values of r are ‘cold’ because the velocity spread is basically negligible compared to the streaming velocity. The good question is, what values should be considered high and what values are low? Let us compare the contour along $Z_x = 0$ with the solution from before for different values of r . This is shown in Figure 8.

Although there are a lot of gaps for small Z_z , one can clearly see that the contour for $r = 10$ matches the solution of the cold dispersion relation pretty well. Even $r = 5$ can still be considered a cold stream. With $r = 3$, the growth rate is significantly influenced by the stream temperature and decreases the warmer the stream is. This is more clearly visible in Figure 9. Here we can see exactly how the growth rate $\delta = \frac{\omega_i}{\omega_p}$ behaves as a function of the velocity ratio r . The green curve was obtained by fitting the Laurent

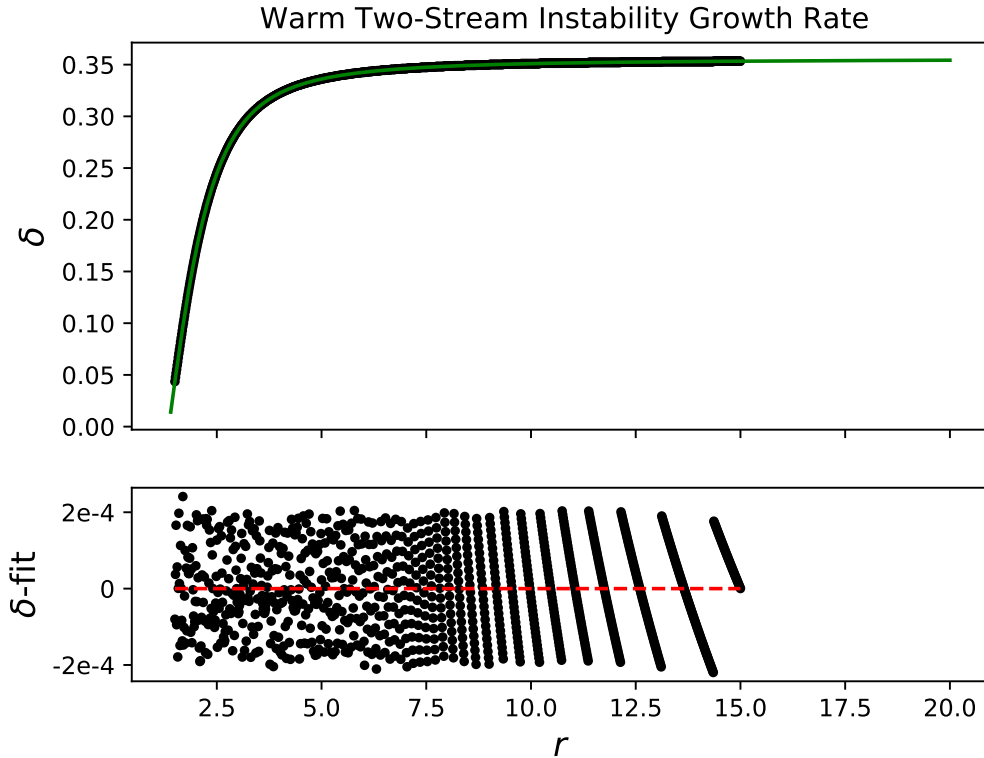


Figure 9: The maximum growth rate as a function of the velocity ratio. The black dots each represent a numerical solution to the two-stream dispersion relation. The green line is the fit of Function (71).

expansion

$$f(x) = \sum_{i=0}^9 \frac{a_i}{x^i}, \quad (71)$$

with parameters a_i to the data points that were obtained by taking the maximum of all growth rates for different \bar{Z} for several runs with varying r . For high values of r until about $r = 3$, the maximum growth rate does not change significantly. Only then does it start to decrease very quickly. The instability dies down completely for $r \approx 1.35$ with $\delta = 0$. It is expected to vanish, because in the limit $r = 1$, the two streams will not be distinguishable from a single very warm stream. The velocity distribution will not have a

positive derivative at any point which is crucial for the instability. The exact value r , below which there is no instability can be calculated from the Penrose criterion [35]. This states that if there are growing modes, there also must be effectively stable modes - mathematically expressed through $G(0 + i0^+) \geq 0$ for an instability to exist, where

$$G\left(\frac{\omega}{k}\right) \equiv \int d^2v \frac{\vec{k} \cdot \partial_{\vec{v}} f(v)}{\vec{k} \cdot \vec{v} - \omega} = \frac{k^2}{\omega_p^2} \quad (72)$$

is the electrostatic dispersion relation of the system (with $|k| \gg |\omega|$ and ω_p the plasma frequency of the full system). For the two-stream instability,

$$G(0 + i0^+) = \frac{\sqrt{2}r_p D\left(\frac{r_p}{\sqrt{2}}\right) - 1}{V^2}, \quad (73)$$

where $D(x)$ is the Dawson integral and $r_p = \frac{v_p}{r}$ the projected velocity ratio ($v_p = v_0 \cos(\arcsin \frac{Z_x}{Z})$). The function is plotted in Figure 10 and one can read off the root to follow that an instability can only exist for $r_p \gtrsim 1.3$.

In Figure 11, the full \vec{Z} -space is shown and how the instability decreases with higher values of r . It can be seen that the cold approximation is only working out for low values of r at $Z_x = 0$, but because the growth rate for $Z_x > 0$ never succeeds the growth rate at $Z_x = 0$, this is not a troubling realization. The reason for the reduced growth rate for highly oblique modes, as well as the slight smearing in the direction of higher Z_z for higher Z_x can be understood from the Penrose criterion, as well. For each wave number, the projected velocity is the relevant streaming velocity, so we never expect perpendicular modes and also modes with $v_p < 1.3V$ are suppressed. This is visualized in Figure 12.

The wave number of maximum growth will be important later on. This is the mode that will dominate the system after it grew most quickly. It is shown as a function of r in Figure 13. It is visible that $Z_z = 0.61$ for $r = 10$. It decreases pretty quickly for warmer streams. This is because modes with larger wave numbers are active on smaller scales, which get washed out quicker by random particle fluctuation induced by the temperature. The slight decrease for higher r comes from the fact that the smearing to modes with smaller angles between \vec{v}_0 and \vec{Z} decreases for growing r close to $Z_x = 0$.

It is worth noting that the electromagnetic modes resulting from the second equation of Eq. 19 will not contribute. The equation reads $K_T = \frac{Z^2}{x^2 v_0^2}$ and while the right side is expressible by the velocity ratio, there is still a

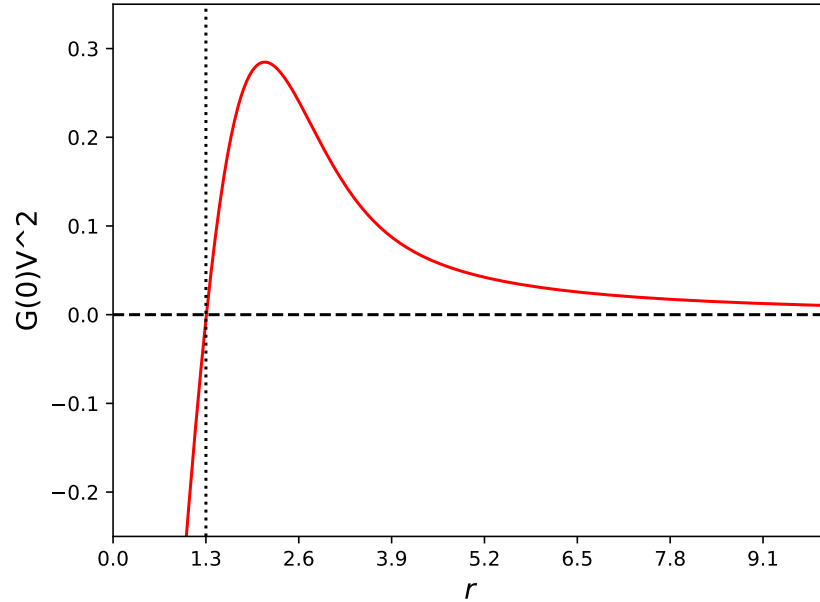


Figure 10: Visualization of the Penrose criterion: The function $G(0 + i0^+)$ as a function of the velocity ratio r .

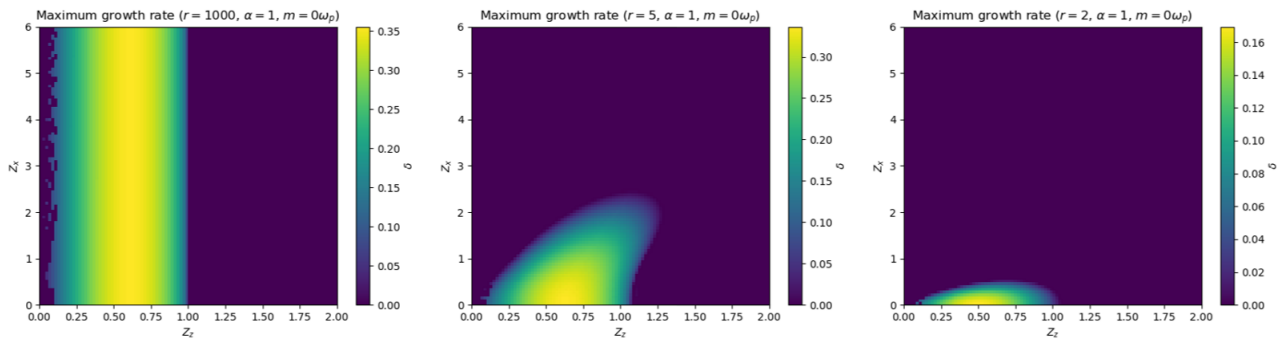


Figure 11: The growth rate as a function of \vec{Z} and the velocity ratio.

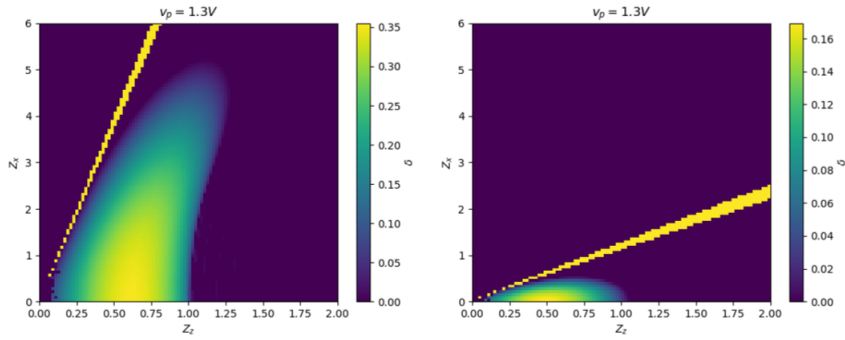


Figure 12: The maximum growth rate as a function of \vec{Z} for $r = 10$ and $r = 2$. The straight lines are where $r_p \approx 1.3$.

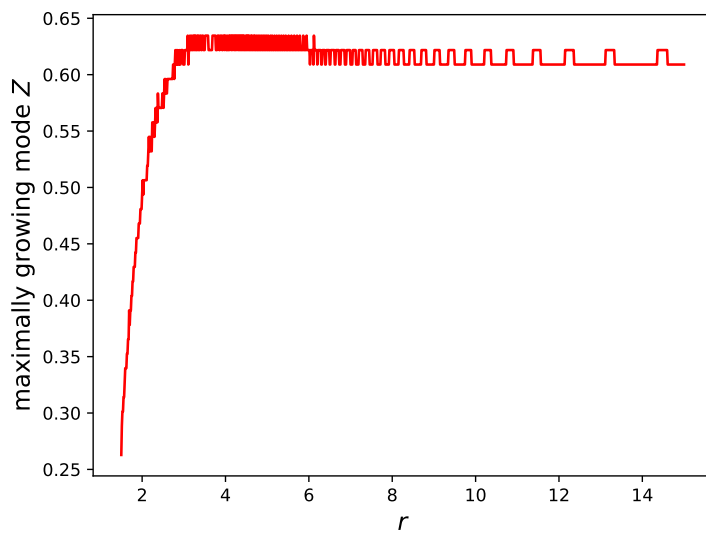


Figure 13: The value of Z_z of the maximum growth rate as a function of the velocity ratio.

dependence on the actual streaming velocity left. I found that there are no solutions to this equation for $v_0 \ll c$, though. The solutions for higher v_0 exist for very cold streams and are always smaller than the solutions for $K_L = 0$, as long as we stay away from the ultra-relativistic limit, where we should consider different equations. We are not interested in this regime due to the nature of dark matter.

3.3 Mediator Mass

Because we are not only considering the standard-model electromagnetic force, but a more general U(1)-type force, it is possible that there is a massive mediator involved. We need to make a little calculation to expand our model and to include a parameter m_A to describe the mass of this dark photon A . (I am basically following [26] in this section.) The generalized Maxwell equations are given by the Proca equation. Using the $(+,-,-,-)$ -convention, it reads in the Lorentz gauge $\partial_\mu A^\mu = 0$

$$(\partial_\mu \partial^\mu + m_A^2)A^\nu = j^\nu \quad (74)$$

for a mediator mass $m_A \neq 0$ with the 4-potential $A = (\phi, \vec{A})$ and a 4-current $j = (\rho, \vec{j})$. The Lorentz force will not change, because it directly follows from the potentials via the Lagrange equation. Therefore, all considerations that lead to Equation (27) still hold up. Also, the continuity equation remains valid. In Fourier space, the Proca equation is

$$(-\omega^2 + k^2 + m_A^2)A^\nu = j^\nu. \quad (75)$$

We can write

$$\vec{E} = -\vec{\nabla}\phi - \frac{\partial \vec{A}}{\partial t}, \quad (76)$$

and in Fourier space

$$\vec{E} = -i\vec{k}\phi + i\omega\vec{A}, \quad (77)$$

while the Lorentz gauge reads

$$\phi = \frac{\vec{k} \cdot \vec{A}}{\omega}. \quad (78)$$

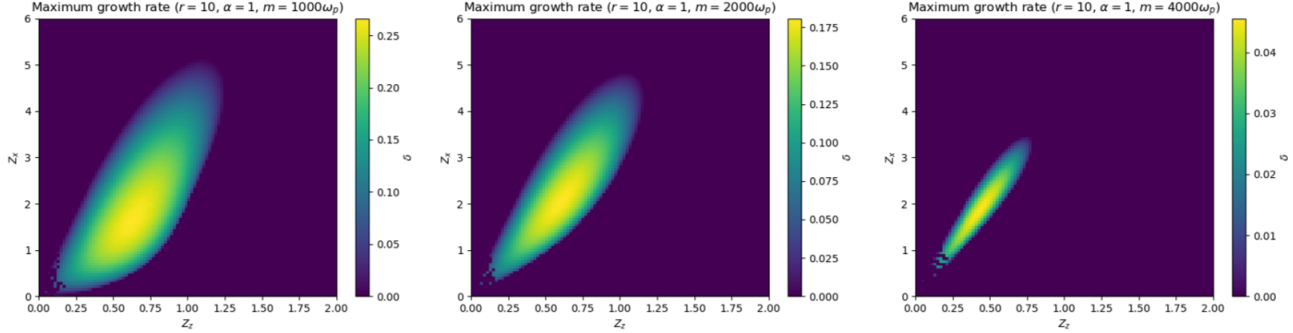


Figure 14: The growth rate as a function of \bar{Z} and the mass of the mediator m_A . The streaming velocity is $v_0 = 10^{-3}$ and, thus $V = 10^{-4}$.

Let us take a look at the spatial components and insert equations (77) and (78) into the Proca equation (75):

$$\begin{aligned} (\omega^2 - k^2 - m_A^2) A_i &= -j_i = -\sigma_{ij} E_j = -\sigma_{ij} \left(-\frac{i}{\omega} k_j k_n A_n + i\omega A_j \right) \\ \iff (\omega^2 - k^2 - m_A^2) \delta_{in} A_n &= \left(-\frac{i}{\omega} \sigma_{ij} \right) (\omega^2 \delta_{jn} - k_j k_n) A_n. \end{aligned} \quad (79)$$

If we isolate the longitudinal part of the tensor, we can compare it to Eq. (60) or Eq. (16) respectively, to see, what needs to be changed in our previous setup:

$$\frac{\omega^2 - k^2 - m_A^2}{\omega^2 - k^2} + \frac{i}{\omega} \sigma_L = 0, \quad (80)$$

where $\sigma_L = \frac{k_i k_j}{k^2} \sigma_{ij}$. It is obvious that I just need to replace the 1 in the dispersion relation $K_L = 0$ by $\frac{\omega^2 - k^2 - m_A^2}{\omega^2 - k^2}$ which returns the massless dispersion relation for $m_A = 0$. Because there is a single k instead of kV or kv_0 , the solutions now tend to depend on v_0 rather than on r alone.

You can see the behaviour of the growth rate as a function of m_A in Figure 14. The growth rate starts to decrease as soon as $m_A = \frac{\omega_p}{2v_0}$. It starts with the longitudinal modes, which vanish at $m_A = \frac{\omega_p}{v_0}$, so that the oblique modes start to dominate until they also vanish when m_A advances $\frac{\omega_p}{2V}$.

To understand this, let us expand the Penrose criterion by the mediator mass

[26]. The new dispersion relation reads

$$G\left(\frac{\omega}{k}\right) = \frac{k^2 + m_A^2}{\omega_p^2}, \quad (81)$$

so the new condition for instabilities to exist reads $G(0+i0^+) - \frac{m_A^2}{\omega_p^2} \geq 0$. From Figure 10 we can see that there cannot be any instability, whenever $\frac{m_A^2}{\omega^2} \gtrsim \frac{0.3}{V^2}$, which is the maximum of G . This explains the vanishing instability at $m_A = \frac{\omega_p}{2V}$. Even for a small mass, the region in r -space where an instability can exist is constrained. Just imagine the region that will be caged above the x-axis in Figure 10 when the function is shifted downward a bit. For large arguments x , the Dawson integral behaves like $D(x) \approx \frac{1}{2x} + \frac{1}{4x^3}$, so $G(0) \approx \frac{1}{r_p^2 V^2}$ and for an instability to exist $m_A \leq \frac{1}{v_p} \omega_p$. Thus, longitudinal modes completely vanish at $m_A \leq \frac{1}{v_0} \omega_p$, whereas oblique modes can survive longer because of their reduced projected velocity. But as long as $\frac{k}{\omega_p} = \frac{Z}{v_0} \gg \frac{m_A}{\omega_p}$, there is no huge difference between the massless and the massive mediator, as seen from the Proca equation (75). Moreover, as soon as a massive mediator is introduced, there will not be any cold two-stream instability. A velocity spread then becomes a necessary condition for growing modes. Intuitively, when the range of the interaction decreases because the mediator mass is heavier, then plasma phenomena begin to suffer.

3.4 Time Evolution

While the two-stream instability acts, directed kinetic energy is converted into electric energy of certain modes which dissipate it into thermal motion. This leads to heating of the plasma. If the streams start with some initial velocity ratio r_0 , over time, the ratio will be lowered due to the increasing thermal velocity until the instability is saturated. This happens at $r \approx 1.3$, as we analyzed earlier.

The energy W behaves according to [21]

$$\frac{dW}{dt} = 2\omega_i W, \quad (82)$$

which can be rewritten in my units easily because $W \sim V^2$:

$$\frac{dr}{d(\omega_p t)} = -\delta(r)r, \quad (83)$$

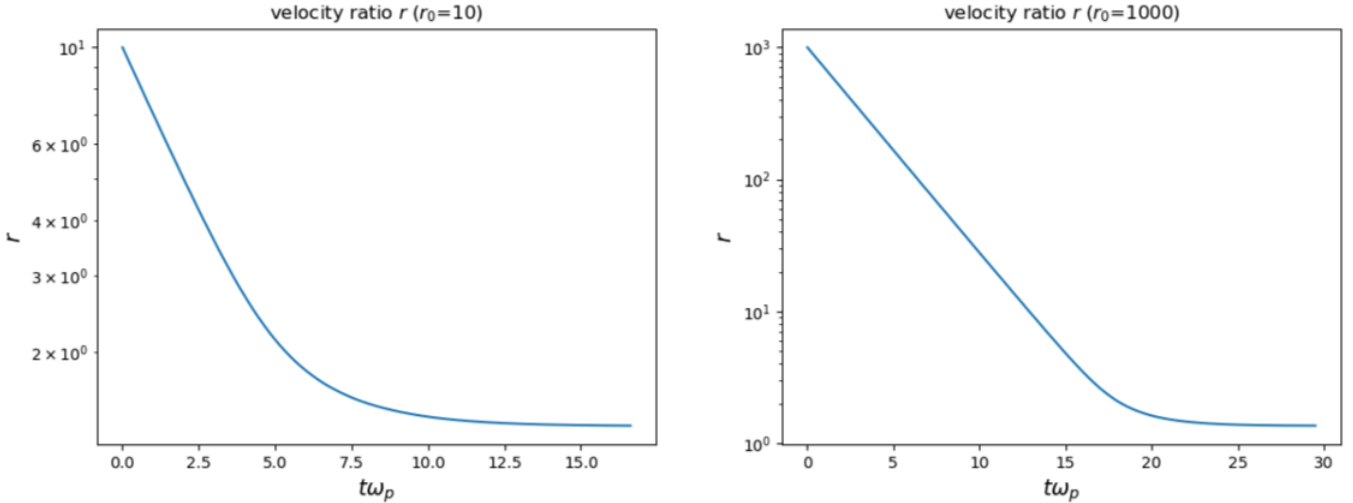


Figure 15: The velocity ratio of the streams as a function of time for two different initial velocity ratios r_0 .

where $\delta(r)$ is the growth rate as a function of the velocity ratio shown in Figure 9 and given by the results of the fit (71). With $\delta(r)$ known, the behaviour as a function of time of δ and r can be calculated numerically via the Euler method

$$r((n+1)\Delta t) = r(n\Delta t) - \delta(r(n\Delta t)) \cdot r(n\Delta t)\Delta t \quad (84)$$

for an integer $n \geq 0$, some time intervals Δt in units of plasma frequency and an initial value $r_0 \equiv r(0)$. Solutions for $r_0 = 10$ and $r_0 = 1000$ are shown in Figure 15 for $r(t)$ and Figure 16 for $\delta(t)$.

The velocity ratio decreases exponentially until it reaches $r \approx 1.35$ after which it becomes constant because the two-stream instability comes to a halt. It decreases like $\sqrt{2}^{-\omega_p t}$. When it reaches $r = 3$, the growth rate, which was constant at 0.35 before, starts to decrease exponentially itself with $e^{-0.5\omega_p t}$. The time after which the instability basically saturates and there is no significant growth expected anymore is when r gets constant. Although this time depends on r_0 it only does so very weakly and because for galaxy clusters like the Bullet Cluster $r_0 \approx \frac{10^{-3}}{10^{-4}} = 10$, we can record the growth time $t_{\text{growth}} = 10\omega_p^{-1}$ for the linear two-stream instability.

Let us take a moment to think about the possibly observable consequences

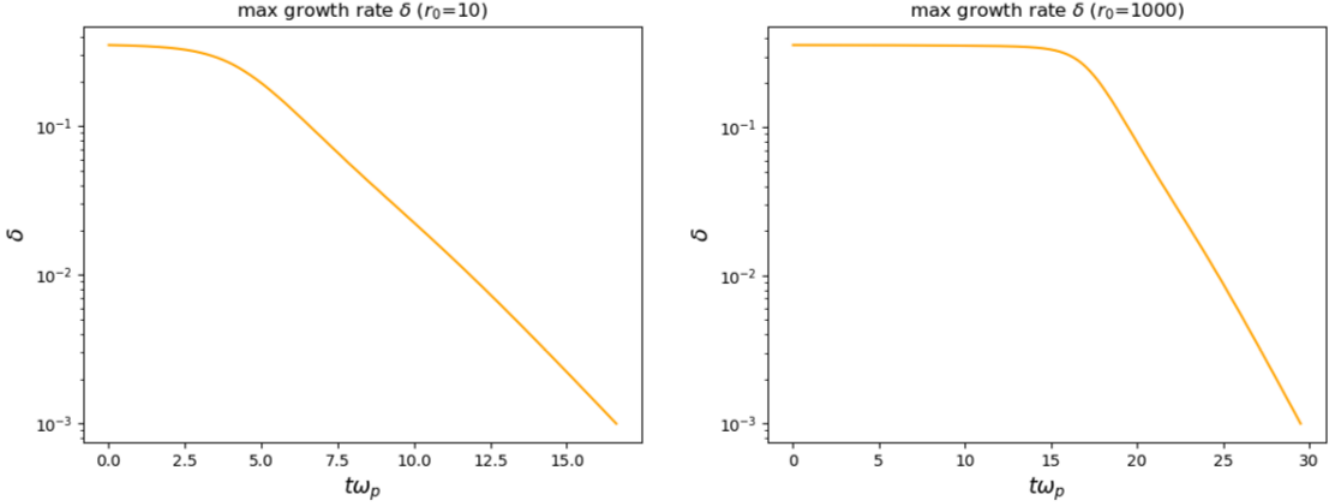


Figure 16: The maximum growth rate of the two-stream instability as a function of time for two different initial velocity ratios r_0 .

of this phenomenon. The dark matter temperature will be increased in a colliding cluster setup compared to an isolated cluster after the two-stream instability is saturated. But the streams of the two clusters are not infinite - there will only be a certain amount of time in which the instability can grow, namely the time, the two galaxy clusters need to pass through each other. We will call it the crossing time t_{cross} . It can be calculated for the Bullet Cluster as the model extension divided by the closing velocity, as done in Section 1.2 to obtain $t_{\text{cross}} = 9.4 \cdot 10^7$ yr. For the Bullet Cluster, we have a streaming velocity of $v_0 \approx 1300$ km/s and a velocity dispersion of $\sigma \approx 100$ km/s, so we can assume $r_0 \approx 10$. Therefore, it takes - as an order of magnitude - 10 inverse plasma frequencies for the instability to saturate. The plasma frequency depends on the dark matter properties and was given in equation (35) in Section 2.1.

By these means, we can constrain the parameter space, in which observations could be made: By setting $t_{\text{cross}} \gtrsim t_{\text{growth}}$ we gain

$$g \gtrsim 2.66 \cdot 10^{-18} \cdot \frac{t_{\text{growth}}\omega_p}{10} \frac{9.4 \cdot 10^7 \text{ yr}}{t_{\text{cross}}} \cdot \sqrt{\frac{0.1 \text{ GeV/cm}^3}{\rho_\chi}} \frac{m_\chi}{\text{GeV}}. \quad (85)$$

This is the relevant border for massless and low-mass mediators. In the case where the mediator mass is higher, it could be that no instability is

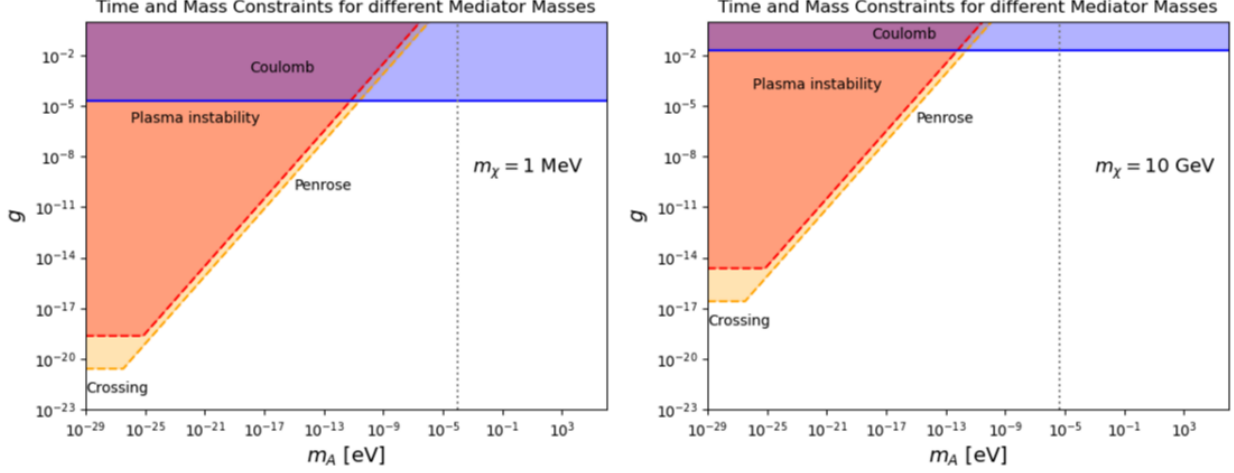


Figure 17: Bounds on dark matter plasma in g - m_A -space for two different values of m_χ . The yellow line shows the maximum of Eq. (85) and Eq. (86). The red contour shows the original results of Lasenby [26]. The upper blue area represents the region of the parameter space where $2 \rightarrow 2$ scatterings are important. Everything right of the grey dotted line is where the range of the interaction force is lower than the mean distance of the dark matter particles as described by Eq. (34).

forming at all. Remember from the Penrose criterion that $m \lesssim \frac{1}{2V}\omega_p$ for an instability to exist. Therefore, we can get the additional bound

$$g \gtrsim 2.64 \cdot 10^{-18} \cdot \frac{V}{100\text{km/s}} \cdot \sqrt{\frac{0.1\text{GeV/cm}^3}{\rho_\chi}} \frac{m_\chi}{\text{GeV}} \frac{m_A}{3.3 \cdot 10^{-27}\text{eV}}. \quad (86)$$

One can see that the bounds are equal for $m_{A,=} = 3.3 \cdot 10^{-27}$ eV. For $m_A < m_{A,=}$, the crossing time is the limiting quantity and for $m_A > m_{A,=}$ the Penrose criterion would inhibit the instability.

The two bounds are visualized in Figure 17 and Figure 18. The yellow line in Figure 17 consists of two parts. The first one is the horizontal line at the bottom, where Equation 85 is the harder exclusion. As long as the mediator mass is small enough, it is important that the instability needs a certain time to saturate. This is not dependent on the mediator mass, but it is dependent on the dark matter mass. As a result, the bounds for higher m_χ is weaker as seen in the comparison of the right plot of Figure 17 with the left. This shift is represented by the lowest line in Figure 18. For a massless mediator and

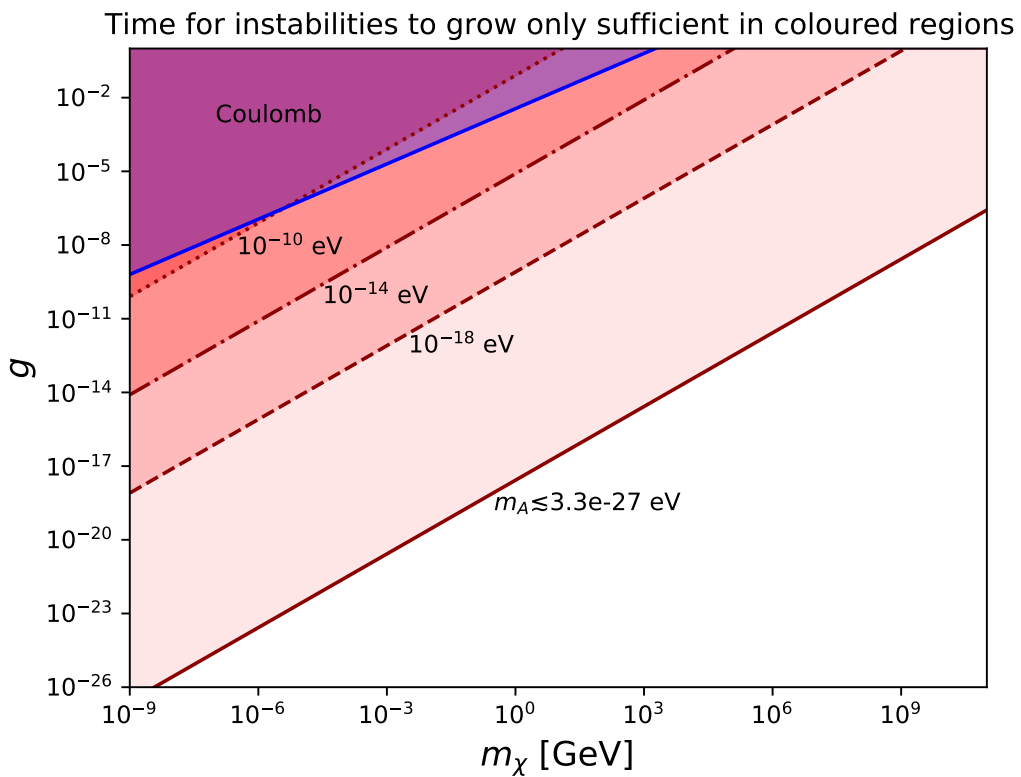


Figure 18: Bounds on dark matter plasma in g - m_χ -space for two different values of m_A . The lowest line shows Eq. (85) while all of the others refer to Eq. (86). The upper blue area represents the region of the parameter space where $2 \rightarrow 2$ scatterings are important.

for very light mediators, this huge region of the parameter space is excluded in the case of the missing observation of increased dark matter temperature. Even quite heavy dark matter U(1) candidates are excluded up to couplings of 10^{-8} . Because this is independent of the exact model, this is a very remarkable result. As I said before, Lasenby has already published similar exclusion bounds [26]. They are shown in red in Figure 17. In my work, I could strengthen his bounds that he gained by the same comparison of t_{cross} and t_{growth} , but while I looked at the linear time evolution of the instability, he did not consider any change in the velocity ratio, but instead claimed that a hundred e-folds of exponential growth with the maximum growth rate of 0.35 (compare Figure 7) would suffice. This is quite arbitrary. I have improved on this drawback so far.

For larger mediator masses, the bounds are weakened. In Figure 18 one can see the trend for growing mediator masses, until at about 10^{-10} eV all plasma effects will not be visible anymore because the $2 \rightarrow 2$ scattering starts to be the relevant mechanism of the clusters dynamics. More on that later. In Figure 17 this is visible in the rising curve where Equation (86) is dominant. The slight difference to Lasenby's results is here just induced by a slightly different choice of parameters. The grey dotted line in this plot marks the mediator mass that makes the range of the U(1)-force equal to the mean distance between particles in the galaxy cluster core. This means that everything left of this line cannot be modeled by my plasma description. We can see that the bounds from the Penrose criterion are more important, so that we can say nothing about this region of the parameter space either way. We also cannot exclude the blue region in the two figures with my plasma description because $2 \rightarrow 2$ -scattering is here the dominant source of cluster-dynamic changes. This region has to be included by conventional means. Because there is no evidence for frequent collisions of dark matter with itself, this region is very likely to be excluded, but this is very complicated to show. The relaxation time τ_C through Coulomb scattering is given by [36]

$$\tau_C = 3\pi^{3/2} \frac{m_\chi^3 V^3}{g^4 \rho_c h i \log \Lambda_C}, \quad (87)$$

where $\Lambda_C = 4\pi \frac{m_\chi V^2}{g^2 m_A}$ is a modified Coulomb logarithm for the Compton wavelength $1/m_A$ as the impact parameter. The bound comes from the fact that if this becomes of the order of the lifetime of galaxies - a few Gyrs - or lower, then we get a bound

$$g \gtrsim 3.6 \cdot 10^{-3} \left(\frac{m_\chi}{\text{GeV}} \right)^{3/4} \left(\frac{40}{\log \Lambda_C} \right)^{1/4}, \quad (88)$$

where Coloumb collisions dominate. Because the logarithm is only very weakly dependent on its parameters, we can assume it to be constant. This is the blue region of figures 17 and 18. In the following, I will even try to improve on these bounds by leaving the linear regime and take into account non-linear effects by simulating the two streams with the help of a PIC-code.

4 PIC-Simulations

4.1 Introduction to PIC-simulations

The idea of a particle-in-cell (PIC)-code is to discretize the base equations of mechanics and electrodynamics that describe the motion of charged particles in order to solve them numerically for a large number of particles N . I follow the approach of Fitzpatrick [37] and start in one dimension for simplicity and adopt periodic boundary conditions for the particles inside a box of length L . I imagine I have a bunch of mobile negatively charged particles in front of an immobile background of positively charged particles. I assume that their total charge is equal. The relevant equations are Newton's second law and the Poisson equation, written as two first-order differential equations:

$$\begin{aligned} \frac{dr_i}{dt} &= \tilde{v}_i \\ \frac{d\tilde{v}_i}{dt} &= a_i = -\frac{q}{m} \tilde{E}(r_i) \\ \frac{d\tilde{E}}{dr}(r) &= -\Phi(r) \\ \frac{d^2\Phi}{dr^2}(r) &= q(n(r) - n_0), \end{aligned} \tag{89}$$

where r_i is the position of particle i , \tilde{v}_i its velocity, a_i its acceleration, \tilde{E} the E-field and Φ the electric potential. The mean number density $n_0 = N/L$ equals the number density of positively charged particles. By applying the normalizations $\tilde{t} = t\omega_p$, $x = \frac{r}{\lambda_D}$, $v = \frac{\tilde{v}}{V}$, $E = \frac{1}{\sqrt{n_0 T}} \tilde{E}$ and $\phi = \frac{q}{T} \Phi$, where $V = \sqrt{T/m}$ is the initial thermal velocity, I arrive at the dimensionless equations

$$\begin{aligned} \frac{dx_i}{d\tilde{t}} &= v_i \\ \frac{dv_i}{d\tilde{t}} &= -E(x_i) \\ \frac{dE}{dx}(x) &= -\phi(x) \\ \frac{d^2\phi}{dx^2}(x) &= \frac{n(x)}{n_0} - 1. \end{aligned} \tag{90}$$

To solve these, I initialize a grid in space with J grid points $\tilde{x}_j = j\Delta x$ and spacing $\Delta x = L/J$. The boundary conditions demand that $\tilde{x}_0 = \tilde{x}_J$. The plasma density at each \tilde{x}_j - I call it n_j - is now generated by adding each

particle partially to the surrounding grid points proportional to its distance. To be clear, if particle i is at r_i which lies between \tilde{x}_j and \tilde{x}_{j+1} , then for the number of particles in dx , ndx :

$$\begin{aligned} n_j \Delta x &\rightarrow n_j \Delta x + \frac{\tilde{x}_{j+1} - r_i}{\Delta x} \\ n_{j+1} \Delta x &\rightarrow n_{j+1} \Delta x + \frac{r_i - \tilde{x}_j}{\Delta x}. \end{aligned} \quad (91)$$

After summing up all the particles, we have a discretized version of $n(x)$. By defining $\rho_j = \frac{n_j}{n_0} - 1$ and $\hat{\rho}_{j'}$ and $\hat{\phi}_{j'}$ as the Fourier transformed ρ_j and $\phi_j = \phi(\tilde{x}_j)$, we can solve the fourth equation of (90) in Fourier space. We need:

$$\hat{\rho}_{j'} = \frac{1}{J} \sum_{j=0}^{J-1} \rho_j e^{-ijj' \frac{2\pi}{J}} \quad (92)$$

for $j' = 0, \dots, J-1$ and

$$\begin{aligned} \hat{\phi}_{j'} &= -\frac{\hat{\rho}_{j'}}{j'^2 \left(\frac{2\pi}{L}\right)^2} \\ \hat{\phi}_{J-j'} &= \hat{\phi}_{j'}^* \end{aligned} \quad (93)$$

for $j' = 0, \dots, J/2$. We get all ϕ_j by transforming back

$$\phi_j = \sum_{j'=0}^{J-1} \hat{\phi}_{j'} e^{ijj' \frac{2\pi}{J}}. \quad (94)$$

The third equation of (90) yields the E-field at \tilde{x}_j E_j ,

$$E_j = \frac{\phi_{j-1} - \phi_{j+1}}{2\Delta x}, \quad (95)$$

and $E(x_i)$ by linear interpolation: If particle i is, again, located between \tilde{x}_j and \tilde{x}_{j+1} , then

$$E(x_i) = \frac{\tilde{x}_{j+1} - r_i}{\Delta x} E_j + \frac{r_i - \tilde{x}_j}{\Delta x} E_{j+1}. \quad (96)$$

The remaining equations of motion can now be solved by the Euler algorithm. When calculating up to a time t_{\max} in N_{steps} steps, then one time step is $\Delta t = t_{\max}/N_{\text{steps}}$. In the n -th step, I calculate

$$\begin{aligned} v_i(t_n) &= v_i(t_{n-1}) - E(x_i) \Delta t \\ x_i(t_n) &= x_i(t_{n-1}) + v_i(t_n) \Delta t. \end{aligned} \quad (97)$$

The whole process repeats N_{steps} times until t_{\max} is reached. By adopting different initial conditions for the x_i and v_i , in this setup, one can induce different kinds of waves and instabilities as any given plasma would. Through time, one can trace all the important quantities one is interested in, which I will introduce whenever we need them.

4.2 Electron Plasma Waves

The most simple setup to start with is a single stream of particles, which in its rest frame just has a streaming velocity of 0. I initialize with a uniform distribution in space first and set the particle temperature to 0. The dispersion relation for electron plasma waves with a Maxwellian velocity distribution is given in simple cases by the Bohm-Gross dispersion relation [38]

$$\omega^2 = \omega_p^2 + \gamma k^2 V^2, \quad (98)$$

where $\gamma = \frac{f+2}{f}$ is the adiabatic index of the plasma and f is the number of degrees of freedom. For our 1D-setup, $\gamma = 3$. This is valid for wavelengths $\lambda \gg \lambda_D$, so $k \ll 2\pi$ in my code.

With no temperature, we are in the case of electron plasma oscillations that Langmuir described in 1929 [24]. Therefore, the corresponding waves are also called Langmuir waves.

Figure 19 shows the phase space at different points in time. The oscillations arise due to fluctuations in the density arising from the random initialization of single particles. If I were to initialize the particles to be equally spaced, they would be in equilibrium and there would be no phenomena to be observed. However, one would expect a displacement δr (without normalization) to oscillate with the plasma frequency due to

$$\frac{d^2 \delta r}{dt^2} = \frac{e}{m} \tilde{E} = -\frac{e^2 n}{m} \delta r = -\omega_p^2 \delta r. \quad (99)$$

In normalized code units, the oscillation period is expected to be 2π because $T = \frac{2\pi}{\omega_p}$. This can indeed be observed as easily seen in the energy evolution

³An animated version of this plot can be found at <https://github.com/lc316353/DarkMatterPlasmaInstabilities> - the title of the corresponding animation-gif is given in each plot caption in typewriter font.

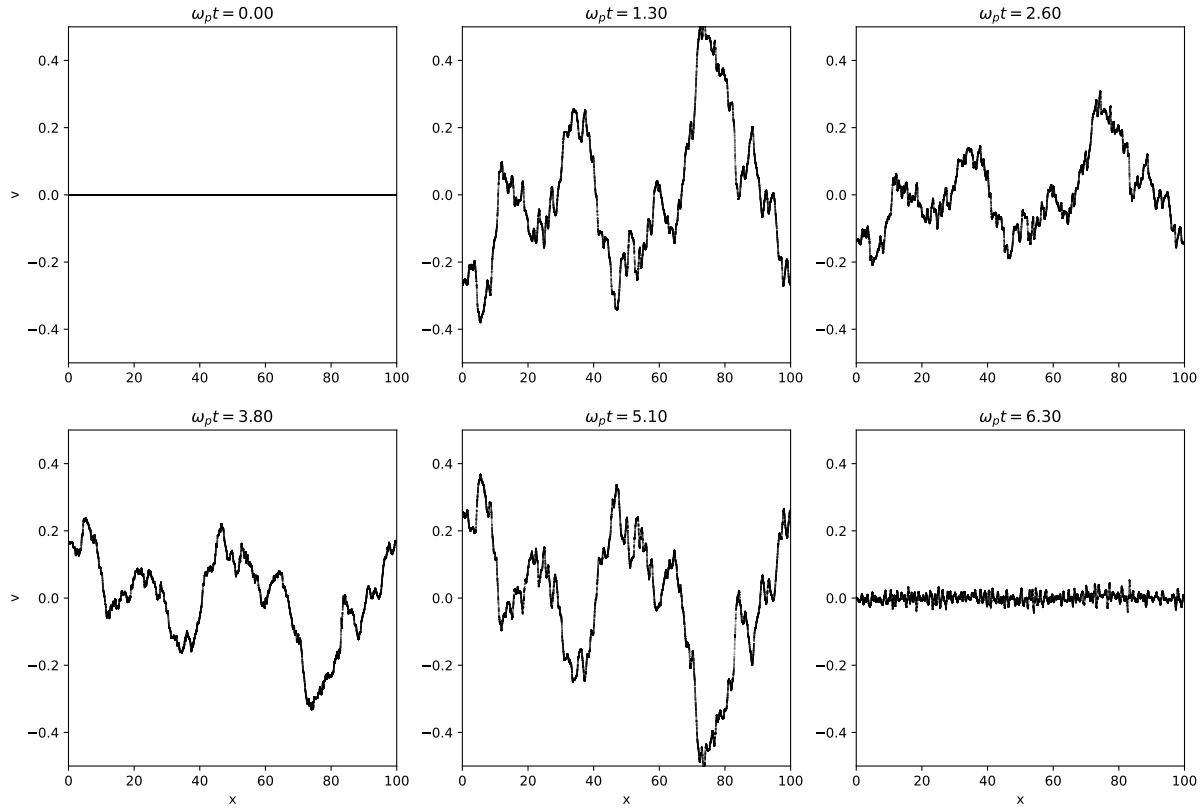


Figure 19: The phase space of the plasma particles as a function of time. Every black dot is a particle at position x and velocity v . The setup is chosen with $T = 0$ and a uniform distribution in space. The other parameters are $N = 2 \cdot 10^4$, $L = 100$, $J = 500$, $N_{\text{steps}} = 10t_{\max}$. ([electron-plasma-wave-zero-temp.gif](#))³

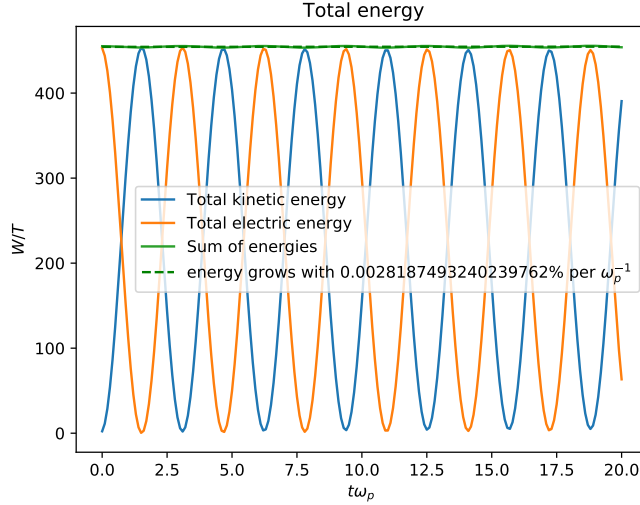


Figure 20: The kinetic energy (blue), the electric energy (orange) and the total energy (green), which is the sum of the first two, as a function of time for the same run as Figure 19.

shown in Figure 20. During the simulation, the energy is calculated from the velocity and the electric field at each time step like

$$W_{\text{kin}} = \frac{1}{2} \sum_{i=1}^N v_i^2 \quad W_{\text{el}} = \frac{1}{2} n_0 \Delta x \sum_{j=0}^{J-1} E_j^2. \quad (100)$$

This means that, in code units, the energy is normalized to the initial temperature $T = mV^2$. Of course, when $V = 0$ this is some arbitrary value instead, so that it is self-consistent without diverging. When calculating the total energy, due to the discretized nature of the PIC-code and the low order of the Euler method, instead of adding up the energies at the same time step, I calculate

$$W_{\text{ges}}(t_n) = W_{\text{el}}(t_n) + \frac{W_{\text{kin}}(t_n) + W_{\text{kin}}(t_n - 1)}{2}, \quad (101)$$

so that the total energy will not fluctuate as strongly when there is a quick rate of energy transfer. (Still, a small fluctuation is visible. But as long as the mean increase in energy is low, there is no need to worry about the quality of the simulation. In setups where I do not comment on the quality

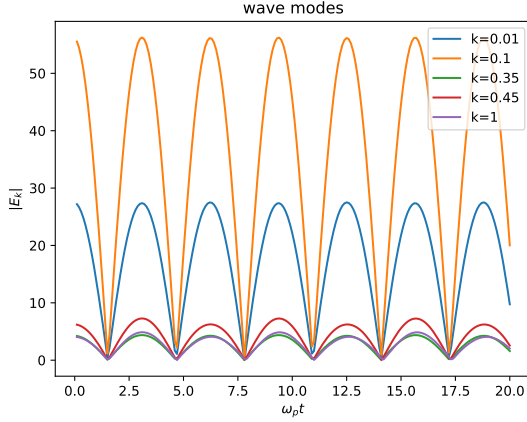


Figure 21: The Fast Fourier Transform of the electric field for some values of the wave number k . The amplitude decreases with $1/k$ but there are large fluctuations visible.

of energy conservation, I found this to be on the order of 10^{-4} per inverse plasma frequency.)

Now a more detailed view of what happens: All the particles are initialized with a velocity of 0, which is why they will all oscillate with the same phase. The kinetic energy will, thus, begin at 0. At most of the points, there will be a density gradient, resulting in a force that accelerates particles either to negative or to positive x , because everywhere where there is less density, there is a net positive local charge (from the ion background), and everywhere where there is more density, there is a net negative charge. This is the maximum displacement, and at this point, the electric energy is naturally at its maximum value. Depending on the amplitude of the density difference, the force is either stronger or weaker and leads to a different amplitude of the oscillation. Because the particles left their initial position, the force vanishes - at which point the electric energy vanishes -, but the particles overshoot due to their remaining velocity (W_{kin} is maximal) and the circle continues. So every particle in Figure 19 is actually performing a small ellipse that is very elongated in the v -direction, because $L = 100$ and $v_{\text{max}} \approx 0.5$.⁴

One can also take a look at the different wave modes of the oscillation by performing a fast Fourier transform (FFT) on the electric field at every time

⁴See `electron-plasma-wave-k0.045.gif` for a better visual

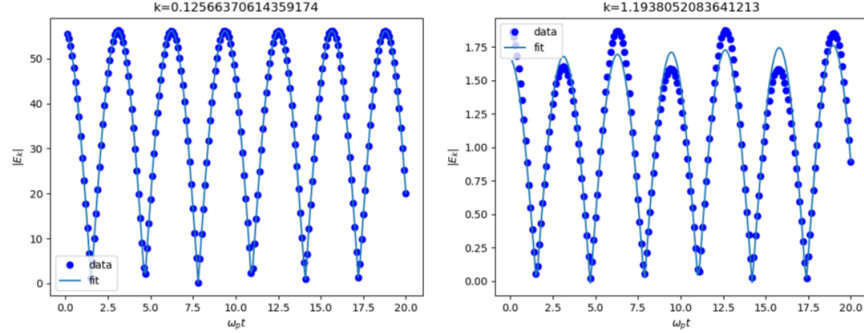


Figure 22: The fits of Function (102) to some mode with low k and some mode with high k .

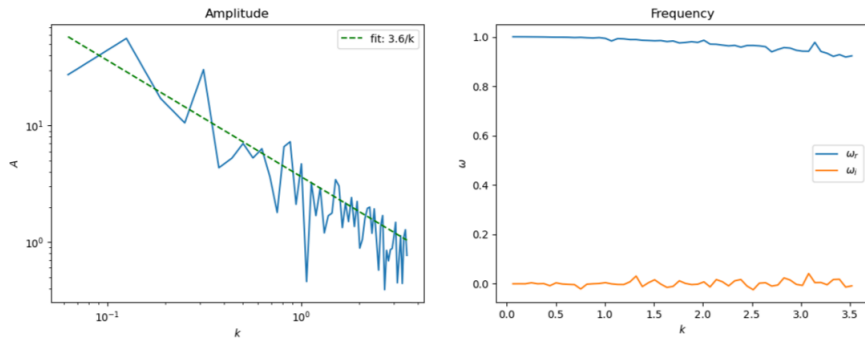


Figure 23: The fitted values A , ω_r and ω_i from Function (102) as a function of k . The dashed green line in the left plot marks $1/k$ to demonstrate the wavemode behaviour.

step. The absolute value of this Fourier transform for different wave modes k is in Figure 21. To be clear, the wave modes in the FFT are given as $k'_j = j' \frac{2\pi}{L}$ (meaning code units of λ_D) for $j' = 0 \dots J - 1$. Whenever I write $k = 0.1$, I am referring to the k'_j that is the first greater than k (e.g. for $L = 100$ k_2). Ideally, all of these curves are supposed to follow the function

$$A|\cos(\omega_r t + B)|e^{\omega_i t} + C, \quad (102)$$

where A, B, C are free parameters for a fit (the amplitude, the phase and some possible offset) and ω_r and ω_i are the real part and the imaginary part of the frequency. Two example fits are shown in Figure 22. For higher

values of k , the quality of the fit reduces because the spatial resolution is worse for small scales and because random fluctuations also happen on small scales and interfere with the modes from the plasma oscillations. If one fits all available modes until it is not meaningful anymore, one can plot some of the parameters as a function of wave mode, as shown in Figure 23. The amplitude of the wave modes follows a $1/k$ -profile. The reason for that is connected to the initialization of random fluctuations and will become clear in Section 4.4.1. The imaginary part of the frequency is always close to 0: there is no damping to be expected. The real part of the frequency is expected to be 1 for all wave modes (as $V = 0$) which can also be validated. If the spatial resolution is too low, though, it can be observed to decrease for higher values of k .

Adding a temperature that is non-negligible, leads to a propagation of the waves and to an increase of frequency for higher wave modes. For a better visual of this, I changed the way of inducing the plasma waves to have more control of the amplitude of certain wave modes. The positions will be drawn from a distribution following

$$f(x) = \frac{1 + a \cos(k_{\text{in}}x)}{L + \frac{a}{k_{\text{in}}} \sin(k_{\text{in}}L)}, \quad (103)$$

where a is a parameter controlling the strength of the wave-like density fluctuation, k_{in} is the initial wavenumber, and the denominator is for normalization to 1 when integrating over the length of the box. For now, I set $a = 0.2$ and look at the cases $k_{\text{in}} = 0.01$ and $k_{\text{in}} = 0.45$. Following [39], this is a procedure of validating a PIC-code:

The full truth for the warm non-relativistic dispersion relation is given by (see [39] appendix E or [22])

$$\frac{k^2 V^2}{\omega_p} + 1 = \sqrt{\frac{\pi}{2}} \frac{\omega}{kV} \left(\text{Erfi}\left(\frac{\omega}{\sqrt{2}kV}\right) - i \right) e^{-\frac{\omega^2}{2k^2V^2}} = \Phi\left(\frac{\omega}{\sqrt{2}kV}\right). \quad (104)$$

One can recover the Bohm-Gross relation for small values of k with Approximation (140) of Appendix A. Figure 24 depicts the expected function $\omega(k)$. The important lines are the black ones, which show the important branch of the expected numerical solution to the linear dispersion relation. This dispersion relation allows for an imaginary part of the frequency, which will be visible as a damping of the wave mode. For $k_{\text{in}} = 0.01$, one expects $\omega_r = 1.00015 \omega_p$ and $\omega_i = -4.7 \cdot 10^{-2167} \omega_p$, so still a practically negligible damping, and for $k_{\text{in}} = 0.45$ $\omega_r = 1.35025 \omega_p$ and $\omega_i = -0.10629 \omega_p$. Due to the initialization (103), there is more initial energy in the corresponding

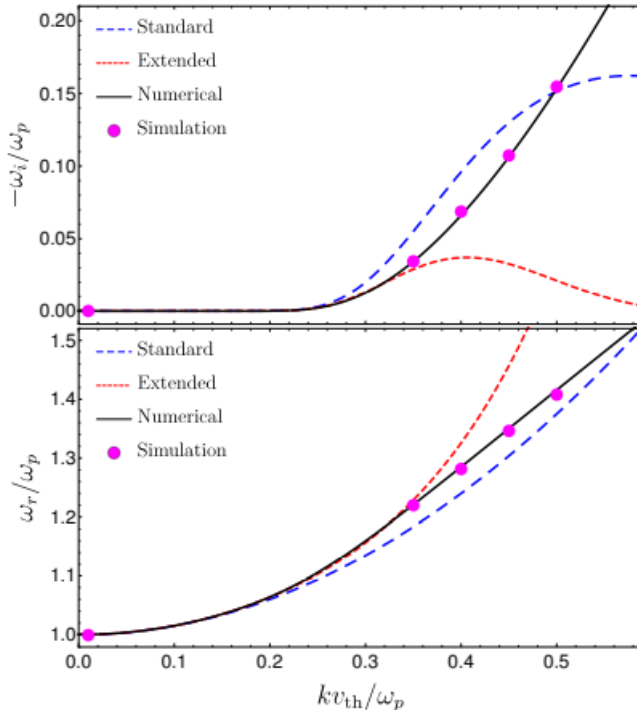


Figure 24: The warm, non-relativistic dispersion relation $\omega(k)$ for electron plasma waves. The black line is the full solution while the dashed and dotted line are different approximations (the blue dashed line in the lower plot corresponds to the Bohm-Gross-dispersion). The dots are the result of the PIC simulation from SHARP [39]. In the upper plot, the imaginary part of ω is shown, which corresponds to the strength of the damping of the wave, while in the lower part the actual oscillation frequency, the real part of ω is visible.

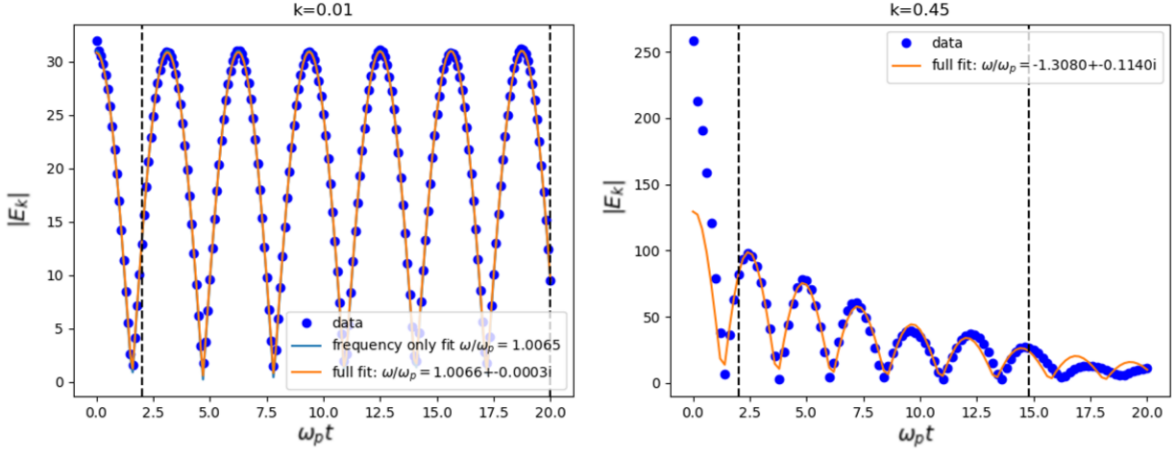


Figure 25: Fits to the wavemodes $k = 0.01$ and $k = 0.45$ when initialized with these modes. The temperature is non-zero. For the left plot $L = 100$, $J = 100$, $N = 2 \cdot 10^4$, $N_{\text{steps}} = 10t_{\max}$ (`electron-plasma-wave-k0.01.gif`) and for the right $L = 500$, $J = 1200$, $N = 2 \cdot 10^4$, $N_{\text{steps}} = 5t_{\max}$. (`electron-plasma-wave-k0.45.gif`)

mode, which starts leaking out in the damped case. Figure 25 shows the fit of Eq. (102) to the wavemodes $k = 0.01$ and $k = 0.45$ when initialized with each of these modes to measure ω_r and ω_i in my code. One can see, that my PIC code correctly reproduces the frequency and the damping rate of these modes. This validates my PIC-code and sets the way to set up the next stage of my work.

4.3 The Full Two-Stream Instability

As for the initial conditions, I adopted two opposing streams of thermal particles with a uniform distribution in space and a velocity distribution of

$$f(v) = \frac{1}{2\sqrt{2\pi}} \left(e^{-(v+r)^2/2} + e^{-(v-r)^2/2} \right), \quad (105)$$

with the streaming velocity in units of the initial thermal velocity $r = \frac{v_0}{V}$. A first example can be seen in Figure 26. It is initialized with $r = 10$ as can be seen from the v -positions of the stream and a box size of $L = 100$ which can be seen on the x -axis.

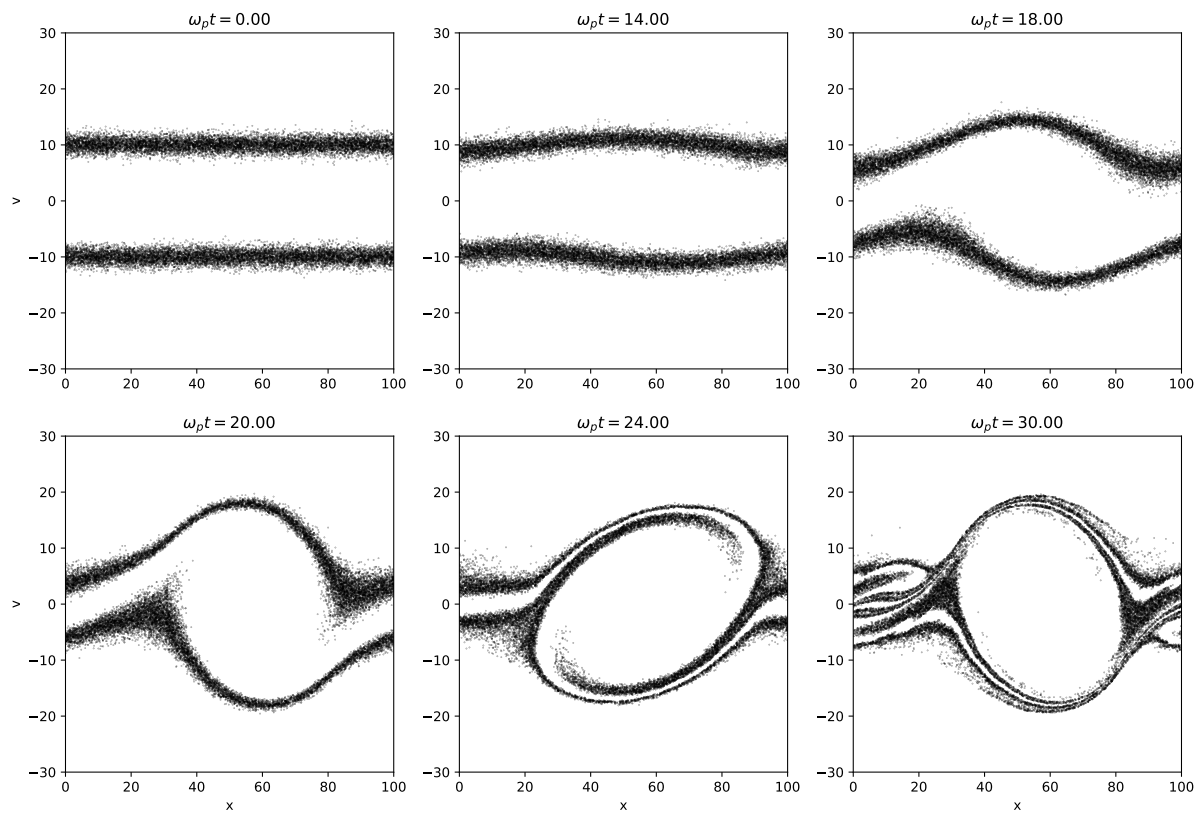


Figure 26: An example two-stream instability simulated by my PIC-code. The parameters are $r = 10$, $N = 2 \cdot 10^4$, $L = 100$, $J = 100$ and $N_{\text{steps}} = 10t_{\max}$. These will be the benchmark parameters for later reference. ([default-two-stream-instability.gif](#))

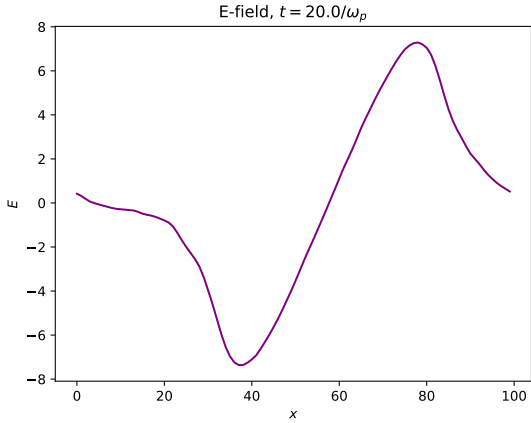


Figure 27: The electric field as a function of position corresponding to the upper left plot (at $\omega_p t = 20$) of Figure 26.

What happens is the following: Particles move around in their two streams and although there are background electron plasma waves in each stream, their energy is much smaller than the temperature. There are small fluctuations in the number density (as a consequence of the discrete particles), which lead to small fluctuations in the electric field. If, coincidentally, some electric field fluctuation grows beyond a certain threshold value, the two-stream instability kicks in and wavemodes start to grow exponentially.

In Figure 27, the electric field is shown after growth due to the two-stream instability. At this point, it stays constant (apart from slight overshoot oscillations). When it starts growing, at its maximum value, particles are accelerated in the right-going stream and decelerated in the left-going stream. At its minimum, vice versa. The particles will be drawn towards the minimum in the potential (the root of the electric field), where some of them will be trapped and start to oscillate. In phase space, this will look like a whirl. The slightly higher flow velocity at this special point will lead to a lower number density of particles and, thus, to an enhancement of the electric field. At the maximum and minimum of the electric field, particles are accumulating. Soon they are repelled by each other and stop the electric field from growing further. At this point, slight oscillations set in when particles are ejected from the over-density regions, increasing the number density in the whirl's middle, and, thus, reducing the acceleration of the following particles until the growth can repeat again. These overshoot oscillations are visible in the

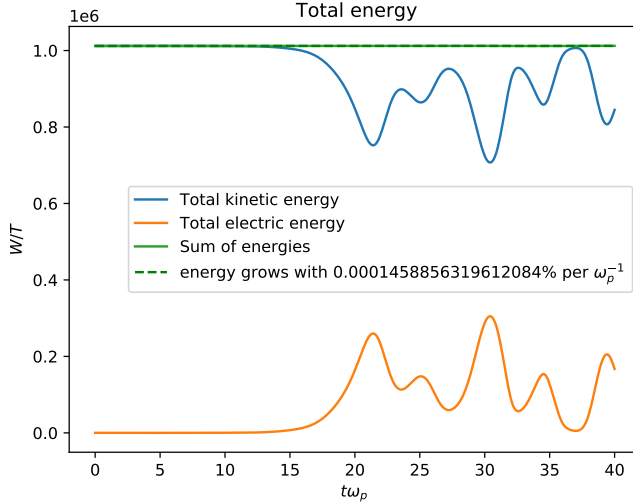


Figure 28: The energy plot corresponding to the run of Figure 26. Still, blue is kinetic, yellow is electric and green is the total energy.

‘tumbling’ of the egg-shaped whirl. While all of this happens, the velocity distribution gets washed out. What was once two streams with a clear Maxwell distribution of velocities is now a single symmetric distribution that may be (depending on the state of the overshoot oscillations) uniform in a certain range or has a varying number of peaks. In the long run, these oscillations get a bit smoother because the phase space is folded over and over like puff pastry, which hints at an increased temperature as well as a more uniform number density.⁵

Figure 28 shows the energy distribution during the run. In the beginning, the electric energy is almost 0 because the particles are uniformly distributed. Only the small fluctuations due to the discrete nature of particles give a small contribution that scales like (remember the definition (100))

$$W_{\text{el}} \approx \frac{1}{2} n_0 \frac{L}{J} J \langle E^2 \rangle \sim \frac{L}{2} \left(\frac{L}{2\pi} - \frac{1}{L} \right) \approx \frac{L^2}{4\pi} \quad (106)$$

because $\langle E^2 \rangle \sim \langle \left(1 - \frac{n}{n_0}\right)^2 \rangle = \frac{1}{n_0^2} (\langle n^2 \rangle - n_0^2) \sim \frac{L^2}{N^2} \frac{N}{2\pi} \left(1 - \frac{2\pi}{L^2}\right)$ from the equations of electrostatics and a calculation that will be revised in Section

⁵See `two-stream-long-run.gif`

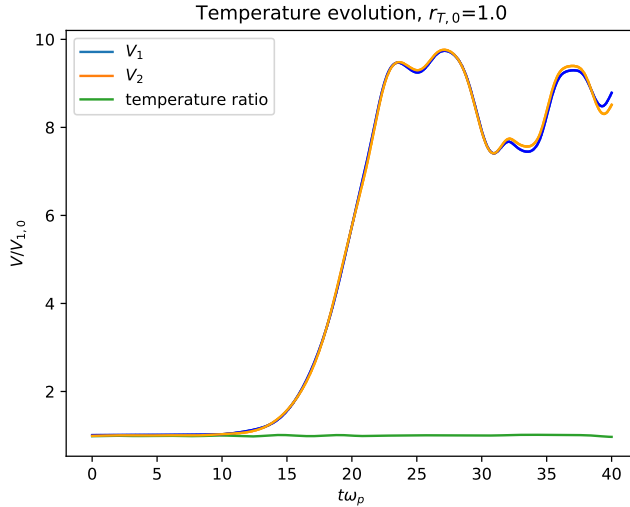


Figure 29: The temperature represented by the standard deviation of the velocity of each stream. The left-going one in blue (V_1), the right-going one in yellow (V_2) and the ratio of those two in green (V_1/V_2). Corresponds to Figure 26.

4.4.1. This is measured to be true up to a factor of $\frac{1}{2}$. The energy itself does not depend on N , but its fluctuation does. Most of the energy, though, is located in the streaming velocity. We expect the initial energy to be about

$$W_{\text{kin}} \approx \frac{1}{2}N\langle v^2 \rangle = \frac{1}{2}N(r^2 + 1) \quad (107)$$

(because velocities are normalized to the initial thermal velocity). Once the instability sets in, kinetic energy is transferred to electric energy until a maximum is reached. This maximum can give an orientation to when the instability saturates. At this point, the electric field is static as in Figure 27 and the velocity distribution is completely diluted. After this maximum, the energy starts to be periodically shifted back and forth between the electric and the kinetic component. These are the overshoot oscillations that will eventually decrease when the two-stream instability has more time to adapt.

The velocity distribution is more descriptive in Figure 29. In this setup, the two streams, of course, behave symmetrically. Once the two-stream instability sets in, the temperature starts to grow when the first particles are slowed down while others are accelerated. When it saturates, the energy

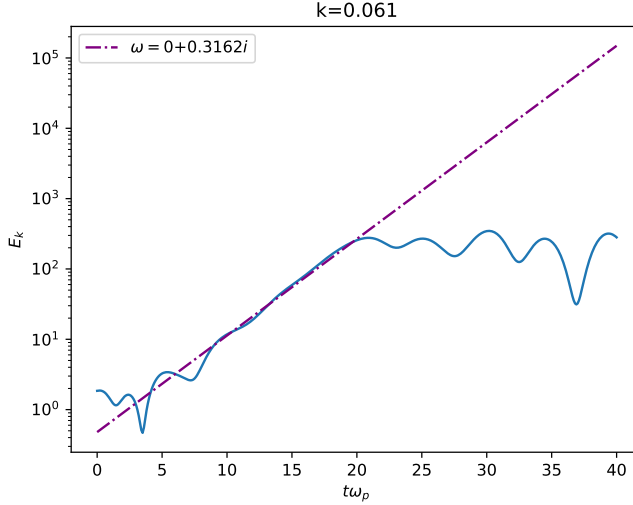


Figure 30: The wavemode of the maximum growth rate as expected from linear theory as a function of time. An exponential function is fitted to the part where it grows to measure the growth rate δ .

peaks for the first time and the velocity distribution is maximally diluted. This happens at $V \approx 8.5$ (averaging over overshoot oscillations). This means that the initial thermal velocity - to which every velocity is normalized - is now 8.5 times higher. For a initial velocity ratio of $r_0 = 10$, this corresponds to a velocity ratio of $r = \frac{1}{8.5}r_0 = 1.2$ which is, naturally, a consequence of the Penrose criterion and can be compared to the linear evolution in Figure 15.

Another comparison with the linear calculation can be made when taking a look at certain wave modes as described in the last section. The wavemode $k = 0.061$ in units of inverse Debye length corresponds to $Z_z = \frac{kv_0}{\omega_p} = k\lambda_D r = 0.61$, which is the normalized wave number of maximum growth rate. We can fit the function

$$f(\tilde{t}) = Ae^{\delta\tilde{t}} \quad (108)$$

to the region where the two stream instability is unfolding. We receive a value of $\delta \approx 0.32$. This is fairly close to the maximum growth rate $\delta = 0.35$ from the linear calculation for $r = 10$ (see Figure 7).

Let us explore some of the parameters and interesting insights of the two-stream PIC-simulation.

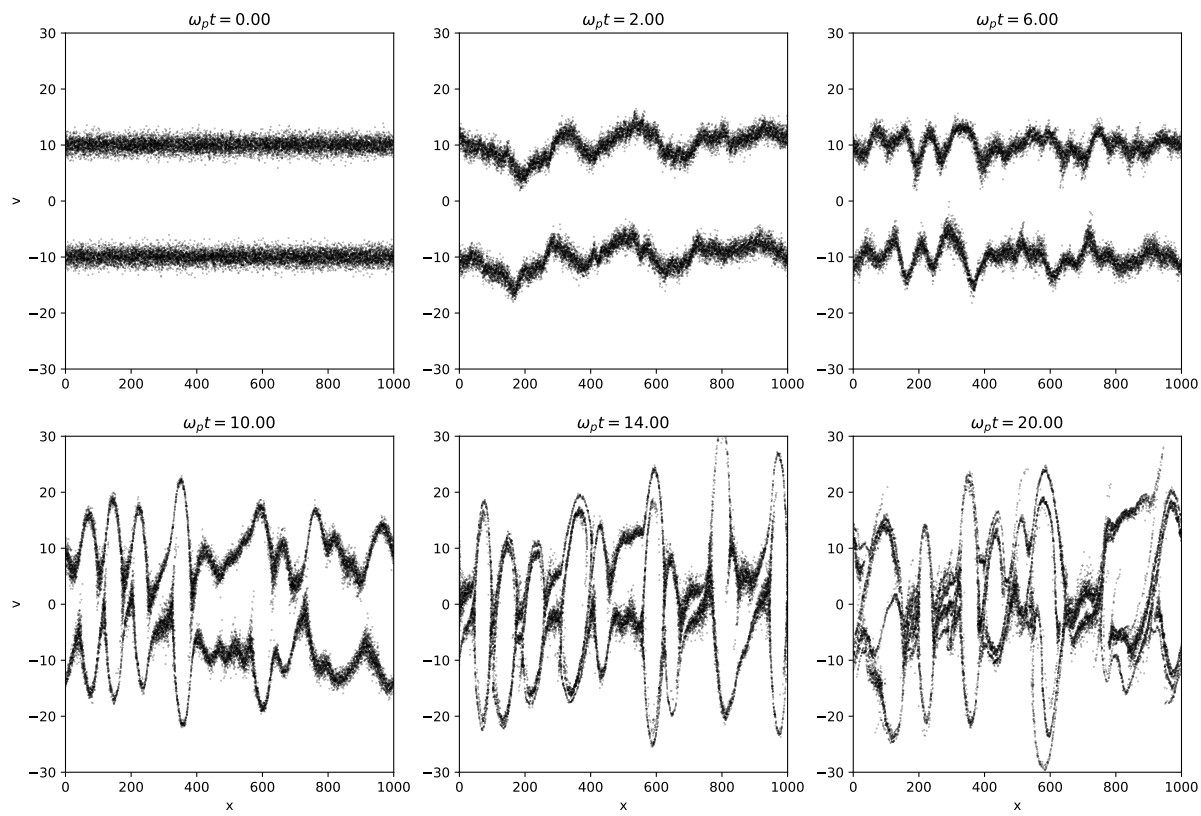


Figure 31: The phase space of a two-stream PIC-simulation with $r = 10$, $N = 2 \cdot 10^4$, $L = 1000$, $J = 1000$ and $N_{\text{steps}} = 10t_{\max}$. (`large-L-two-stream.gif`)

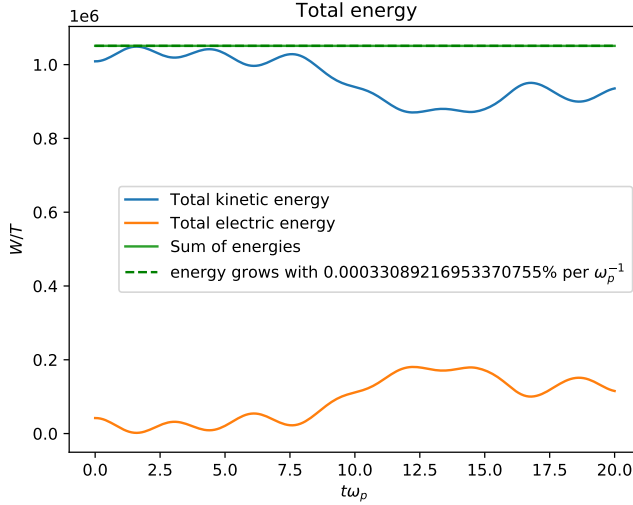


Figure 32: The energy plot corresponding to Figure 31.

In Figure 31, one can see basically the default setup from Figure 26, but with increased box size L and consequently increased grid spacing J to keep Δx constant. This time, there are several whirls visible. Additionally, one can see that electron plasma oscillations start to become relevant. This is better perceptible in Figure 32. Because of equation 106, the initial electric energy will be higher. Intuitively, if the particle number at one place is lower, because of the overall lowered mean number density, then fluctuations are not so strongly suppressed (compare to the Poisson error). These fluctuations can induce electron plasma oscillations. Additionally, the two-stream instability may kick in earlier. If L is raised with constant n_0 , then the initial electric energy still increases, but simultaneously, the kinetic energy increases by the same amount (see Equation (107)). Still, in phase space, slight oscillations can be observed in this setup.⁶ This is because the larger box size leaves room for smaller wave modes k and the amplitude of plasma oscillation modes goes with $1/k$ (compare Figure 23).

The length of the whirl in Figure 26 is about $100\lambda_D$ and for larger box sizes L , it can be seen that whirls have in average this extension (Figure 31). This can be understood from our linear setup: One can read off the maximum growth wavenumber from Figure 7 as $Z_{z,\max} = 0.61$ at $Z_x = 0$ (because of

⁶see `large-L-const-n0-two-stream.gif`

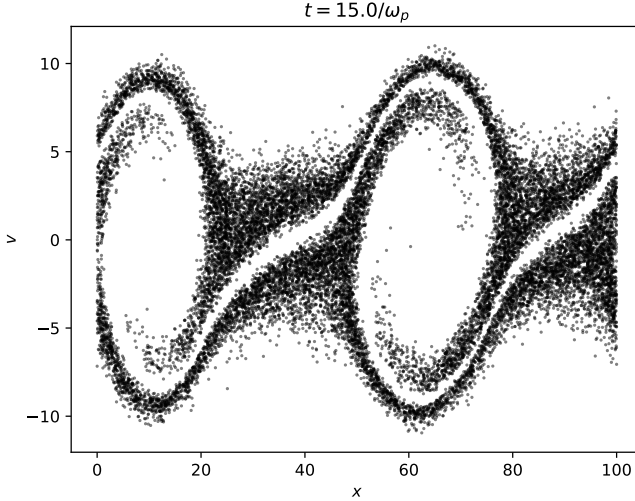


Figure 33: The phase space of a two stream instability for $r = 5$, $L = 100$, $J = 100$, $N_{\text{steps}} = 10t_{\max}$ and $N = 2 \cdot 10^4$. (two-stream-r5.gif)

the 1d-setup). The wavelength corresponding to that in Debye lengths is:

$$\frac{\lambda}{\lambda_D} = \frac{2\pi}{k_{\max} \frac{V}{\omega_p}} = \frac{2\pi v_0}{Z_{\max} V} = \frac{2\pi r}{Z_{\max}} \approx 100. \quad (109)$$

A whirl corresponds to a wavelength of the instability (compare with Figure 27) and, thus, it needs a space of about $100\lambda_D$. There is still a whirl fitting into the box for $L = 64\lambda_D$, which corresponds to a normalized wavenumber of $Z = 0.98$. If I measure the growth rate of the corresponding mode, I get a value of $0.174\omega_p$, which one can roughly confirm when looking at the corresponding value in Figure 7. Additionally, one can check the whirl size for different values of r and here, as well, one can affirm that it scales right. For example, Figure 33 shows the phase space for $r = 5$ and $L = 100$. The whirl size here should be half of the $r = 10$ case, and the two visible whirls confirm this.

As expected for $r \lesssim 1.5$ there is no instability emerging. For large values of r (e.g. $r = 1000$) we need to make sure that the box size is large enough so that at least one wavelength of the instability fits inside. The time it takes the instability to grow will naturally be higher due to the almost constant growth rate for $r > 3$ combined with the larger kinetic energy that can be dissipated. The maximum energy converted into electric energy will be

higher ($\sim 25\%$ instead of $\sim 10\%$).

If one modifies the initial velocity distribution to read

$$f(v) = \frac{1}{2\sqrt{2\pi}} \left(\alpha e^{-(v+r)^2/2} + (1-\alpha)e^{-r_T^2(v-r)^2/2} \right), \quad (110)$$

one can implement the density contrast $\alpha = \frac{n_1}{n_1+n_2}$ and the temperature ratio $r_T = \frac{V_1}{V_2}$, where 1 describes the left-going stream. Although I will not be further interested in these two parameters, I provide a short picture of how they are acting:

For a strong density contrast, the two-stream instability needs way more time to be induced and in the end, the less dense stream is completely dismantled.⁷ All particles are trapped in the potential minimum which moves in the direction of its original motion. The velocity distribution of the denser stream is almost constant, but non-thermal. Because the growth rate is reduced, the increase of energy looks damped.

Introducing a temperature ratio leads, over time, to an assimilation of this very same temperature contrast.⁸ When the two-stream instability saturates, both streams are heated up to the same temperature. The minimum of the potential is moving in the direction of the hotter stream. A movement must mean that the frequency of the maximum growth rate is no longer 0 so that there is a phase speed $v_{ph} = \frac{\omega}{k}$. Additionally, the growth rate is lower and it seems like density fluctuations are advantaged as the instability starts to grow very soon. In Figure 34, the temperature evolution of both streams and the ratio of them are depicted. They both increase up to ≈ 8.5 , which means that they just grow until the Penrose criterion stops them from heating any further. The ratio, thus, approaches 1.

The last important parameter I did not mention yet is the number of particles N . Besides its role of stabilizing the simulation similar to having a low Δx and Δt , which not only increases the accuracy of the results but also prevents leaks like the total energy increasing with time, N also leads to more statistical credibility. Furthermore, some of the quantities depend on N like the kinetic energy. The growth rate and the evolution of the two stream instability do not depend on the number of particles but nevertheless, N is an essential parameter when looking at the time difference between the instability's saturation and the start of the simulation. This is because the instability needs to be induced by electric field fluctuations that need to cross a certain threshold. But fluctuations are, of course suppressed by about $\frac{1}{\sqrt{N}}$.

⁷See `alpha-two-stream.gif` which has $\alpha = 0.1$

⁸See `rT-two-stream.gif` which has $r_T = 0.2$

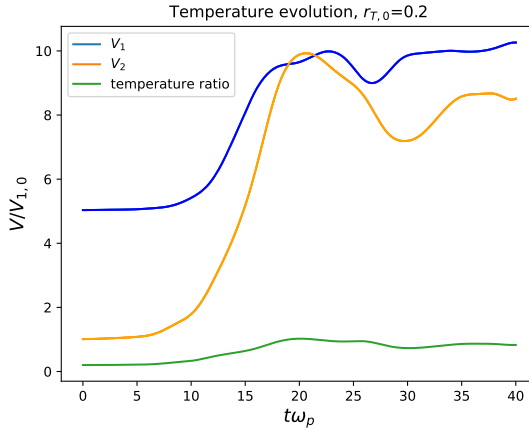


Figure 34: The temperature of the two streams in a setup that corresponds to the one of Figure 26 but with an additional temperature ratio of $r_T = 0.2$.

This is actually a relic of the increasing number density. For a constant box size $L = 100$, the time of the first maximum in the electric energy is measured as a function of N . An example can be in Figure 35 and the result is shown in Figure 36. The maximum energy was determined by the mean of several runs and the error on the maximum position was determined by eye. The χ^2 is quite small because I did a generous estimate for the errors. The power law fit seems to yield a good result that reads $\omega_p t_{\text{sat}} = 7N^{0.08}$. We can see that the actual growth time of the instability is still of the order of $\omega_p t_{\text{growth}} = 10$, but the wait for the initial fluctuation is not included in linear theory. This is, of course, a serious effect concerning Estimation (85) that may lead to a weakened exclusion bound for dark matter particles.

4.4 Noise

The initial condition of my PIC-code is of great importance for the development of the instability. As mentioned above, there is a dependence on the number of particles in the simulation regarding how long it takes for fluctuations to exceed a certain threshold and to kick off the two-stream instability. In my program I have, so far, always started off with a uniform distribution of particles, but in reality what we are looking at is the complex structure of a galaxy cluster, in which we do not necessarily have a uniform random distribution but a substructure where mass is accumulated at single galaxies.

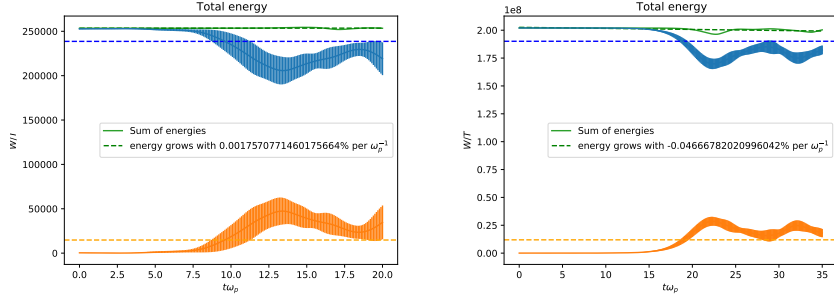


Figure 35: The plots show the energy of a PIC-simulation with the parameters of Figure 26 but with $N = 5 \cdot 10^3$ (left) and $N = 4 \cdot 10^6$ (right). The energy of each time step is averaged over several runs and the error bars depict the standard deviation divided by the square root of the number of runs.

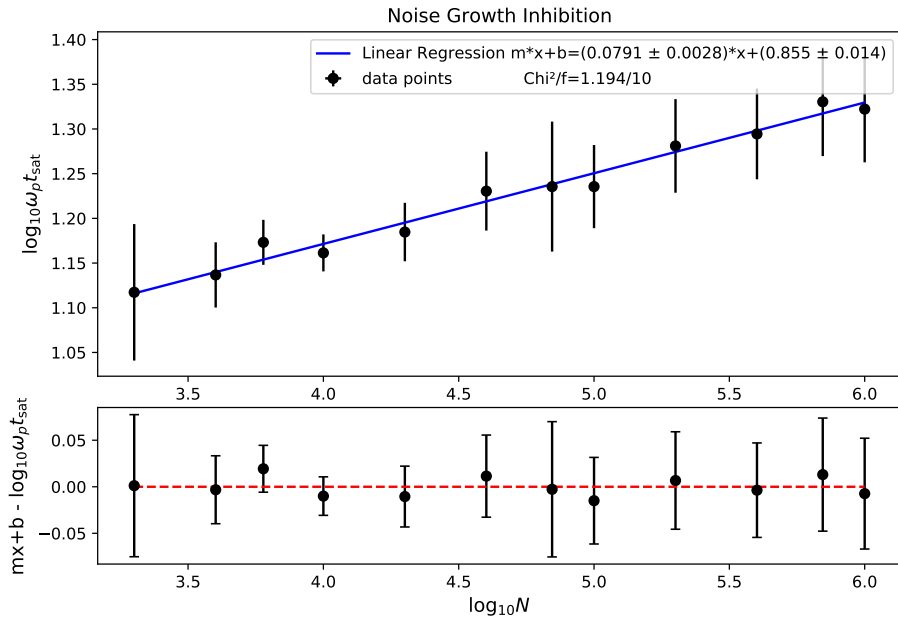


Figure 36: The saturation time t_{sat} of the two-stream instability from the simulation start to the electric energy maximum as a function of the particle number N for the parameters of Figure 26, especially $L = 100$. A linear regression was used to find the functional dependence $\omega_p t_{\text{sat}} = 7N^{0.08}$.

The size of such a galaxy is of the order of 10 kpc, which is not far from our estimate for the wavelength of the dominant mode

$$\lambda_{\text{TS}} = \frac{2\pi r}{Z_{z,\max}} \lambda_D = 39.8 \text{ kpc} \frac{r}{10 \text{ GeV}} \frac{m_\chi}{g} \frac{10^{-18}}{10^{-18}}, \quad (111)$$

with $Z_{z,\max} = 0.61$ where I have taken λ_D from Equation 31. This is the value along the current exclusion line. As this is of the order of galactic sizes, the amplitude of the number density for this mode will start with a certain value that may be higher than for random initialization. Let us take a closer look at this in the following sections.

4.4.1 Random Noise

Consider a number N of particles, that are drawn from a distribution $p(\vec{x})$, where \vec{x} is a general d -dimensional vector. Their number density is given by

$$n(\vec{x}) = \sum_{i=1}^N \delta(\vec{x} - \vec{x}_i) \quad \vec{x}_i \in p(\vec{x}). \quad (112)$$

If we Fourier-transform this, we arrive at

$$\begin{aligned} \tilde{n}(\vec{k}) &= \frac{1}{\sqrt{2\pi}^d} \int_{-\infty}^{\infty} d^d x e^{i\vec{k}\cdot\vec{x}} \sum_{i=0}^N \delta(\vec{x} - \vec{x}_i) \\ &= \frac{1}{\sqrt{2\pi}^d} \sum_{i=0}^N e^{i\vec{k}\cdot\vec{x}_i}. \end{aligned} \quad (113)$$

This Fourier-transform can be averaged over all the realisations of the \vec{x}_i and by using the central limit theorem $\langle \frac{1}{N} \sum_{i=0}^N f(\vec{x}_i) \rangle = \langle f(\vec{x}) \rangle$:

$$\begin{aligned} \langle \tilde{n}(\vec{k}) \rangle &= \frac{N}{\sqrt{2\pi}^d} \langle e^{i\vec{k}\cdot\vec{x}} \rangle \\ &= \frac{N}{\sqrt{2\pi}^d} \int_{-\infty}^{\infty} d^d x e^{i\vec{k}\cdot\vec{x}} p(\vec{x}) \\ &= N \tilde{p}(\vec{k}). \end{aligned} \quad (114)$$

The standard deviation can be calculated from the second moment

$$\begin{aligned}
\langle |\tilde{n}(\vec{k})|^2 \rangle &= \frac{1}{(2\pi)^d} \int d^N \vec{x}_k \left(\prod_{k=1}^N p(\vec{x}_k) \right) \sum_{i,j=1}^N e^{i\vec{k} \cdot \vec{x}_i - i\vec{k} \cdot \vec{x}_j} \\
&= \frac{1}{(2\pi)^d} \left(\sum_{i \neq j} \int d\vec{x}_i \int d\vec{x}_j p(\vec{x}_i)p(\vec{x}_j) e^{i\vec{k} \cdot \vec{x}_i - i\vec{k} \cdot \vec{x}_j} + \sum_i \int d\vec{x}_i p(\vec{x}_i) \right) \\
&= (N^2 - N) |\tilde{p}(\vec{k})|^2 + \frac{N}{(2\pi)^d},
\end{aligned} \tag{115}$$

so that

$$\sigma_{\tilde{n}}^2 = \langle |\tilde{n}(k)|^2 \rangle - \langle |\tilde{n}(k)| \rangle^2 = \frac{N}{(2\pi)^d} \left(1 - (2\pi)^d |\tilde{p}(k)|^2 \right). \tag{116}$$

One can directly see that while the mean value of a mode scales with N , the fluctuations $\frac{\sqrt{\langle |\tilde{n}|^2 \rangle}}{\langle \tilde{n} \rangle}$ scale with $\frac{1}{\sqrt{N}}$ as one would expect from the Poisson error.

The reason why we are interested in $\sigma_{\tilde{n}}$ instead of $\tilde{\sigma}_n$, defined as the Fourier transform of the fluctuations of n in real space, is the following: in my PIC-code the number density is randomly fluctuating in every time step. In the same way, its Fourier transform fluctuates. We are waiting for a certain wavemode near k_{\max} to fulfil $\tilde{n}(k_{\max}) \geq \text{threshold}$. The mean probability for this is described by $\langle |\tilde{n}(\vec{k})|^2 \rangle$.

For a uniform distribution between 0 and L in $d = 1$, as I use it in my PIC-code, one gets

$$\tilde{p}(k) = \frac{1}{\sqrt{2\pi}} \frac{1}{L} \int_0^L dx e^{ikx} = \frac{1}{\sqrt{2\pi}} \frac{1}{ikL} (e^{ikL} - 1). \tag{117}$$

This explains the $1/k$ behaviour of the amplitude of electron plasma waves in Figure 23. The initial mode k of the number density gained by the uniform distribution of particles in space has an amplitude $\propto \frac{1}{k}$. For the limit of $L \rightarrow \infty$ with $n_0 = \frac{N}{L}$ constant, the mean value is $n_0 \delta(x)$, the Fourier transformed of a constant distribution.

4.4.2 Noise of the Galaxy Substructure

A galaxy cluster will have a certain substructure that leads to an amplitude of the Fourier modes that we are interested in. As above, we will calculate the mean value of this mode. The number density of dark matter $n = \frac{\rho}{m}$ of a

galaxy cluster is given by a halo of dark matter and the halos of each galaxy of the galaxy substructure of the cluster. N-Body simulations show that a large number of gravitationally interacting particles will arrange corresponding to the NFW-profile [13]

$$\rho_{\text{NFW}}(r) = \frac{\rho_0}{\frac{r}{r_s} \left(1 + \frac{r}{r_s}\right)^2}, \quad (118)$$

where r_s is some scale radius and ρ_0 is the density at r_s . This is true for the galaxies inside the cluster, as well as for the dark matter inside the galaxies. Without the background halo of galactic cluster size, the summed dark matter densities of the galactic halos follow

$$n(\vec{r}) = \sum_{i=1}^{N_g} \rho_g(|\vec{r} - \vec{r}_i|), \quad (119)$$

where N_g is the number of galaxies inside the cluster, \vec{r} are 3d-positions measured from the center of the galaxy cluster and where we replace each galaxy with an average galaxy with the same scale radius r_g and a number density at the scale radius $\rho_{0,g}$. A Fourier transform leads to

$$\begin{aligned} \tilde{n}(\vec{k}) &= \frac{1}{\sqrt{2\pi}^3} \sum_i \int d\vec{r} \rho_g(|\vec{r} - \vec{r}_i|) e^{i\vec{k} \cdot \vec{r}} e^{i\vec{k} \cdot (\vec{r}_i - \vec{r}_i)} \\ &= \frac{1}{\sqrt{2\pi}^3} \sum_i e^{i\vec{k} \cdot \vec{r}_i} \int d\vec{r} \rho_g(\vec{r}) e^{i\vec{k} \cdot \vec{r}}, \end{aligned} \quad (120)$$

with $\vec{r} = \vec{r} - \vec{r}_i$. Averaging over the different realizations of the galaxy distribution inside the cluster yields

$$\langle \tilde{n}(\vec{k}) \rangle = \frac{N_g}{\sqrt{2\pi}^3} \int d\vec{r}_i \rho_c(\vec{r}_i) e^{i\vec{k} \cdot \vec{r}_i} \int d\vec{r} \rho_g(\vec{r}) e^{i\vec{k} \cdot \vec{r}} \equiv \frac{1}{\sqrt{2\pi}^3} \tilde{\rho}_c \tilde{\rho}_g, \quad (121)$$

where $N_g \rho_c(r) = \frac{dN}{dr}(r)$ is the distribution of galaxies inside the cluster, a NFW profile with a scale radius of the cluster of r_c and $\rho_{0,c}$ is given by the demand that the total integral over space needs to give the number of galaxies N_g inside a galaxy cluster. Because for both functions ρ_c and ρ_g , one assumes an NFW-profile, motivated by N-body simulations of massive (quasi)-particles, the mean Fourier transform is basically the product of two times the same Fourier transform of the NFW-profile with different parameters. The integrals calculate to

$$\tilde{\rho}_s(\vec{k}) = 2\pi \rho_{0,s} r_s^3 \int d\theta \int_0^{c_{\max,s} r_s} dr \frac{r e^{ikr \cos \theta}}{(r_s + r)^2} = 2\pi \rho_0 r_s^3 (f_s(k) - f_s(-k)), \quad (122)$$

where

$$f_s(k) \equiv \frac{e^{ikc_{\max,s}r_s}}{1 + c_{\max,s}} - 1 - e^{ikr_s}(ikr_s - 1)[\text{Ei}(ik(1 + c_{\max,s})r_s) - \text{Ei}(ikr_s)], \quad (123)$$

with the exponential integral $\text{Ei}(x)$. In the limit $c_{\max} \rightarrow \infty$ this function looks like

$$f_{\text{cinf}}(k) = -1 - e^{ikr_s}(ikr_s - 1)\left(i\frac{k}{|k|}\pi - \text{Ei}(ikr_s)\right). \quad (124)$$

The final mean number density in Fourier space, thus, reads

$$\langle \tilde{n}(k) \rangle = \sqrt{2\pi}N_g\rho_{0,g}\rho_{0,c}r_g^3r_c^3(f_g(k) - f_g(-k))(f_c(k) - f_c(-k)). \quad (125)$$

f_s satisfies $f_s(-k) = f_s^*(k)$, so $\langle \tilde{n} \rangle$ is a real function of k . The second moment reads

$$\langle |\tilde{n}(k)|^2 \rangle = \frac{1}{(2\pi)^3}|\tilde{\rho}_g|^2\left\langle \left| \sum_{i=1}^{N_g} e^{i\vec{k} \cdot \vec{r}_i} \right|^2 \right\rangle. \quad (126)$$

The last term was already calculated in Section 4.4.1 for a general probability function, so we can simply insert $\tilde{\rho}_c$ into equation 116, which yields

$$\langle |\tilde{n}(k)|^2 \rangle = \frac{1}{(2\pi)^3}|\tilde{\rho}_g|^2\left((N_g^2 - N_g)|\tilde{\rho}_c|^2 + N_g\right) \quad (127)$$

and

$$\sigma_n^2 = \frac{N_g}{(2\pi)^3}|\tilde{\rho}_g|^2\left(1 - |\tilde{\rho}_c|^2\right) = \quad (128)$$

$$\langle \tilde{n}(k) \rangle = \sqrt{2\pi}N_g\rho_{0,g}\rho_{0,c}r_g^3r_c^3(f_g(k) - f_g(-k))(f_c(k) - f_c(-k)). \quad (129)$$

To find the amplitude with which we should initialize the PIC-code, we need to insert the value of the wave mode that has the largest growth rate, namely $Z_{z,\max}$. We can use the values from Section 1.2 to calculate

$$r_s = \frac{R_{200,s}}{c_s} \quad (130)$$

and

$$\rho_{0,s} = \frac{M_{200,s}}{4\pi r_s^3} \left(\ln(1 + c_s) - \frac{c_s}{1 + c_s} \right)^{-1} \quad (131)$$

from the integral of a NFW-profile over space up to the cluster radius. The mass $M_{200,s}$ represents the value we want to receive from the integral, which is 1 for ρ_c and $\frac{M_{200,c}}{m_\chi}$ for ρ_g . So, we have $M_{200,g} = 10^{12} M_\odot$, $R_{200,g} = 200$ kpc, $c_g = 10$, $N_g \approx 1000$, $R_{200,c} = 2136$ kpc and $c_c = 1.94$. We do not need all of those quantities, when looking at

$$\frac{\langle |\tilde{n}(k)|^2 \rangle}{\langle |\tilde{n}(k)| \rangle^2} = N_g^2 + N_g \left(\frac{1}{|\rho_c(k)|^2} - 1 \right). \quad (132)$$

Let us estimate $|\rho_c(k)|$. The imaginary part of f_c is a quickly oscillating function of k for the relevant arguments. Its absolute value is always between 0 and about 1. Because it is oscillating strongly, there is always a value k very close to k_{TS} that can be excited maximally. Therefore, we can take $|\text{Im}[f_c(k)]| = 1$. We are left with

$$|\rho_c| = 2\rho_{0,c}r_c^3 = \frac{1}{4\pi} \left(\ln(1 + c_c) - \frac{c_c}{1 + c_c} \right)^{-1} \approx \frac{1}{\pi} \quad (133)$$

for $c_c \approx 2$, so

$$\frac{\langle |\tilde{n}(k)|^2 \rangle}{\langle |\tilde{n}(k)| \rangle^2} = N_g^2 + 5N_g \quad (134)$$

4.4.3 Translation into PIC-simulations

Let us return to the setup described at the end of Section 4.2. We will not initialize with a uniform distribution, but instead with

$$f(x) = \frac{1 + a \cos(k_{\text{in}}x)}{L + \frac{a}{k_{\text{in}}} \sin(k_{\text{in}}L)} \quad (135)$$

where we fix k_{in} at the mode $k_{\text{max}} = Z_{z,\text{max}}/r$. We want to scale a to find when the initial amplitude of this mode is enough to instantly trigger the two-stream instability. For different values of a and N for fixed L (and the parameters from Figure 26), we measure the quantity $\frac{\langle |\tilde{n}(k)|^2 \rangle}{\langle |\tilde{n}(k)| \rangle^2}$, which is done by taking the fast Fourier transform of the number density after it was calculated like in Equation (91). This is averaged over several runs and divided by the mean number density $n_0^2 = \frac{N^2}{L^2}$. The result is shown in Figure 37.

In the limit of small a , the initialization is equivalent to the uniform initialization. Therefore, it gets constant and behaves like $\frac{1}{N}$ (the square root

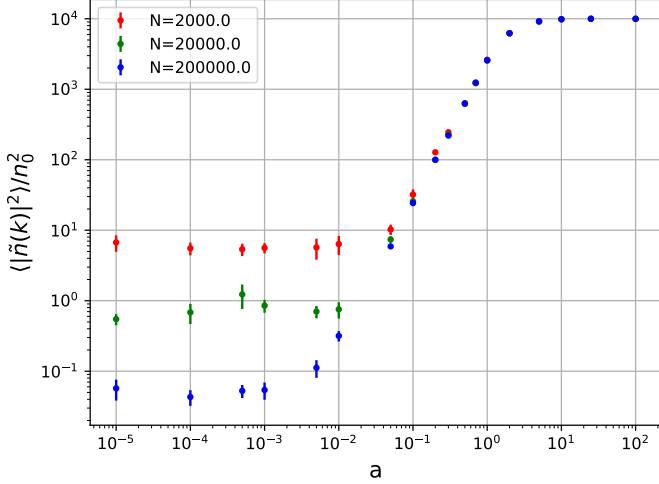


Figure 37: The relative fluctuations of the two-stream wavemode of the number density as a function of the parameter a and the number density N/L .

would of which would be the standard way to express this). In the limit of large a due to the normalization of Eq. (135), the a -Parameter cancels. At this point, all the available energy is stored in this wave mode and the function flattens out. The linear growth in between those two plateaus is the transition to shorter delay times because the initial fluctuations grow. At a point where the function is not distinguishable for two different N , the two-stream instability is instantly triggered by all modes with equal or greater N - the initial conditions need to be different if this is supposed to lead to different outcomes in terms of the saturation time.

With our calculation from the last chapter, we can estimate at which number density in the galaxy cluster the fluctuations are high enough to trigger the instability instantly, so that there is no delay and the exclusion bounds from Figure 18 stay unchanged. Because my PIC-code is not in 3d but in 1d, we can assume that under isotropy, the dimensions are multiplicative, simply meaning that we can take the cubic root of the calculated value to compare with the results of the PIC-simulation. So we expect the initial fluctuations to be $\frac{\langle |\tilde{n}(k)|^2 \rangle}{\langle |\tilde{n}(k)| \rangle^2} \approx (1000^2)^{1/3} = 10^2$ for a thousand galaxies in a galaxy cluster. We can, thus, take the number density for that the curves start to deviate at

$\frac{\langle |\hat{n}(k)|^2 \rangle}{|\langle \hat{n}(k) \rangle|^2} = 100$, which can be seen is $N = 2000$, which corresponds to $n = 20$. So, as long as $n\lambda_D > 20$, there is no delay before the two-stream instability is triggered.

4.5 Final Boundaries

For our dark matter model, we have

$$n_\chi \lambda_D^3 = 4.2 \cdot 10^{10} \sqrt{\frac{0.1 \text{ GeV/cm}^3}{\rho_\chi}} \left(\frac{V}{100 \text{ km/s}} \right)^2 \frac{1}{g^3} \left(\frac{m_\chi}{\text{GeV}} \right)^2 \quad (136)$$

from Eq. (31) and Eq. (34). For every part of the exclusion line that follows from the comparison of the growth time with the crossing time in Figure 18, it has to be checked if the condition $n\lambda_D > 20$ is fulfilled. Otherwise, instead of using t_{growth} , we need to use $t_{\text{sat}} = 4.8(n\lambda_D)^{0.08}$ from the Fit in Figure 36. Of course, this is not a relevant effect unless it changes by many orders of magnitude. Actually, one should introduce another lower boundary for the fit because the saturation time will not scale arbitrary low, because the growth time itself is a constant with about $t_{\text{growth}} = 10\omega_p^{-1}$. This again weakens the limits. But let us take a look at where this condition plays a significant role. The result is shown in Figure 38.

It is obvious that there is no need for revision of the exclusion bounds. Every relevant combination of mass and coupling would lead to such a number density in the dark matter halo of the cluster that the two-stream instability is instantly triggered, so that the growth time is the relevant time scale to compare with the crossing time. There were a lot of hand-wavy arguments and assumptions for parameters that the numbers could strongly depend on. This problem should, therefore, be revisited.

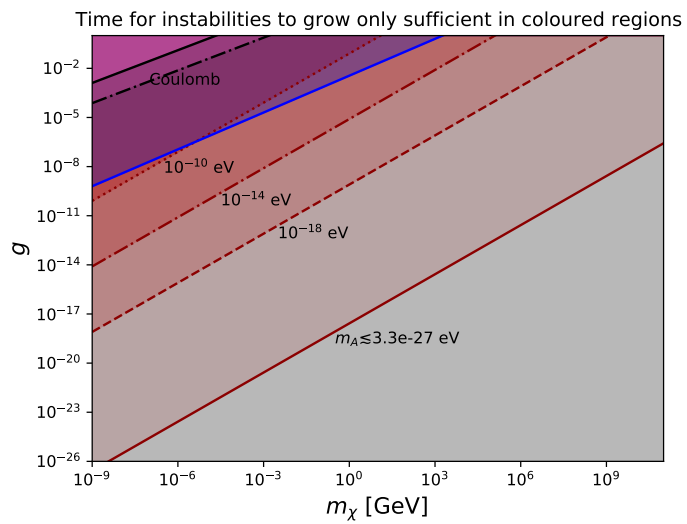


Figure 38: The exclusion bounds of Figure 18 with additional improvement check. The blackened straight line and the area beneath are where $n\lambda_D > 20$, so no revision is necessary. The dashdotted black line represents $n\lambda_D > 10^5$, for that the saturation time exceeds the growth time.

5 Conclusions and Outlook

In this thesis, I investigated a rarely considered feature of commonly assumed dark matter models: the long-ranged plasma-like interactions that lead to collective behaviour. In colliding galaxy clusters - the most famous one being the Bullet Cluster - this dark matter plasma would heat up, mainly due to the so-called two-stream instability. I calculated the setup in linear theory and had a closer look at the cold limit where some analytic understanding was possible. Then I calculated the growth rate of the two-stream instability as a function of the velocity ratio r between the streaming velocity and the thermal velocity. I explained the Penrose criterion and how it would be modified by a massive mediator, and I took a look at the time evolution of the instability that led to first exclusion bounds on all common U(1) dark matter models when compared to the crossing time of a galaxy cluster. Then, I went a step further and started to analyze the two-stream instability in a full numerical setup by writing my own PIC-code. I first understood the electron plasma oscillations that are a natural background effect, and then I had a thorough look at the two-stream instability. I discovered that there is a relevant delay before the two-stream instability starts to grow because of the need for fluctuations in the electric field. This led to the analysis of the initial noise inside a galaxy cluster. It turned out that, for typical galaxy clusters with an NFW-distribution of galaxies, the delay is immaterial. The main results of this paper are thus the well defended exclusion bounds of Figure 17 and Figure 18 that were already derived similarly by Lasenby [26]. There are several things to improve on and some open questions. The most important one is that we are yet to find a method of measurement that can detect the velocity distribution of dark matter directly instead of indirectly via the virial theorem, where it is assumed that the gravitational collapse is fully responsible for the velocity distribution of dark matter. Another option could be the dark matter density profile. If this can be measured accurately, then its deviation from the natural NFW-profile could be quantified. But given that there is no obvious derivation, one should check if the density profile is changed by the plasma interaction. If not, then the region in the boundary plot is excluded. The model can be improved in several ways, some of which are hinted at in Appendix B. So far, the two dark matter halos have been modelled as two infinite streams with constant density. The setup, certainly, is a bit more complicated with two finite streams that may have different densities and temperatures and, because of the density profile, even varying densities at different points of the stream. Still, the heating of

the galaxy clusters is inevitable if they consist of plasma-like dark matter. It just may take more or less time for the instability to saturate, so the bounds could shift.

Furthermore, one could add a dark proton mass instead of considering them immovable. If the instability is triggered, this may increase the growth rate if the mass ratio $R = \frac{m_e}{m_i}$ is large enough because of the Buneman instability (that merges with the two-stream instability in the $\alpha = 1$ -case) [27].

The PIC-code itself may be improved, as well. There are several more exact solvers for differential equations than the Euler method. Also, parts of this could run quicker in another programming language or with more parallelization.

$U(1)$ -models like milicharged dark matter and models where the dark photon is mixing with the standard-model photon may require additional analysis due to their interaction with visible matter. This was already performed by Lasenby and McQuinn et al. [26, 40]. The latter also considered non-zero magnetization (although I have some doubts about his arguments that the Weibel instability outweighs the two-stream instability in the unmagnetized case). A deeper analysis of the effects of magnetic fields could also be performed.

Last but not least, a very important point is a more careful investigation of the initial noise in galaxies. The transition from 3d to 1d should be studied cautiously because there are still problems like that for a large number of galaxies, the available energy of the mode can be exceeded. The initial noise of galaxy clusters is an interesting issue that may prove important in other topics of research.

In the end, I could confirm Lasenby's findings and improve his bounds on dark matter in terms of robustness and by an order of magnitude in the coupling.

Acknowledgements

There are several people I want to mention here: First of all, thank you, Philipp, for our long discussions at the whiteboard, for all your support, your helpful hints and questions and for sharing literature. Thank you, Hanno, for caring so much, for being a great role model as a PhD student. Thank you, Minh, for your supervising, Marco, for your brownies, and Andrea, for all the help during my Bachelor's thesis. Thanks Marie, Lena and Ivan for sharing the greatest office of all time with me. Greetings to everyone at the institute. I had a lot of fun during lunchtime talks, the journal club, the seminars, the barbecue and especially on the excursion to the labyrinth. Thanks to my supportive family members and roommates and everybody who wished me the best of luck in the last couple of weeks. Last year was a lot more than just writing this thesis, and I thank everybody who participated.

Appendix

A The plasma dispersion function

The plasma dispersion function always appears in dispersion relations when there is a thermal distribution of particles [21]. It is defined as

$$\Phi(z) = -\frac{z}{\sqrt{\pi}} \int_{-\infty}^{\infty} \frac{e^{-t^2}}{t-z} dt. \quad (137)$$

Some authors also call another function the plasma dispersion function, namely,

$$Z(z) = -\frac{1}{z} \Phi(z). \quad (138)$$

It can be expressed through the complex error function, as well (see [41]):

$$\Phi(z) = -i\sqrt{\pi}ze^{-z^2}(1 + \operatorname{erf}(iz)) = \sqrt{\pi}ze^{-z^2}(\operatorname{erfi}(z) - i). \quad (139)$$

Different limits of $\Phi(z)$ may be interesting: For $|z| \gg 1$

$$\Phi(z) = 1 + \frac{1}{2z^2} + \frac{3}{4z^4} + \dots - i\sqrt{\pi}\sigma ze^{-z^2}, \quad (140)$$

where $z = x + iy$ and

$$\sigma = \begin{cases} 0, & \text{if } y > |x| \\ 1, & \text{if } |y| < |x| \\ 2, & \text{if } y < -|x| \end{cases}. \quad (141)$$

For $|z| \ll 1$:

$$\Phi(z) = 2z^2 - \frac{4}{3}z^4 + \dots - i\sqrt{\pi}ze^{-z^2}. \quad (142)$$

What may be also interesting is the derivative that can be expressed through the function itself:

$$\frac{d\Phi}{dz}(z) = \frac{\Phi(z)}{z} + 2z(1 - \Phi(z)). \quad (143)$$

B More fun Setups

In this section, I introduce some models that I tried to build in order to solve some open questions, but ultimately, I had to dismiss them for various reasons. All the animations and my PIC-code can be found on <https://github.com/lc316353/DarkMatterPlasmaInstabilities>.

B.1 Reset

When two finite streams of plasma start crossing each other, then the front-most part will always react with fresh plasma that has not developed an instability yet. This is simulated by resetting one of the streams every timestep Δt_{reset} . This time can be estimated by the box size and the streaming velocity:

$$\Delta t_{\text{reset}} = \frac{L}{r}. \quad (144)$$

A smaller reset time will bring the setup closer to reality, but this is limited by the minimum box size that an instability needs to evolve (see Equation (109)). Of course, energy cannot be conserved in this setup. See `reset.gif` with the default parameters of Figure 26. It seems as if the reset stream is influenced quickly and the two-stream instability is not disturbed. However, if I arbitrarily use a lower number for Δt_{reset} , the growth time increases significantly because supportive fluctuations get washed out again and the stream needs a finite time to adapt to the instability.

B.2 Two Blops

The finite size of the two galaxy clusters may even better described by a setup where the initial number density is not uniformly distributed, but concentrated around a point $\mu_{1,2}$ for the two streams 1,2. It will either be a uniform distribution with exact expansion σ or a smoothed-out Gaussian distribution with variance σ . The first one will be called `two-boxes.gif` and the second one `two-blops.gif`.⁹ They use the default parameters of Figure 26 and $\mu_1 = \frac{1}{2}L$, $\mu_2 = \frac{3}{4}L$ and $\sigma = \frac{1}{25}L$. The background ions are simulated by the probability distribution function moving with r in the stream direction. The energy in this setup is not conserved as well, which is why it lacks credibility. But it can be observed that despite the interaction, the two clusters leave the interaction almost fully intact while the velocity distribution is obliterated. This means that the clearly distinct masses in the Bullet Cluster are themselves no evidence for non-existing plasma behaviour.

B.3 Sliced Cluster

Another approach to model the finite streams is to cut the cluster into several slices with length L and simulate each of them by an infinite stream in my

⁹Sadly, they are either broken or too big for Github right now. I will try to fix this

PIC simulation. Then the slices can be swapped with the slices of the other cluster one after another. To simplify the setup, only the temperature could be traced, but it turns out that you will lose important phase information. So what should be done is to save a snapshot of the phase space after each swapping time. For the first slice of one cluster, it is equivalent to the reset-scenario of Section B.1. The swapping time is equal to the reset time. But before each reset, the status of the reset-stream should be saved to use against a fresh, unperturbed plasma stream for the second slice of the cluster that interacts with all these saved stream statuses in the same order as before. After every slice of the first cluster interacted with every slice of the second cluster, the velocity distributions can be compared and averaged. With this setup, one can even simply introduce a density profile and an initial temperature ratio by making use of the velocity initialization in Equation (110). Nonetheless, the continuum limit is restricted by Equation (109).

C TRISTAN-MP

The TRISTAN-MP code is a publicly available PIC-simulation code¹⁰ that was optimized and runs on several cores.

C.1 Tips for the Setup

Due to a lack of time and space, I cannot go into the details. Further information can be found here: <https://ntoles.github.io/tristan-mp-pitp/Tristan-MP%20Features%20And%20Code%20Structure/Compilation/> Use a Linux system. Understanding the code units is tough. Here is what I think, I know:

$$\begin{aligned} \omega_p t_{\max} &= \text{last*c/c_omp} \\ N &= \text{ppc0*mx0*my0/2} \\ L/\lambda_D &= \text{mx0/c_omp/sqrt(delgam*temperature_ratio*mi/me)} . \\ r &= \text{gamma0/sqrt(delgam*temperature_ratio*mi/me)} \end{aligned} \quad (145)$$

I still do not know how to calculate the box length in units of λ_D , because this does not lead to the correct number of whirls.

¹⁰<https://github.com/ntoles/tristan-mp-pitp>

References

- [1] F. Zwicky. Die Rotverschiebung von extragalaktischen Nebeln. *Helvetica Physica Acta*, 6:110–127, January 1933.
- [2] J. H. Oort. The force exerted by the stellar system in the direction perpendicular to the galactic plane and some related problems. , 6:249, August 1932.
- [3] Vera C. Rubin and Jr. Ford, W. Kent. Rotation of the Andromeda Nebula from a Spectroscopic Survey of Emission Regions. *The Astrophysical Journal*, 159:379, February 1970.
- [4] Douglas Clowe, Maruša Bradač, Anthony H. Gonzalez, Maxim Markevitch, Scott W. Randall, Christine Jones, and Dennis Zaritsky. A Direct Empirical Proof of the Existence of Dark Matter. *Astrophysical Journal, Letter*, 648(2):L109–L113, September 2006.
- [5] NASA. 1e 0657-56: Nasa finds direct proof of dark matter. <https://chandra.harvard.edu/photo/2006/1e0657/index.html>, 2006. Revised: August 13, 2018.
- [6] D. Clowe, P. Schneider, A. Aragón-Salamanca, M. Bremer, G. De Lucia, C. Halliday, P. Jablonka, B. Milvang-Jensen, R. Pelló, B. Poggianti, G. Rudnick, R. Saglia, L. Simard, S. White, and D. Zaritsky. Weak lensing mass reconstructions of the ESO Distant Cluster Survey. *Astronomy and Astrophysics*, 451(2):395–408, May 2006.
- [7] Planck Collaboration, N. Aghanim, Y. Akrami, M. Ashdown, J. Aumont, C. Baccigalupi, M. Ballardini, A. J. Banday, R. B. Barreiro, N. Bartolo, S. Basak, R. Battye, K. Benabed, J. P. Bernard, M. Bersanelli, P. Bielewicz, J. J. Bock, J. R. Bond, J. Borrill, F. R. Bouchet, F. Boulanger, M. Bucher, C. Burigana, R. C. Butler, E. Calabrese, J. F. Cardoso, J. Carron, A. Challinor, H. C. Chiang, J. Chluba, L. P. L. Colombo, C. Combet, D. Contreras, B. P. Crill, F. Cuttaia, P. de Bernardis, G. de Zotti, J. Delabrouille, J. M. Delouis, E. Di Valentino, J. M. Diego, O. Doré, M. Douspis, A. Ducout, X. Dupac, S. Dusini, G. Efstathiou, F. Elsner, T. A. Enßlin, H. K. Eriksen, Y. Fantaye, M. Farhang, J. Fergusson, R. Fernandez-Cobos, F. Finelli, F. Forastieri, M. Frailis, A. A. Fraisse, E. Franceschi, A. Frolov, S. Galeotta, S. Galli, K. Ganga, R. T. Génova-Santos, M. Gerbino, T. Ghosh,

J. González-Nuevo, K. M. Górski, S. Gratton, A. Gruppuso, J. E. Gudmundsson, J. Hamann, W. Handley, F. K. Hansen, D. Herranz, S. R. Hildebrandt, E. Hivon, Z. Huang, A. H. Jaffe, W. C. Jones, A. Karakci, E. Keihänen, R. Keskitalo, K. Kiiveri, J. Kim, T. S. Kisner, L. Knox, N. Krachmalnicoff, M. Kunz, H. Kurki-Suonio, G. Lagache, J. M. Lamarre, A. Lasenby, M. Lattanzi, C. R. Lawrence, M. Le Jeune, P. Lemos, J. Lesgourges, F. Levrier, A. Lewis, M. Liguori, P. B. Lilje, M. Lilley, V. Lindholm, M. López-Caniego, P. M. Lubin, Y. Z. Ma, J. F. Macías-Pérez, G. Maggio, D. Maino, N. Mandolesi, A. Mangilli, A. Marcos-Caballero, M. Maris, P. G. Martin, M. Martinelli, E. Martínez-González, S. Matarrese, N. Mauri, J. D. McEwen, P. R. Meinhold, A. Melchiorri, A. Mennella, M. Migliaccio, M. Millea, S. Mitra, M. A. Miville-Deschénes, D. Molinari, L. Montier, G. Morganante, A. Moss, P. Natoli, H. U. Nørgaard-Nielsen, L. Pagano, D. Paoletti, B. Partridge, G. Patanchon, H. V. Peiris, F. Perrotta, V. Pettorino, F. Piacentini, L. Polastri, G. Polenta, J. L. Puget, J. P. Rachen, M. Reinecke, M. Remazeilles, A. Renzi, G. Rocha, C. Rosset, G. Roudier, J. A. Rubiño-Martín, B. Ruiz-Granados, L. Salvati, M. Sandri, M. Savolainen, D. Scott, E. P. S. Shellard, C. Sirignano, G. Sirri, L. D. Spencer, R. Sunyaev, A. S. Suur-Uski, J. A. Tauber, D. Tavagnacco, M. Tenti, L. Toffolatti, M. Tomasi, T. Trombetti, L. Valenziano, J. Valiviita, B. Van Tent, L. Vibert, P. Vielva, F. Villa, N. Vittorio, B. D. Wandelt, I. K. Wehus, M. White, S. D. M. White, A. Zacchei, and A. Zonca. Planck 2018 results. VI. Cosmological parameters. *arXiv e-prints*, page arXiv:1807.06209, July 2018.

- [8] A. A. Penzias and R. W. Wilson. A Measurement of Excess Antenna Temperature at 4080 Mc/s. , 142:419–421, July 1965.
- [9] Giorgio Arcadi, Maíra Dutra, Pradipta Ghosh, Manfred Lindner, Yann Mambrini, Mathias Pierre, Stefano Profumo, and Farinaldo S. Queiroz. The waning of the WIMP? a review of models, searches, and constraints. *The European Physical Journal C*, 78(3), mar 2018.
- [10] P. Fouqué , J. M. Solanes, T. Sanchis, and C. Balkowski. Structure, mass and distance of the virgo cluster from a tolman-bondi model. *Astronomy & Astrophysics*, 375(3):770–780, sep 2001.
- [11] Steven W. Allen, August E. Evrard, and Adam B. Mantz. Cosmological parameters from observations of galaxy clusters. *Annual Review of Astronomy and Astrophysics*, 49(1):409–470, sep 2011.

- [12] Julio F. Navarro, Carlos S. Frenk, and Simon D. M. White. The structure of cold dark matter halos. *The Astrophysical Journal*, 462:563, may 1996.
- [13] Federico Sembolini, Gustavo Yepes, Frazer R. Pearce, Alexander Knebe, Scott T. Kay, Chris Power, Weiguang Cui, Alexander M. Beck, Stefano Borgani, Claudio Dalla Vecchia, Romeel Davé , Pascal Jahan Elahi, Sean February, Shuiyao Huang, Alex Hobbs, Neal Katz, Erwin Lau, Ian G. McCarthy, Giuseppe Murante, Daisuke Nagai, Kaylea Nelson, Richard D. A. Newton, Valentin Perret, Ewald Puchwein, Justin I. Read, Alessandro Saro, Joop Schaye, Romain Teyssier, and Robert J. Thacker. nIFTy galaxy cluster simulations – i. dark matter and non-radiative models. *Monthly Notices of the Royal Astronomical Society*, 457(4):4063–4080, feb 2016.
- [14] Andrey V. Kravtsov. THE SIZE-VIRIAL RADIUS RELATION OF GALAXIES. *The Astrophysical Journal*, 764(2):L31, feb 2013.
- [15] Volker Springel and Glennys R. Farrar. The speed of the ‘bullet’ in the merging galaxy cluster 1E0657-56. , 380(3):911–925, September 2007.
- [16] Paraficz, D., Kneib, J.-P., Richard, J., Morandi, A., Limousin, M., Jullo, E., and Martinez, J. The bullet cluster at its best: weighing stars, gas, and dark matter. *A&A*, 594:A121, 2016.
- [17] Malcolm S. Longair. *High Energy Astrophysics*. Cambridge University Press, 3 edition, 2011.
- [18] Irving Langmuir. Oscillations in Ionized Gases. *Proceedings of the National Academy of Science*, 14(8):627–637, August 1928.
- [19] Richard Fitzpatrick. *Plasma Physics: An Introduction*. CRC Press, Taylor Francis Group, 2014.
- [20] R.M. Kulsrud. *Plasma Physics for Astrophysics*. Princeton University Press, 2005.
- [21] D. B. Melrose. *Instabilities in Space and Laboratory Plasmas*. CAMBRIDGE UNIVERSITY PRESS, 1986.
- [22] Reinhard Schlickeiser. *Cosmic Ray Astrophysics*. Springer-Verlag, Berlin, Heidelberg, 2002.

- [23] Francis Chen. *Introduction to Plasma Physics and Controlled Fusion*. Springer, 01 2016.
- [24] Lewi Tonks and Irving Langmuir. Oscillations in Ionized Gases. *Physical Review*, 33(2):195–210, February 1929.
- [25] Peter Debye and Erich Hückel. Zur theorie der elektrolyte. i. gefrierpunktserniedrigung und verwandte erscheinungen. *Physikalische Zeitschrift*, 24(185):305, 1923.
- [26] Robert Lasenby. Long range dark matter self-interactions and plasma instabilities. *Journal of Cosmology and Astroparticle Physics*, 2020(11):034–034, Nov 2020.
- [27] A. Bret. Weibel, two-stream, filamentation, oblique, bell, buneman...which one grows faster? *The Astrophysical Journal*, 699(2):990–1003, Jun 2009.
- [28] A B Mikailovskii. *Theory of plasma instabilities. Volume 1. Instabilities of a homogeneous plasma*. Springer, 1974.
- [29] A. Bret. Beam-plasma dielectric tensor with mathematica. *Computer Physics Communications*, 176(5):362–366, 2007.
- [30] A. Bret, L. Gremillet, D. Bé nisti, and E. Lefebvre. Exact relativistic kinetic theory of an electron-beam–plasma system: Hierarchy of the competing modes in the system-parameter space. *Physical Review Letters*, 100(20), may 2008.
- [31] A. Bret, L. Gremillet, and D. Bénisti. Exact relativistic kinetic theory of the full unstable spectrum of an electron-beam-plasma system with Maxwell-Jüttner distribution functions. , 81(3):036402, March 2010.
- [32] O. Buneman. Dissipation of currents in ionized media. *Phys. Rev.*, 115:503–517, Aug 1959.
- [33] Del Anderson, Renato Fedele, and M. Lisak. A tutorial presentation of the two stream instability and landau damping. *American Journal of Physics - AMER J PHYS*, 69:1262–1266, 12 2001.
- [34] D B Melrose. A covariant formulation of wave dispersion. *Plasma Physics*, 15(2):99–106, feb 1973.
- [35] Oliver Penrose. Electrostatic instabilities of a uniform non-maxwellian plasma. *The Physics of Fluids*, 3(2):258–265, 1960.

- [36] Prateek Agrawal, Francis-Yan Cyr-Racine, Lisa Randall, and Jakub Scholtz. Make dark matter charged again. *Journal of Cosmology and Astroparticle Physics*, 2017(05):022–022, may 2017.
- [37] Fitzpatrick, Richard. Particle-in-cell codes. <https://farside.ph.utexas.edu/teaching/329/lectures/node96.html>, 2006. Accessed: 2022.
- [38] D. Bohm and E. P. Gross. Theory of Plasma Oscillations. A. Origin of Medium-Like Behavior. *Physical Review*, 75(12):1851–1864, June 1949.
- [39] Mohamad Shalaby, Avery E. Broderick, Philip Chang, Christoph Pfrommer, Astrid Lamberts, and Ewald Puchwein. SHARP: A spatially higher-order, relativistic particle-in-cell code. *The Astrophysical Journal*, 841(1):52, may 2017.
- [40] Akaxia Cruz and Matthew McQuinn. Astrophysical Plasma Instabilities induced by Long-Range Interacting Dark Matter. *arXiv e-prints*, page arXiv:2202.12464, February 2022.
- [41] Milton Abramowitz and Irene A. Stegun. *Handbook of mathematical functions with formulas, graphs, and mathematical tables*. United States. Government Printing Office., 1965.